'76

IPCR cyclotron
Progress Report 1976

Vol. 10

IPCR Cyclotron Progress Report

Vol. 10

Editors

This volume contains recent information of the IPCR Cyclotron, informal reports and abstracts of papers which will be published at scientific meetings or in publications by staff members, guests, and visitors.

CONTENTS

5. NUCLEAR PHYSICS
    Nuclear Spectroscopy

6. NUCLEAR INSTRUMENTATION

7. ATOMIC AND SOLID-STATE PHYSICS

8. RADIOCHEMISTRY AND NUCLEAR CHEMISTRY

9. RADIATION CHEMISTRY AND RADIATION BIOLOGY

PREFACE TO PUBLICATION OF THE 10TH PROGRESS REPORT

After World War II, our institute underwent prolonged financial difficulty for years and the facilities became obsolete in that period. Gradually, however, situation began improving thanks to the endeavour of people of the institute and helps from outside. The legislation of 1958 to reorganize RIKAGAKU KENKYUSHO as a non-profit research institute and subsequent government approval of acquiring a new site of the institute at the present location to move from the old crowded Komagome area warranted the renewal of RIKEN. Construction of the cyclotron was planned at that time to take the place of the Nishina's cyclotron destroyed after the War and symbolized our determination to improve our facilities. All the basic design was made by members of the institute and constructional work was completed in the fall of 1966.

The design was unique at that time in its capability of acceleration of heavy ions such as ^{12}C, ^{14}N and ^{16}O as well as lighter ions and in the possibility of changing particle energy widely. Shortly after the completion of the cyclotron, acceleration of heavy ions by tandem Van de Graaffs became popular abroad. However in Japan, there were few other cyclotrons or tandems which can accelerate heavy ions to sufficiently high energy until few years ago. The RIKEN cyclotron has been the only high energy heavy ion facility in this country for these 10 years. Fortunately, operation of the cyclotron was found simple and easy in spite of its use for wide variety of particles and energy. It must be mentioned that the people working in the field other than nuclear physics have used high energy heavy particles as new means of research in their fields and many remarkable results have been obtained. It is needless to say that important contributions to nuclear study have also been made. All those studies have been recorded in the Progress Reports issued for these 10 years together with the technical achievements made by the engineering staffs. This is the 10th volume and shows still growing activity around the cyclotron. We are proud of our achievements made in the past and also are glad to see prospect of further development of research in this institute by use of the cyclotron and the new heavy ion linac under construction.

Shinji FUKUI
President

1. INTRODUCTION

Ten years have elapsed since the first beam was successfully accelerated in our cyclotron. Our cyclotron is the first one in Japan that has widely been used in fields not only of nuclear physics but also in solid state physics, chemistry and biology.

The cyclotron continued to work, as before, in good condition all through last year. Several improvements have been made in the machine and its accessory facilities.

A number of experimental studies on nuclear reactions and level structures were continued from previous years. Heavy-ion induced X-rays were studied using a Bragg crystal spectrometer as well as Si(Li) detectors with good energy resolution. Channeling experiments were continued with high energy alpha particles. Perturbed angular correlation (PAC) studies were made on transition metal ions in magnetic oxides. Positron annihilation studies on metals were continued. Emission spectra of alkali halides were measured under low temperature heavy-ion irradiation to obtain information on initial species produced. Effects of heavy ions on DNA synthesis in bacterial and cultured mammalian cells have been investigated, together with the production of radioisotopes and labelled compounds for the medical use.

The first resonator and the injector of the heavy-ion linear accelerator were installed in a new building.

Hiromichi Kamitsubo

Editor

2. MACHINE OPERATION

S. Fujita, H. Nakajima, K. Ogiwara, K. Ikegami,
T. Kageyama, S. Kohara, H. Takebe, and I. Kohno

During the period from Oct. 23, 1975 to Oct. 22, 1976 the cyclotron was operated on the 24h-per-day basis. Statistics of machine operation is given in Table 1. The working time meter for the beam, which indicated 4597h, was increased by about 19 % (744h) compared with that of the last year. This increase in working time is due to the decrease in holidays and in the loss by troubles.

Table 1.   Machine operation.

Date	Oscillator	Ion source	Beam
Oct. 23, 1975	42088.3 (h)	45174.3 (h)	14878.2 (h)
Oct. 22, 1976	47050.3 (h)	50354.2 (h)	19474.9 (h)
365 days	4962.0 (h)	5179.9 (h)	4596.7 (h)
Percentage of 365 days	56.6 %	59.1 %	52.5 %

Schedule in this period	
Beam time	246 (days)
Overhaul and installation work	46 (days)
Periodical inspection and repair	32 (days)
Vacation and holidays	41 (days)

Table 2 shows beam time alloted to various activities in this period. Requests for heavy ion beams continued to increase and the cyclotron was operated 143 days with the heavy ion source, which was 58.4 % of the total scheduled beam time. The beam time alloted to the inner atomic shell excitation study was increased by about 300 h and the study of stopping power with heavy ion beams was newly begun.

Following troubles occurred during this period. A bearing of the circulation pump for deionized cooling water was broken. Vacuum leak developed at vacuum seal of a ceramic insulator which connects copper cooling water tube to the shorting plane. Metal of the vacuum seal was found eroded by electrolysis.

These troubles brought about a loss of about 12 days.

A cooling tower to remove heat from the cyclotron facilities was set on the roof of the cyclotron vault instead of the cooling pond used until then.

Table 2.   Scheduled beam time and subjects of activity in the period XI.

Subject		Heavy ion	Light particles	Total
Nucl. Phys.	Nuclear reaction	2241 (h)	935 (h)	3176 (h)
	In-beam spectroscopy	321 (h)	122 (h)	443 (h)
	RI production	0 (h)	153 (h)	153 (h)
Fields other than Nucl. Phys.	Nuclear chemistry	0 (h)	155 (h)	155 (h)
	Radiation chemistry	138 (h)	74 (h)	212 (h)
	Radiation biology	128 (h)	80 (h)	208 (h)
	Solid state physics	12 (h)	546 (h)	558 (h)
	Inner atomic shell excitation study	344 (h)	48 (h)	392 (h)
	Stopping power study	34 (h)	0 (h)	34 (h)
Outside users	Nuclear medicine	0 (h)	75 (h)	75 (h)
	Nuclear fuel study	0 (h)	106 (h)	106 (h)
	RI production	0 (h)	5 (h)	5 (h)
Development of instruments		24 (h)	12 (h)	36 (h)
Total		3242 (h)	2311 (h)	5553 (h)
Percent in total		58.4%	41.6 %	100 %

Maintenance: operation and engineering

Exchange of ion sources	80 (h)
Reserved for beam time adjustment and cooling of radio-activity	271 (h)
Machine inspection and repair	744 (h)
Total	1095 (h)

3. MACHINE DEVELOPMENT AND ACCELERATOR PHYSICS

3-1. The Production of Multiply Charged Lithium and Magnesium Ions from a PIG Source

A. Shimamura, T. Tonuma, and I. Kohno

In order to develop an ion source of lithium and magnesium for the cyclotron we have studied the production of multiply charged ions of these metals from a PIG source. Details of the ion source is shown in Fig. 1. The anode is made of stainless steel without cooling and a stainless steel oven is used for the production of metal vapour. For the operation of the ion source the use of a supporting gas is essential. Its first function is to enable an arc to be struck in the ion source, and its second function is to keep the metal vapour to maintain a stable arc. We used argon as the supporting gas and studied the production of multiply charged ions of lithium and magnesium. The ion beam extracted from the ion
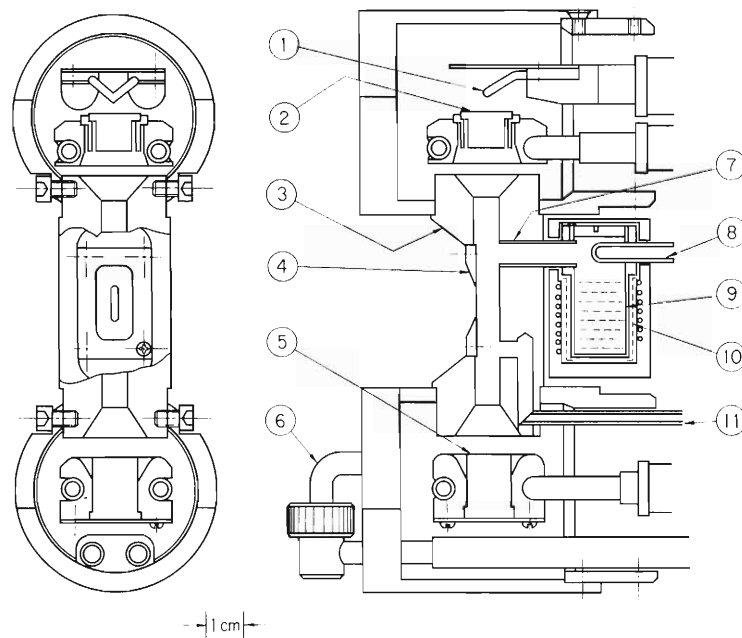
Fig. 1. Cross-sectional view of the ion source.
① - filament (W), ② - hot cathode(W),
③ - anode box (copper), ④ - slit plate(Mo),
⑤ - reflector cathode (W), ⑥ - cooling tube,
⑦ - ceramic chimney, ⑧ - ceramic tube for thermo couple,
⑨ - oven (stainless steel), ⑩ - ceramic paper,
⑪ - gas feed
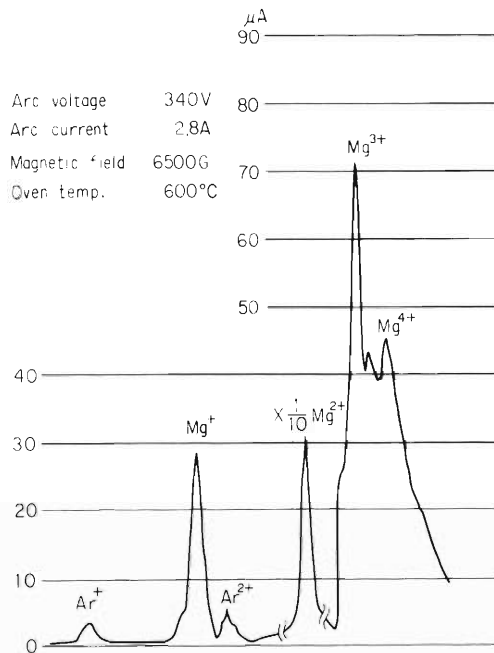
Fig. 2. M/q spectrum of ion beams of magnesium (supporting gas: argon).
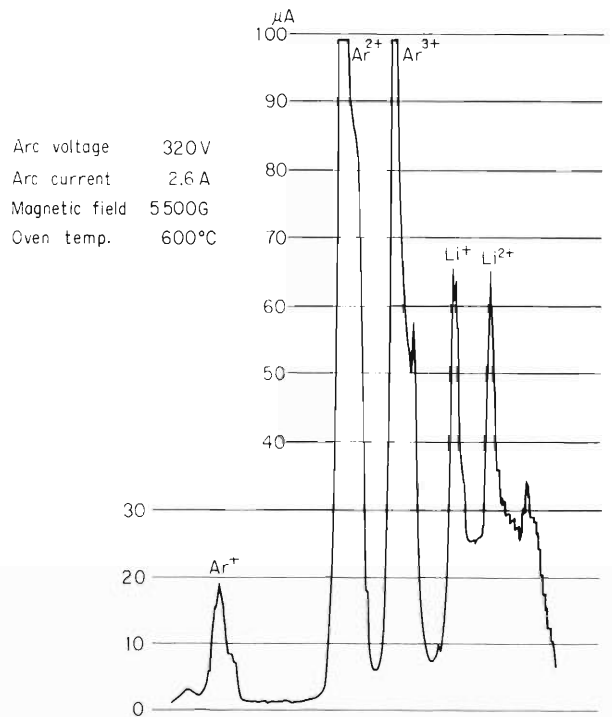
Fig. 3. M/q spectrum of ion beams of lithium (supporting gas: argon).

source was analyzed by a 180° mass-spectrometer. The charge spectra of magnesium and lithium measured are shown in Figs. 2 and 3.

3-2. An Improved Heavy Ion Source

H. Nakajima, T. Kageyama, and S. Kohara

Heavy ions such as C,N and O have been accelerated in the cyclotron since 1967. The variety of particles and range of energies of the cyclotron are limited by its minimum accelerating frequency and maximum dee voltage (Fig. 1). All kinds of ions are accelerated by fundamental mode since we cannot extract the beam by any harmonic mode on account of adoption of the R-F type deflector.

Besides, ions of charge to mass ratio $Z_i/A = 0.25$ (such as C^{3+}, O^{4+}, and Ne^{5+}) are not accelerated because it was difficult to hold dee voltage for accelerating such ions. O^{5+} is routinely accelerated instead of O^{4+} although the extracted beam intensity is about 5 % of the beams of N^{4+} and C^{4+}. Therefore, it is necessary to increase the intensity of highly charged ions from the ion source to extend the performance of the cyclotron.

According to our experimental data and several publications by others the production rate of multiply-charged ions in the PIG ion source with indirectly heated cathode, increases in proportion to the square or cube of the arc power and to inverse of the 12 th power of the gas flow rate.[1] We have also experienced an increase in intensity of highly charged ions by a discharge chamber having a smaller diameter than that used at present.

An improved ion source was designed based on these well recognized facts. The main features are as follows: a precise assembly of the electrodes, no hole other than ion extraction slit is provided to allow reduction of gas flow and the use of an arc chamber with a smaller
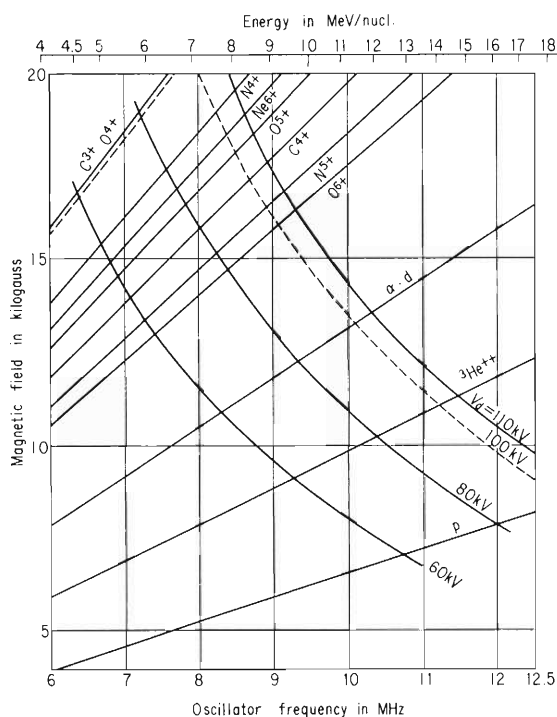
Fig. 1. The resonance condition of the IPCR 160 cm variable energy cyclotron, radius of beam exit is 74 cm. The dotted lines indicate the upper limit of dee voltage.
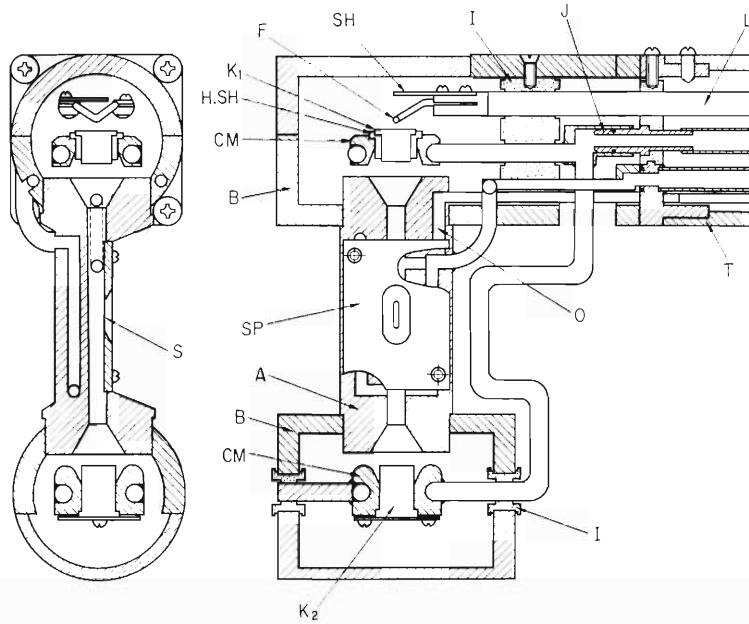
Fig. 2. Cross-sectional view of the ion source.

K_1 : hot cathode (W), K_2 : reflector cathode(W),

CM : cathode mount (copper and water-cooled),

HSH : cathode heat shield (W), SH : electron shield,

F : filament, B : anode box (copper), SP : slit plate (Mo),

S : Source aperture,

O : distribution plenum, A : exhaust window,

I : insulator (steatite), J : cooled joint,

L : leading tube, T : supporting tube, G : copper spacer.
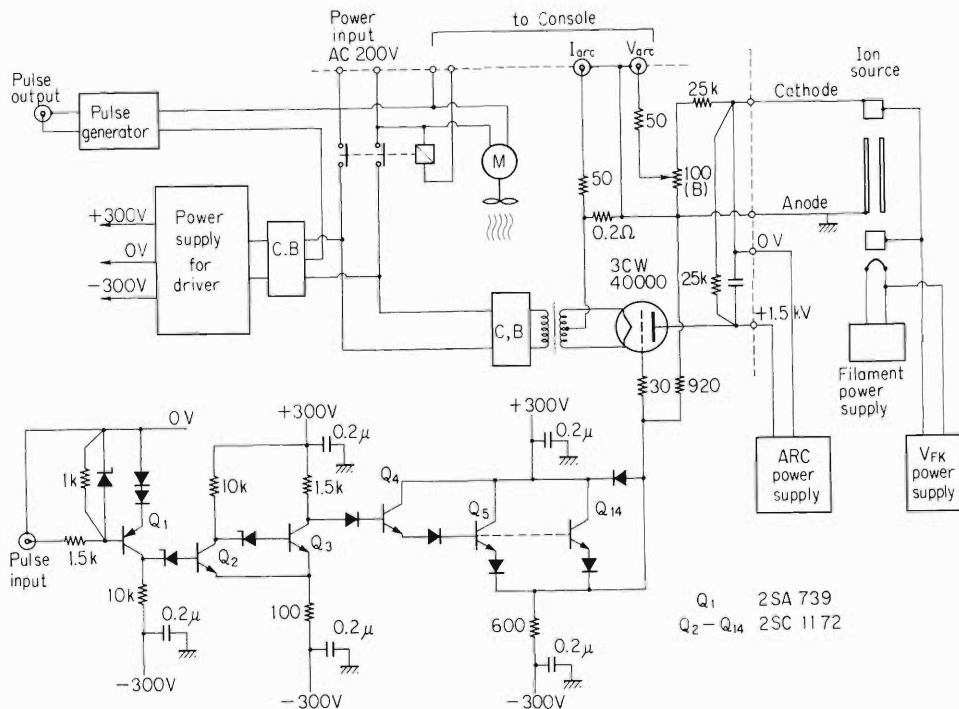
Fig. 3. Circuit of the pulsed arc power supply.

bore diameter (see Fig. 2). Also a pulsed arc power supply was designed which can produce a large instantaneous arc power. 10 kW is available at peak. The circuit consists of a power tube and a transistorized driver stage and will be used with the above ion source and the power supply working at present (Fig. 3).

We hope to be able to raise the intensity of N^{5+} and O^{5+} and to accelerate new ions such as O^{6+} and Ne^{6+}.

Reference

1) Y. Miyazawa, I. Kohno, T. Inoue, T. Tonuma, A. Shimamura, and S. Nakajima: IPCR Cyclotron Technical Report, No. 2 (1972).

3-3. An Automatic Control of the Pumping System for the Vacuum Chamber of the Cyclotron

K. Ikegami, T. Kageyama, T. Watanabe, and T. Noda

The pumping system of the cyclotron is composed of 32", 14" and 6" oil diffusion pumps connected in series, and several roughing pumps as shown in Fig. 1.[1] Instead of manual operation an automatic control device of the pumping system was developed and many valves were replaced with pneumatic ones.

In the new control system, pumps and valves are operated automatically according to the indication of Pirani-detectors to evacuate the chamber of the cyclotron up to the pressure of $0.7 \sim 1.0 \times 10^{-6}$ Torr, and also to protect the pumping system against vacuum failure by accidental leakage in the chamber. Pirani detectors used can give trip signals at arbitrary value of pressure chosen between atomosphere and 1×10^{-3} Torr. Figure 2 shows the graphic handling board of the pumping system which is installed on the control panel, and each switch is provided with a name card showing its function briefly. When the switch "Auto" is pushed the pumping system can be operated automatically according to the predetermined sequence for evacuation of the chamber by pushing the running switch but in the state of "MANU" the pumping system is operated by switching each pump and valve manually.

Figure 3 shows the standard circuit for the new control system which is the same one as the unit circuit used previously.[2] In Fig. 4 the sequence of operation of the pumping
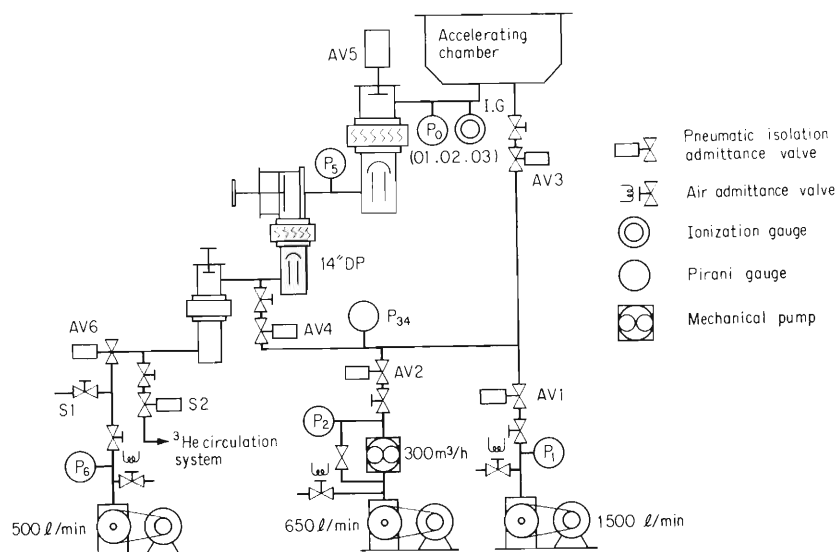
Fig. 1. Schematic diagram of the vacuum system for IPCR 160cm cyclotron.

system is shown. The sequence begins from starting up of 1500 ℓ/m rotary pump and proceeds in due order up to evacuation of the chamber by the main diffusion pumps.
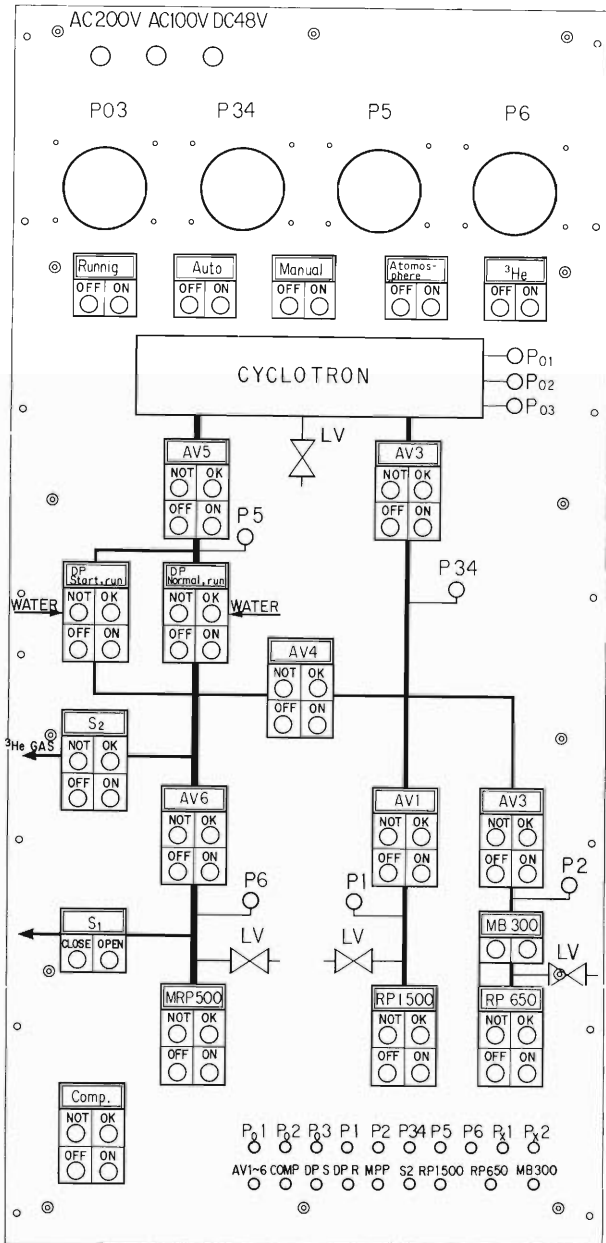
Fig. 2. A diagram of handling board of the vacuum system.
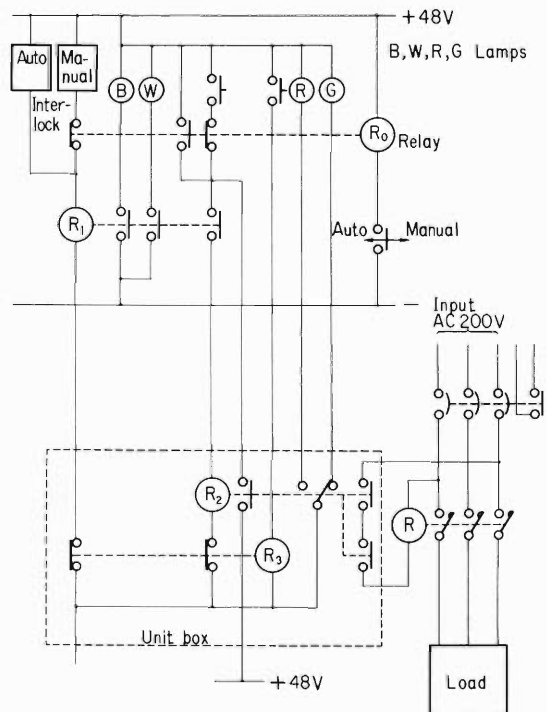
Fig. 3. A diagram of a circuit for control system.

12
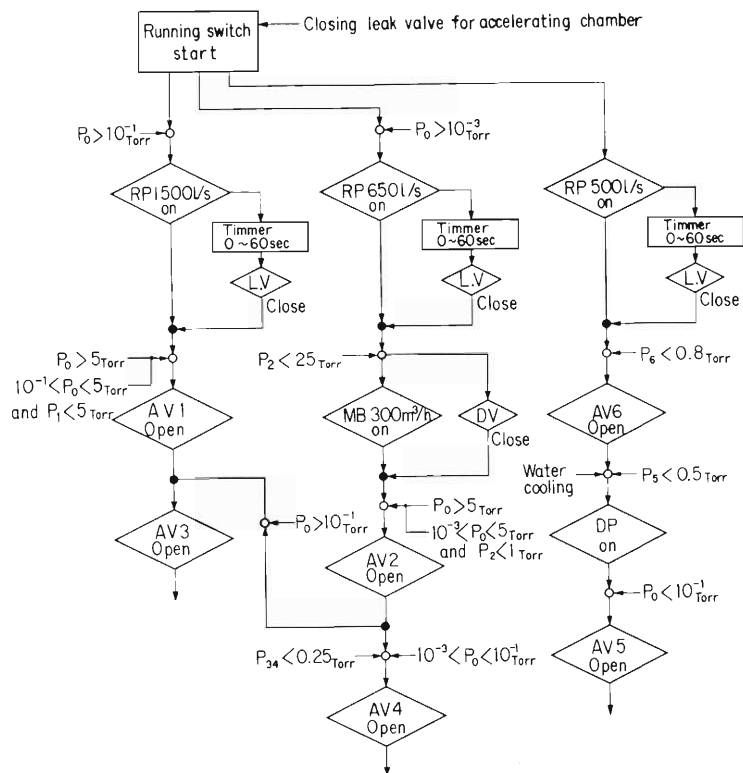
Fig. 4. A sequence diagram of automatic operation of the
installation. P_0 indicates the pressure at the accelerating
chamber. Pn (n=0~6) corresponds to the vacuum at each
place of the vacuum system shown in Fig. 1.

References

1) T. Tonuma, Y. Miyazawa, K. Yoshida, T. Karasawa, and H. Kumagai: J. Vacuum Soc.
    Japan, 12, 11 (1969).

2) T. Inoue, I. Kohno, and S. Takeda: Reports IPCR (in Japanese), 46, 103 (1970).

3-4. Ultra-compact Cyclotron

T. Karasawa and K. Sakabe*

Cyclotron-produced radionuclides have been widely used in nuclear medicine as well as other fields. Of all the different kinds of accelerators, a cyclotron is the most useful source of radionuclides. Carbon, nitrogen and oxygen are physiological key elements. Radionuclides of these elements with short half-lives of 2 to 20 minutes cannot be transported and require "in-house" preparation.

The ultra-compact cyclotron, the so-called "desk top" cyclotron to be described, aimes particularly at radionuclides production of ^{11}C, ^{13}N, ^{15}O, and ^{18}F. The cyclotron is a 4-sector radial ridge fixed energy AVF cyclotron. Its performances are shown in Table 1.

Table 1. Performances of the ultra-compact cyclotron.

Particle	Energy	f	Harmonic number	Target** energy	Radionuclides	Nuclear reaction
Proton	9.4 MeV	54 MHz	2	9.3 MeV	^{11}C, ^{13}N	(p, d)
Deuteron	4.7 MeV	54 MHz	4	4.3 MeV	^{11}C, ^{13}N, ^{15}O	(d, n)
^{3}He^{++}	12.5 MeV	38 MHz	2	11.5 MeV	^{18}F	(^{3}He^{++}, p)
α-particle	9.4 MeV	54 MHz	4	7.7 MeV		

f: Frequency of oscillator.
**: After passing through an entry window foil of target box.
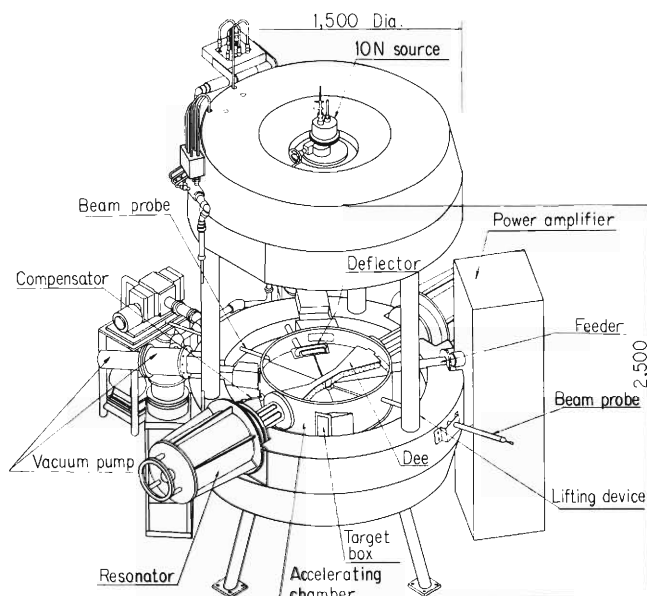
Fig. 1. Birdeye view of the cyclotron.

* The Japan Steel Works, Ltd.
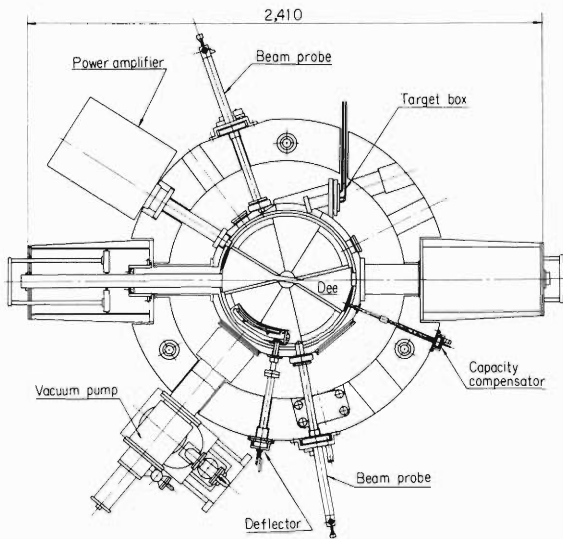
Fig. 2(a) Holizontal section.
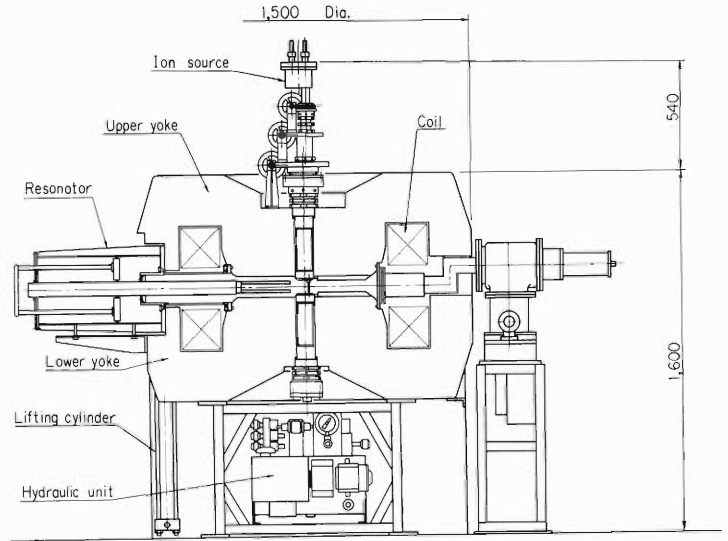
Fig. 2(b) Vertical section.

Table 2. Detailed parameters of the cyclotron.

(1) Magnet

Diameter		Weight		Gap		Field
pole tip	600mm	Fe	7.5ton	hill	50mm	2.4Tesla
pole base	720mm	Cu	0.5ton	valley	90mm	1.6Tesla
outermost	1500mm			average	64.3mm	1.84Tesla

Exciting coil: water cooled hollow conductor, $4A/mm^2$, 336turns

Power supply: 440A×90V 40kW, normal 24kW

Trimming coil: two harmonic coil pairs at extraction radius

Extraction radius: 240mm

(2) Radio-frequency system

Frequency: 54MHz and 38MHz

Dee voltage: 35kV

Q-value: 3000

Shunt impedance: 65k-ohm

MOPA (master oscillator power amplifier)

Capacity-coupled

Coaxial resonator

Power amplifier 3CW20000A7 (EIMAC)

(3) Vacuum system

Turbo-molecular pumps	two 250ℓ/s
Roots blower pump	30m³/h
Rotary pump	100ℓ/min.
Final vacuum	1×10^{-5} Torr.
Operating vacuum	8×10^{-5} Torr.

Figure 1 is a birdeye view when upper yoke is lifted and Fig. 2-(a) and 2-(b) are holizontal and vertical sections of the cyclotron, respectively. The detailed parameters of the cyclotron are given in Table 2.

Design features of the cyclotron are self-radiation shielding[1] and push-button operation. The circular magnet yoke surrounding the cyclotron absorbs radiations coming from inside so that the cyclotron can be installed in a small vault with thin concrete walls. The control system is of such an arrangement and structure that the cyclotron may be operated by pushing six buttons and adjusting ion source power. Thus the cyclotron can be operated in good stability by those who have no high discipline and experience.

The project of the prototype cyclotron was started in December 1972 under a patent licence agreement between IPCR and the Japan Steel Works. The patent is "Self Shielding Type Cyclotron".[1] All components necessary for the electromagnet including field mapping equipment were assembled in spring 1974 at the Muroran plant of JSW. We then began magnetic field mapping and finished it in autumn 1975. We started beam test in spring this year at the Muroran plant and were able to accelerate both proton and deuteron up to the maximum radius on the 16th of July. The beam current measured by the probe vs. radius is shown in Fig. 3.
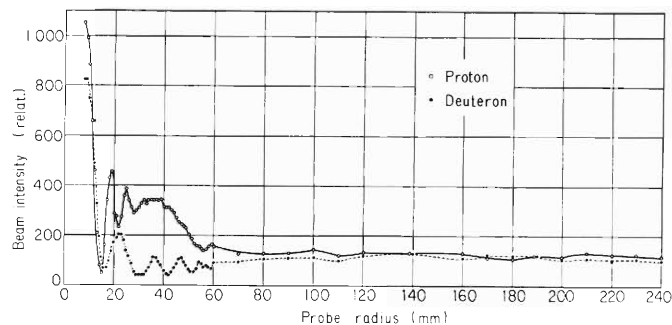
Fig. 3. Beam current versus radius.

During construction of the prototype, following three problems appeared but were successively solved step by step: (1) formation of isochronous magnetic field distribution[2] for 9.4 MeV proton without circular trimming coils, (2) development of dees and resonators with a moderate Q-value at relatively high frequencies and (3) adjustment of initial motion of beam and precession of orbit center resulting from the harmonic acceleration. Reports on these problems will be described in other papers.[3]

References

1) Japanese Patent 818015 and USA Patent 3921019.
2) T. Karasawa and Y. Toda: Reports of IPCR, (in Japanese), 52, 185 (1976).
3) T. Karasawa: ibid., 53, 35 (1977).

3-5. Operation of the IPCR Polarized Ion Source for the INS Isochronous Cyclotron

S. Motonaga, T. Fujisawa, F.G. Resmini,* Y. Toba,
S. Yamada,** N. Ueda,** T. Hasegawa,* and H. Kamitsubo

A polarized proton and deuteron source of an atomic beam type for the INS isochronous cyclotron has been built and installed. All of the mechanical parts and electrical power supplies were manufactured by the workshop of IPCR.

The polarized ion source is mounted vertically on the cyclotron roof shielding as shown in Fig. 1, its beam being injected axially into the accelerator through a bore in the upper yoke. An axial beam injection line, whose optical elements are an einzel lens and two electrostatic quadrupole triplets, brings the beam 4.3 meters down to the cyclotron median plane. A
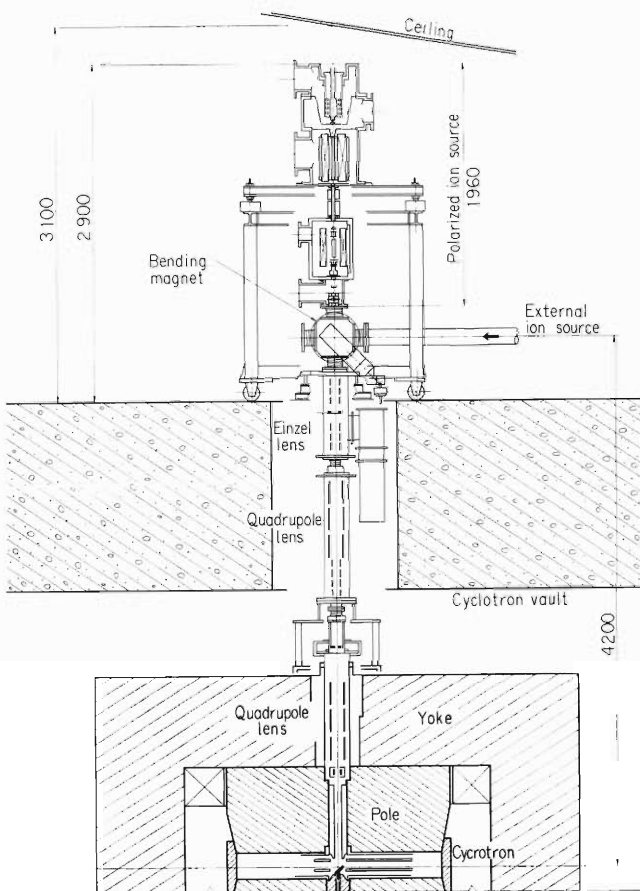
Fig. 1. Simplified layout of the ion source and the axial injection system.
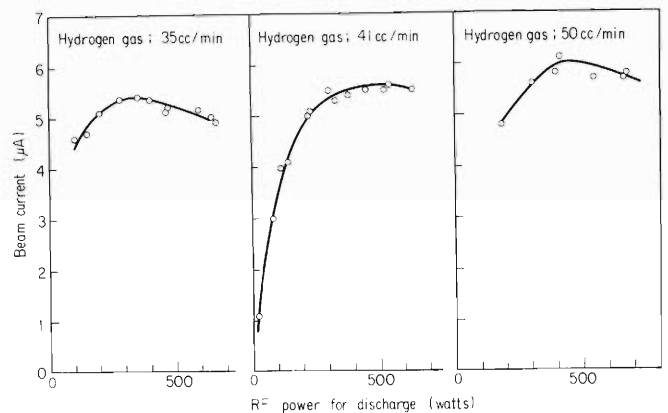
Fig. 2. Intensity of polarized beam as a function of power in the rf discharge.

* Milan University, Italy.
** Institute for Nuclear Study, University of Tokyo.

gridded electrostatic mirror inflects the beam into the dummy dee. More details of the injection system and experimental results have been described in a recent paper.[1] Typical beam current measured at the normal operation were up to 5μA of polarized protons at the exit of the source, 0.1μA accelerated in the cyclotron, 0.03μA external beam with polarization of 70%. A brief account and the operating characteristics of the IPCR polarized ion source are as follows: Molecular hydrogen or deuterium is dissociated in rf-discharge, driven by a 1 kW, 25 MHz oscillator. The discharge tube and nozzle are cooled by flowing water. The gas flow out of the tube is in the range of 50 cc/min. The atomic hydrogen emerging from the nozzle is restricted by a skimmer, and then collimated by a diaphragm at the entrance to the sextupole magnet at a distance of 60 mm from the skimmer. Atomic hydrogen which could not go through the skimmer is evacuated with two oil diffusion pumps having a speed of 4000 ℓ/s. A trouble arose which is inherent in a system using a high pressure discharge tube. It is the rapid polymerization of the diffusion pump oil resulting from the large atomic hydrogen gas load. The pumps on the nozzle exhaust chamber were most seriously affected and needed to be cleaned and oil recharged after about 150 h of operation. Oil used at present is Silicon DC-705 oil. In the early stage of the operation of the polarized ion source, the operation of the discharge tube was found to be unstable. The polarized beam current went out frequently to zero in a periodic fashion, the period depending on the power of the discharge. A water container was then installed in a gas line to give moisture to the hydrogen. Thereafter stable operation of the dissociator with increased polarized beam intensity has been obtained. Measurement of the polarized beam intensity with different gas flow rates into the discharge tube as a function of the discharge power for dissociation was carried out. Figure 2 shows results of such measurement with wet hydrogen gas.

The separation of the hyperfine-structure components is done by a sextupole magnet having an axial length of 35 cm, an entrance aperture of 6.5 mm, and an exit aperture of 13.5 mm. The magnet produces the maximum field of 7.2 KG at poletips.

High values of nuclear polarization can be achieved by use of RF transitions between

Table 1. RF-transition parameters.

Particle	#1 Transition	Frequency (MHz)	Static field (gauss)	Gradient H	#2 Transition	Frequency (MHz)	Static field (gauss)	Gradient H	Polarization P_z, P_{zz}
Hydrogen	$\pi_{1\to3}$	10	6	2					-1,
					$\sigma_{2\to4}$	1480	150	5	$+1$,
Deuterium									
	$\pi_{1\to4}$	10	11	3					$-\frac{2}{3}$, 0
					$\sigma_{3\to5}$	378	117	5	$+\frac{1}{3}$, -1
	$\pi_{1\to4}$	10	11	3	$\sigma_{3\to5}$	378	117	5	$-\frac{1}{3}$, -1

π : Static field is perpendicular to rf field

σ : Static field is parallel to rf field

hyperfine-structure levels. Table 1 shows the proposed operating scheme for hydrogen and deuterium atoms and degree of nuclear polarization after the strong field ionizer. The polarization value of the Table 1 are of ideal one and smaller values were obtained in practice. For the case of 28 MeV polarized proton beam, $P_Z = \pm 0.7$ was obtained from the measurement using the $C(\vec{p},p)C$ reaction, when the transition $1 \rightarrow 3$ was induced. At the present test, the sign of the vector polarization is reversed by reversing the magnetic field in the ionizer but it resulted in a loss of beam intensity of about 10 %. The reason for this phenomenon is not completely understood.

The atomic beam is ionized in the strong field ionizer by electron collision. A magnetic field of about 1300 gauss is applied parallel to the beam axis. Figure 3 shows schematic diagram (a) and a typical operation parameters of the electrical potentials along the axis (b) of the ionizer
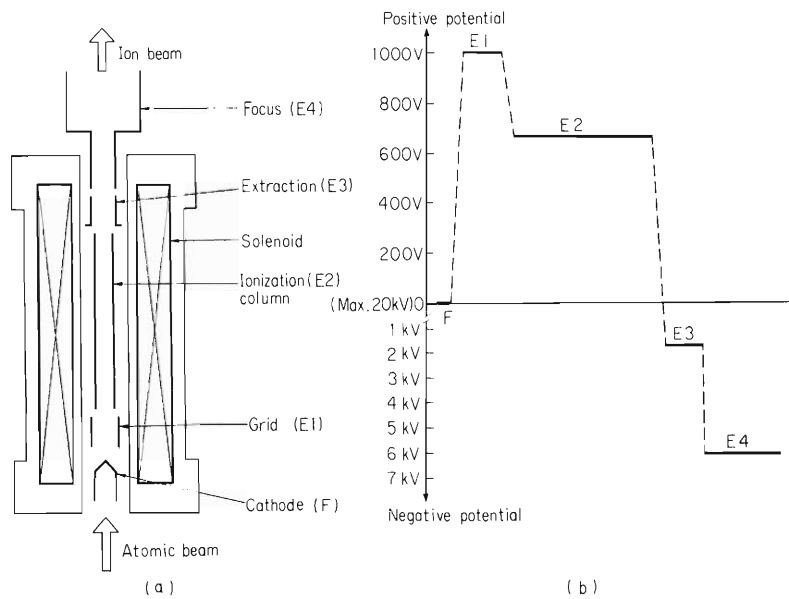
Fig. 3. Schematic diagram (a) and electrostatic potentials (b) in the strong field ionizer.

The solenoid coil, the filament and all of the electrodes are biased at a maximum positive potential of 20 kV to the ground in order to inject the ion beam into the cyclotron. The value of ionization efficiency is estimated to be 5×10^{-3}.

Typical pressure in the different sections of the polarized ion source were measured under the normal operating condition in which the gas flow rate from the nozzle was 50 cc/min. The results obtained are $p = 1.2 \times 10^{-4}$ Torr in the dissociator, $p = 1.8 \times 10^{-6}$ Torr in the sextupole magnet and $p = 2.2 \times 10^{-7}$ Torr in the ionizer.

Reference

1) S. Yamada, N. Ueda, U. Sakurada, M. Sekiguchi, T. Tanabe, T. Honma, and T. Hasegawa: Genshikaku Kenkyu., 21, 772 (1976). Circular in Japanese.

3-6. Design Study of a Separate-Sectored Cyclotron for Heavy-Ions

S. Motonaga, H. Kamitsubo, and N. Nakanishi

A separate-sectored ring cyclotron was proposed as an energy booster of particles from a low energy accelerator at this institute. A variable frequency linac for heavy ions is supposed as an injector. Injection energy ranges between 4 MeV/amu and 1 MeV/amu for light and very heavy ions, and the cyclotron post accelerator extends the maximum energy to 75 MeV/amu and 10 MeV/amu for light and very heavy-ions like Uranium, respectively. Table 1 lists the design parameters of the cyclotron. The cyclotron consists of 4 sector magnets which have maximum field-radius product of 3600 KG·cm, and azimuthal pole width of 50°. The effective sector angle of 50° was chosen to provide strong axial and radial focusing of the ion beam without encountering resonances due to magnet periodicity and field inperfections.[1] The machine dimensions from edge to edge are about 10 meter on the magnet yokes. An energy gain of up to 1 MeV per turn is achieved with two resonators in opposite valleys.

Design study of the proposed accelerator will be made along an iterative design procedure and consists of successive measurements by model magnets (Fig. 1). In order to obtain detailed information on properties of a sectored magnet, a 1/4 scale model of the magnet has

Table 1. Design parameters of the post-stripper accelerator:
Separate sectored ring cyclotron.

Maximum energy, MeV/amu	
Uranium ($^{238}U^{42+}$)	10
Carbon ($^{12}C^{6+}$)	75
Energy constant, K, ($E=Kq^2/A$)	320
Number of sectors	4
Sector angle, degree	50°
Orbital magnet fraction	0.55
Gap between poles, (cm)	12
Maximum magnetic field, (KG)	17
Injection radius, (cm)	53.1
Extraction radius, (cm)	212.4
Energy gain per turn, (MeV)	1
Number of dees	2
Width of dee, degrees	22
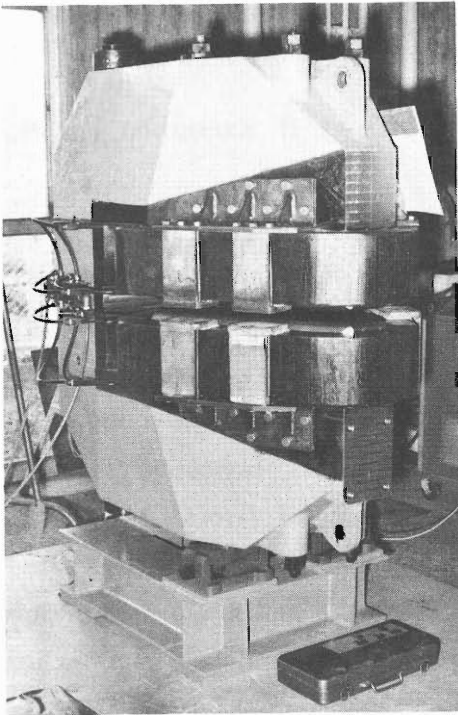
Fig. 1. A view of the 1/4 model magnet.

been constructed, and the measurements of magnetic excitation characteristic, and the field distribution inside and outside the magnet gap at various field strength are being in preparation. The isochronism and focusing characteristics of the beam will then be calculated using results of the measurements.

Reference

1)   M. M. Gordon: Ann. Phys., <u>50,</u> 571 (1968); Nucl. Instr. Methods, <u>58,</u> 245 (1968).

4. NUCLEAR PHYSICS

Scattering and Reactions

4-1. Blocking Effect in the Core-Excitation of ^{29}Si

Y. Toba, N. Nakanishi, H. Sakaguchi,*
A. Goto,*   N. Kishida,**   and F. Ohtani*

When an odd-A nucleus is core-excited by certain nuclear particles, the hindrance of the core-excitation is expected due to the presence of an odd valence particle. This blocking effect caused by the Pauli exclusion principle will be seen more apparently in inelastic scatterings on an odd-A nucleus with low j-value of an odd nucleon.

Inelastic scattering experiments of ^{28,29}Si were performed using momentum analysed 16.2 MeV proton beam accelerated by the cyclotron. Angular distributions of protons to the following final states were measured: 0_1^+(g.s.), 2^+(1.78 MeV), 4^+(4.61 MeV), 0_2^+(4.97 MeV), 3^+(6.27 MeV), of ^{28}Si, and $1/2^+$(g.s.), $3/2_1^+$(1.273 MeV), $5/2_1^+$(2.032 MeV), $3/2_2^+$(2.427 MeV), $5/2_2^+$(3.069 MeV) of ^{29}Si. Self-supporting targets were prepared by vacuum evaporation of natural silicon powder and silicon oxide powder of enriched isotopes (^{29}SiO$_2$) obtained from ORNL. Scattered particles were detected with a silicon surface barrier detector.

The angular distributions obtained are shown in Fig. 1 and Fig. 2. Data are normalized, for the present, to the best χ^2 fitted elastic scattering cross sections by optical model calculations.[1] The angular distributions of the $5/2_1^+$ and $3/2_2^+$ states are very similar to each other and to that of the 2^+ state in ^{28}Si, as will be the case, when the former two states are weak-coupling states $[^{28}$Si$(2^+) \otimes (2S_{1/2})]_{5/2^+, 3/2^+}$, which are to be expected.[2,3] However, the cross sections of the two states are reduced considerably, compared with the weak-coupling scheme. Besides, the $3/2_1^+$ state is very enhanced, although this state is considered to be a $2d_{3/2}$ single neutron state.[4] Therefore, the core-coupling component and the single particle one of the wave function may have mixed with each other in the two states. The summed cross section of the three states, $3/2_1^+$, $5/2_1^+$, and $3/2_2^+$, is, however, reduced by about 30 %, compared with that of the 2^+ state in ^{28}Si. This reduction may be ascribed to the blocking effect. To study this effect further, the inelastic scattering experiments from other targets, for example, ^{88}Sr and ^{89}Y are in progress.
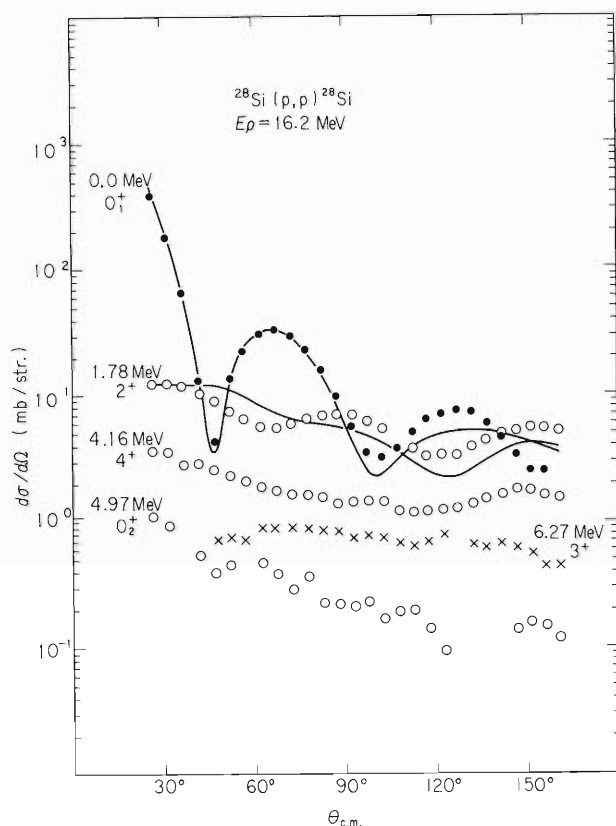
Fig. 1. Angular distributions of the elastic and the inelastic scatterings on ^{28}Si. Solid lines show coupled channel calculation,[5] using following parameters: V=49.7 MeV, W_D=6.54 MeV, V_{SO}=6.5 MeV, r_0=1.2 fm, r_D =1.07 fm, r_{SO} = 1.2 fm, r_C = 1.25 fm, a_0 =0.625 fm, a_D =0.585 fm, a_{SO} =0.625 fm, β_2=−0.46.
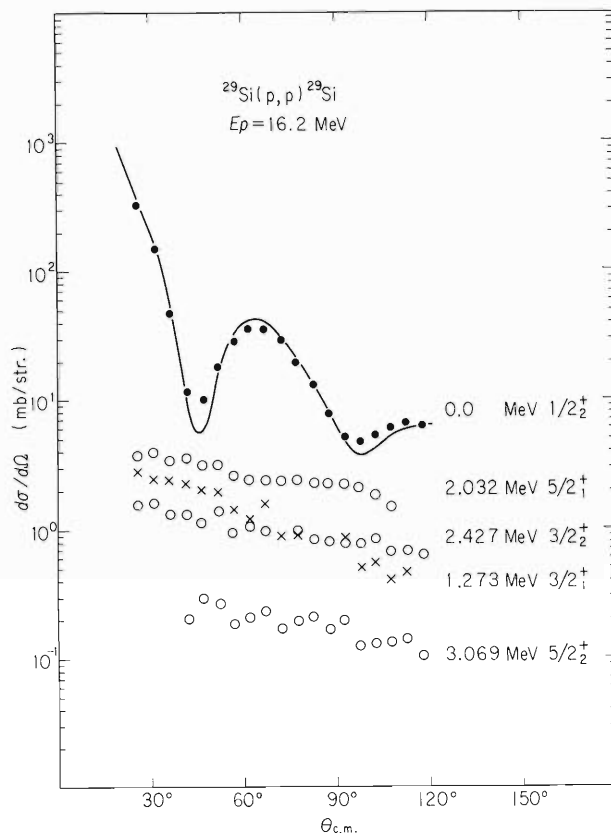
Fig. 2. Angular distributions of the elastic and the inelastic scatterings on ^{29}Si. Solid line shows optical model calculation, using the same parameters of the potential for ^{28}Si.

References

1)   T. Wada: Reports I.P.C.R., (in Japanese), 46, 21 (1970).

2)   B. Castel, K. W. C. Stewart, and M. Harvey: Can. J. Phys., 48, 1490 (1970).

3)   W. R. Coker, T. Udagawa, and G. W. Hoffmann: Phy. Rev., C10, 1792 (1974).

4)   M. C. Mermaz, C. A. Whitten, J. W. Chomin, A. J. Howard, and D. A. Bromley: ibid., C4, 1778 (1971).

5)   T. Wada and S. Yamaji: Sci. Papers I.P.C.R., 68, 65 (1974).

4-2. Study of the ^{54}Fe (d, p)^{55}Fe Reaction at 24 MeV

N. Kishida,* N. Nakanishi, Y. Toba, and H. Ohnuma

Lee and Schiffer[1] observed a very pronounced J-dependence in (d, p) angular distributions in the region of incident deuteron energies around 12 MeV. Such effects have been reproduced to some extent by the distorted wave Born approximation (DWBA) calculations. Yntema and Ohnuma[2] investigated the ^{54}Fe(d, p)^{55}Fe reaction at E_d = 23 MeV. They had to use very large nonlocality parameters in optical potentials to obtain reasonable fits to experimental angular distributions.

We have studied the ^{54}Fe(d, p)^{55}Fe reaction with the 23.80 MeV deuteron beam from the cyclotron. Reaction products were measured with two ΔE-E Si counter telescopes and particle identification systems. The target was a 0.5 mg/cm² thick metallic foil of enriched (97.12 %) ^{54}Fe, and was set with its normal making an angle of 45° to the beam. Overall energy resolution was about 100 keV for both systems. Angular distributions were observed in the
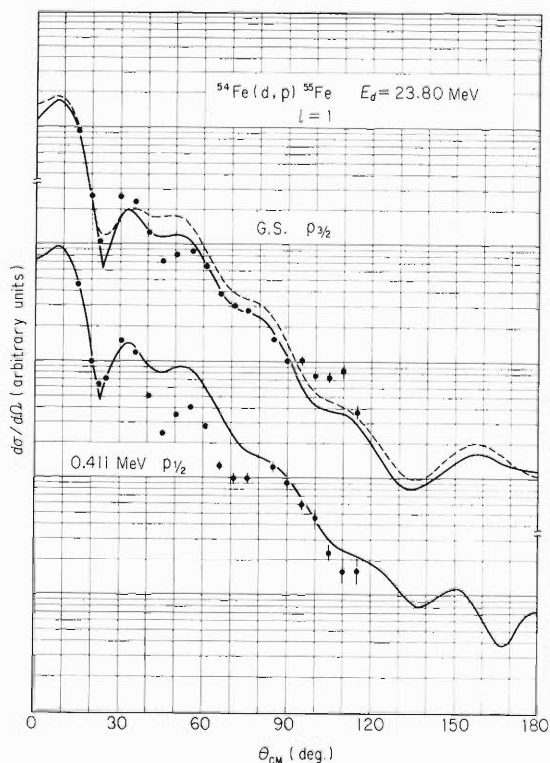
Fig. 1. Angular distributions for the ground state (3/2⁻) and the 0.411 MeV state (1/2⁻). FRNL and ZRL DWBA calculations are shown by solid and dashed lines, respectively.
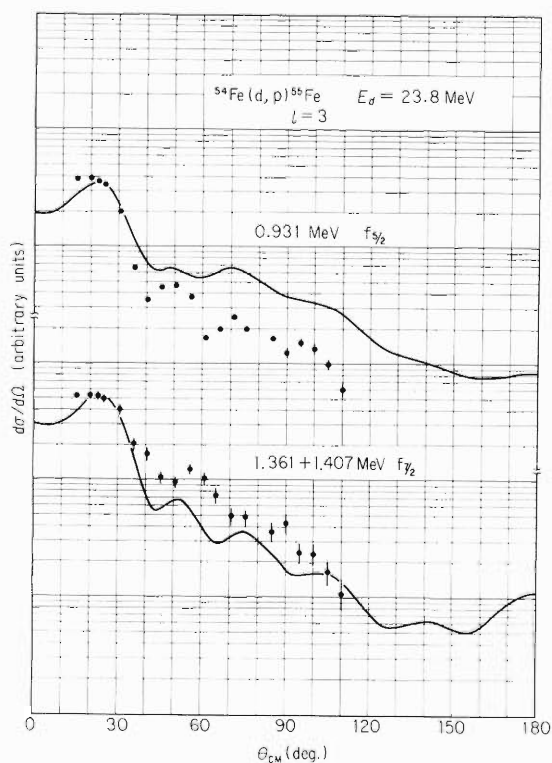
Fig. 2. Angular distributions for the 0.931 MeV state (5/2⁻) and 1.361+1.407 MeV states (7/2⁻) solid lines are FRNL calculations.

range of angles between 15° and 115° in step of 5°. The angular distribution of the elastic scattering was also measured simultaneously, and was used to check optical model parameters for DWBA calculations and target thickness.

Angular distributions obtained are shown in Figs. 1 and 2 together with DWBA calculations. Optical model parameters used in the calculations are given in Table 1. The deuteron optical potential parameters are those obtained with the code ELAST2[3] so as to reproduce the elastic angular distribution obtained in the present work. The proton parameters are those used in Ref. 4. Calculations were made with zero-range local potential (ZRL) and finite-range and non-local potential corrections (FRNL) within the framework of the local energy approximation. Finite-range parameter of 0.658, and nonlocality parameters of 0.54 for a deuteron and 0.85 for a proton were used in FRNL calculations. Form factors were calculated with conventional well-depth description of the separation energy method. All the DWBA calculations are made by DWUCK4[5] using the HITAC-8700 computer at Tokyo Inst. Technology.

In contrast to low energy works, there is no marked difference between the angular distributions for the ground state ($P_{3/2}$) and for the 0.411 MeV 1st excited state ($P_{1/2}$) (Fig. 1). On the other hand, in the case of $\ell = 3$ transitions (Fig. 2), the $f_{5/2}$ angular distribution is shifted forward relative to one of the $f_{7/2}$ state. Present results show that DWBA calculations can not reproduce well the experimental angular distribution.

Table 1. Optical model parameters used in the DWBA calculations.

		d	p	n
V_0	(MeV)	76.97	50.40	a)
r_0	(fm)	1.292	1.111	1.25
a_0	(fm)	0.594	0.790	0.65
W_0	(MeV)	—	2.99	—
r_0	(fm)	—	1.296	—
a_0	(fm)	—	0.616	—
W_0	(MeV)	11.85	4.35	—
r_0	(fm)	1.040	1.397	—
a_0	(fm)	1.016	0.545	—
V_{S_0}	(MeV)	5.67	6.73	$\lambda=25$ b)
r_{S_0}	(fm)	1.024	0.958	—
a_{S_0}	(fm)	0.558	0.709	—
r_C	(fm)	1.3	1.12	—
NLOC		0.54	0.85	

a) Adjusted to give binding equal to separation energy.
b) Spin-orbit coupling of λ times the Thomas term.

References

1) L. L. Lee, Jr. and J. P. Schiffer: Phys. Rev. Lett., 12, 108 (1964).

2) J. L. Yntema and H. Ohnuma: ibid., 19, 1341 (1967).

3) M. Igarashi: INS-PT-26 (1970).

4) P. D. Geaves, V. Hnizdo, J. Lowe, and O. Karban: Nucl. Phys., A179, 1 (1972).

5) P. D. Kunz: Private communication.

4-3. Particle-Particle Correlation in Heavy Ion Reaction

H. Kamitsubo, M. Ishihara, T. Shimoda, T. Fukuda

T. Motobayashi, T. Ooi, and I. Kohno

Heavy ion induced reactions at incident energies well above the Coulomb barrier have revealed a vriety of new phenomena in reaction mechanism by the systematic studies.[1] In these processes multinucleon transfer reactions accompanied by large negative Q values are dominant and are called quasi elastic and deeply inelastic collisions. Because of considerable amount of energy transfer, emission of a third particle in addition to the usual binary reaction products is often possible in deeply inelastic collisions. In fact, a measurement[2] of γ ray multiplicities has indicated a considerable rate of α emission in such processes.

To see the reaction mechanism of deeply inelastic collisions, we measured particle-particle correlation between the light reaction products and p's or α's in a bonbardment of
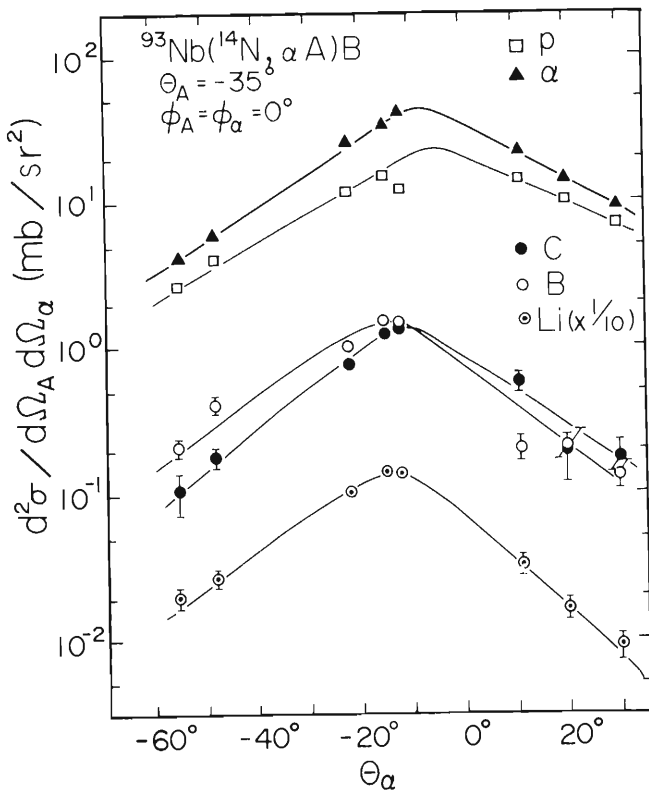
Fig. 1. Energy integrated cross sections for α's coincident with particle A's at $\theta_A = -35°$, $\phi_A = 0°$. A's are p, α Li, B, and C. Abscissa is the laboratory angle of α's.
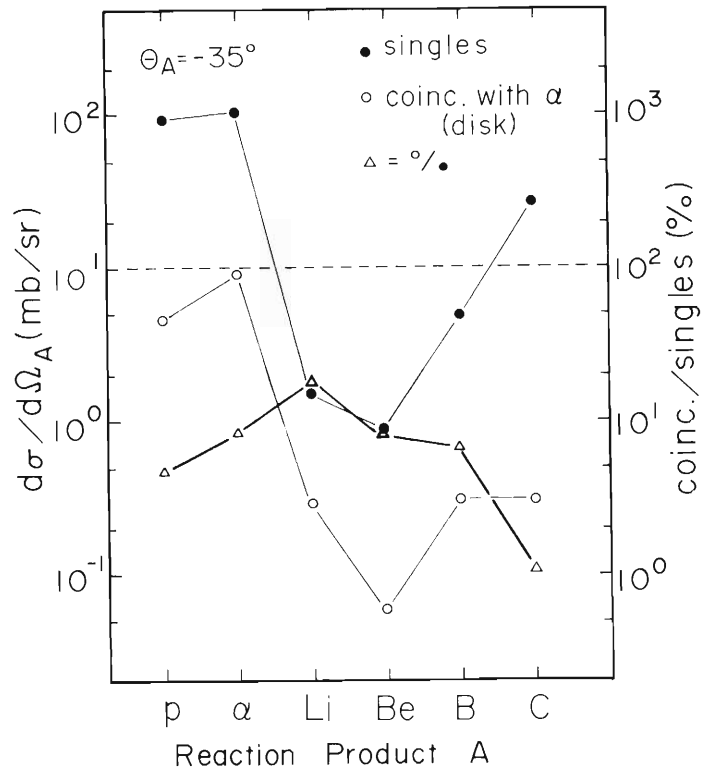
Fig. 2. Closed circles are cross sections for multi-nucleon transfer reactions at $\theta_{lab} = -35°$. Open circles are cross sections for multi-nucleon transfer reactions at $\theta_{lab.} = -35°$ accompanying secondary emission of α's. Triangles are ratios of the two quantities.

a ^{93}Nb foil (4.0 mg/cm^2) with 95 MeV ^{14}N ions from the cyclotron. The light reaction products, C, B, Li, α and p were detected and identified with a ΔE-E counter telescope of 30 and 2000 μm Si detectors fixed at θ_{lab} = -35° and -42°. Coincident p's and α's were detected with a similar telescope, which was moved and located at several angles between θ_{lab} = +30° and -65° and at θ_{lab} = 160° in the same reaction plane as the fixed telescope (ϕ_{lab} = 0°). To see the ϕ dependence we also measured correlation at θ_{lab} = -15° and ϕ_{lab} = 14°, 18° and 26°. A 90 μm aluminum absorber was placed in front of the latter telescope to cut off the particles of elastic scattering. The fixed and movable telescopes subtended solid angles of 7.9 and 4.7 msr, respectively. Two pairs of energy and identified particle spectra and time correlation were registered event by event in a computer system.

In Fig. 1 energy integrated cross sections for α's coincident with C, B, Li, α, and p on the fixed telescope are plotted versus the lab angle of the movable telescope. The angular correlations show curves of almost symmetric shape with an exponential slope. The center angles coincide neither with the emission angles of light products nor recoil angles of heavy products. The data at θ_{lab} = 160° suggest that the yields decrease continuously for larger angles. The results suggest that the third particles were emitted with a considerably short reaction time. It is interesting to note a trend that the half width of the distribution becomes wider as the product becomes lighter from C to p. We also observed that the center angles of B and Li data shift about 7° to the fixed telescope when it was placed at θ_{lab} = -42°.

The cross sections (σ^{α}_{coin}) for multi-nucleon transfer reactions at -35° accompanying secondary emission of α's can be estimated by integrating the angular correlations over angles of θ_α and ϕ_α. The ratios of σ^{α}_{coin} to σ_{single}, cross sections for multi-nucleon transfer reactions at -35°, are shown in Fig. 2.
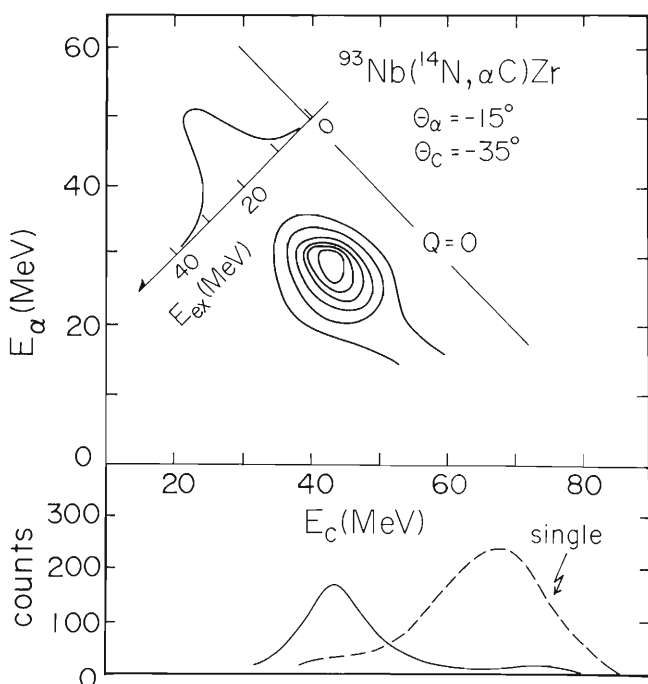
Fig. 3. Energy contour map of C and α. The ordinate is laboratory energy of α, and the abscissa is that of C. The inclined line is kinematicaly allowed one in the case of zero reaction Q-value. At the left above, distribution of Q-value is shown. Energy spectrum of C emitted independently of α as well as spectrum coincident with α is below the contour map.

We have also measured energy correlation in those reactions. Figure 3 shows the result of energy correlation, C at $-35°$ and α at $-15°$ in the same reaction plane. We note that the multi-nucleon transfer reactions accompanying α emission are dominant in large energy transfer region, namely deeply inelastic collisions from the comparison of the energy spectrum of single events with the projection of energy contour map to the C energy axis.

References

1)   V. V. Volkov: Proc. Int. Conf. on Reactions between Complex Nuclei, Nashville, 2, 363 (1974).

2)   M. Ishihara, T. Numao, T. Fukuda, K. Tanaka, and T. Inamura: Proc. Symp. on Macroscopic Features of Heavy-Ion Collisions, Argonne, II, 617 (1976).

4-4. Gamma Ray Multiplicities for Deep Inelastic and Quasi-elastic Processes

M. Ishihara, T. Numao,* T. Fukuda,

K. Tanaka, and T. Inamura

It has been shown that processes called quasi-elastic (QE) and deep inelastic (DI) collisions exist in the reactions induced by heavy ions with energies well above the Coulomb barriers.[1] It is interesting to know what angular momenta are brought into the fragments emitted in these processes. Multiplicities of γ-rays from the fragments will provide information on the angular momenta in question. Accordingly, an experiment was carried out to measure the γ-ray multiplicities for QE and DI in the bombardment of ^{93}Nb, ^{169}Tm, and ^{181}Ta with 90 and 120 MeV ^{14}N.
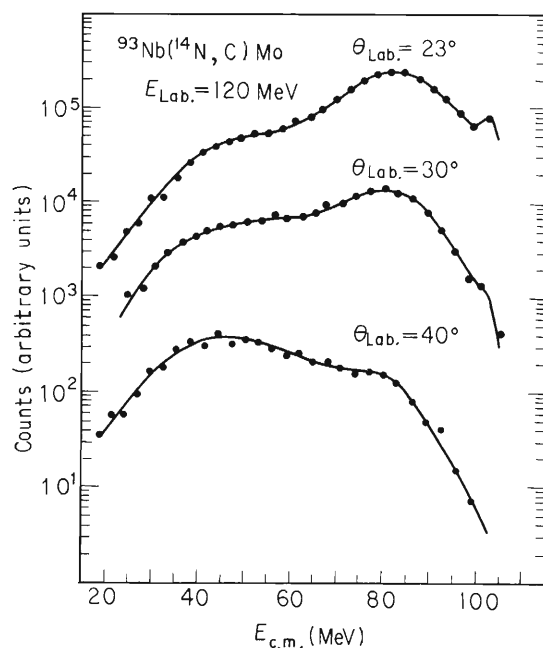
Fig. 1. Energy spectra of carbon from the ^{93}Nb(^{14}N,C) Mo reaction at $E_{lab} = 120$ MeV.
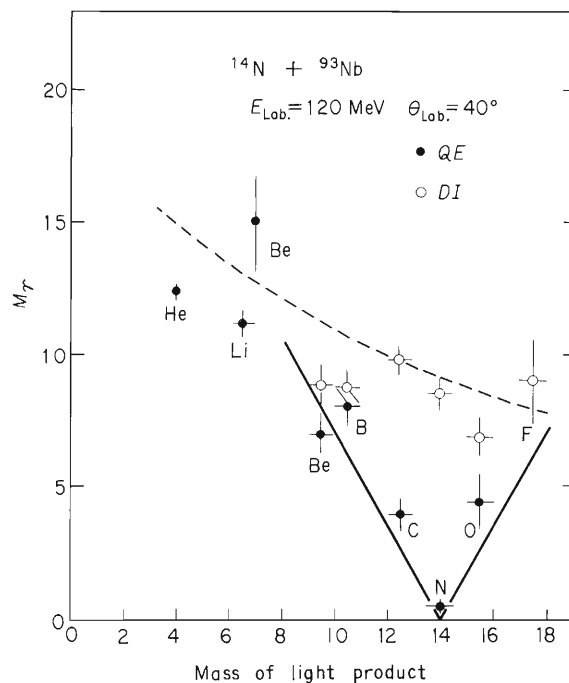
Fig. 2. The γ-multiplicity M_γ versus the light fragments emitted in the bombardment of ^{93}Nb with 120 MeV ^{14}N : The dotted line is obtained from the model of sticking motion[3] to be compared with the DI result. The solid line is from the model of grazing collision[4] to be compared with the QE result.

* University of Tokyo.

We measured energy and identified particle spectra in singles and in coincidence with γ-rays for each reaction. The γ-ray multiplicity M_γ is determined by $M_\gamma = N_{coin}(E_f)/\Omega_\gamma N_{sing}(E_f)$, where N_{sing} and N_{coin} represent singles and coincidence counting rates of the identified particles with energy E_f, respectively; and Ω_γ is the solid angle subtended by the γ-counter. Details of this technique were described in Ref. 2.

Figure 1 shows energy spectra of carbon from the $^{93}Nb(^{14}N, C)Mo$ reaction at E_{lab} = 120 MeV. It is seen that the QE humps (higher energy peak) gradually diminishes, while the DI hump (lower energy peak) becomes dominant towards backward angles.

The multiplicity M_γ can be related to the initial spin l of the residual nucleus by $I = fM_\gamma$. At the moment, we have no accurate knowledge about angular-momentum dissipation due to particle emission. However, we have found that an effective f-value of 2.4 ℏ is needed to account for the total spin dissipation by γ-rays and particles. We shall tentatively use this value in the analysis.

Figure 2 shows a typical plot of Mγ measured at the centres of QE and DI humps versus mass of the light fragments. The dotted line represents the multiplicities expected from the sticking motion of colliding nuclei;[3] this line is to be compared with the DI result. The solid line represents the result obtained by assuming the velocity of transfered nucleons to be the same as that of the projectile.[4] This is compared with the QE result. It is interesting to note that the M_γ values for DI and QE processes are described well by these simple models. Similar results were obtained for the Tm and Ta targets.

References

1)   M. Lefort: Rep. Prog. Phys., _39_, 129 (1976).

2)   T. Numao, M. Ishihara, T. Inamura, and T. Fukuda: IPCR Cyclotron Prog. Rep., _9_, 13 (1975).

3)   J. Wilczynski: Phys. Lett. _47B_, 484 (1973).

4)   D. M. Brink: ibid., _40B_, 37 (1972).

4-5. Complete Fusion Cross Section Measurement *by* Beam Attenuation Method

T. Fukuda, M. Ishihara, T. Inamura,

T. Numao,* T. Shimoda, and T. Nomura

Recently, complete fusion cross sections σ_{cf} for heavy ion induced reactions have extensively been measured to determine the critical angular momentum ℓ_{cr}. However, the methods using mica track detectors or counter telescopes are not always reliable in discrimination of fusion reaction events from direct reaction ones and have some difficulty in application to heavier targets.

We have developed a new technique of σ_{cf} measurement, which is simple and free from above mentioned difficulties. As mentioned in Ref. 1 the basic principle of the method is similar to that of the beam attenuation method[2] used for the measurement of the proton total reaction cross section. As shown in Fig. 1, the set-up consists of two beam defining counters in front of the target, a fixed backward annular counter (C4) and a movable stopping counter (C3) positioned downstream the beam. The stopping counter detected projectiles which passed through the target or were elastically scattered and the whole light charged particles of reaction products emitted in forward direction. Heavy fragments like evaporation residues were stopped by a thin aluminum foil in front of the stopping counter. The solid angle of the stopping counter was chosen to cover a forward semisphere large enough to register the whole direct reaction events.
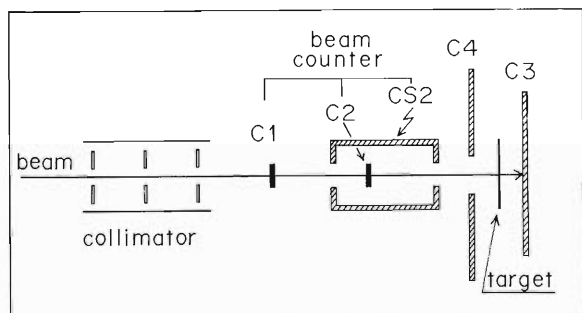
Fig. 1. The schematic experimental set-up: C1, C2, CS2, C3, and C4 are plastic counters.
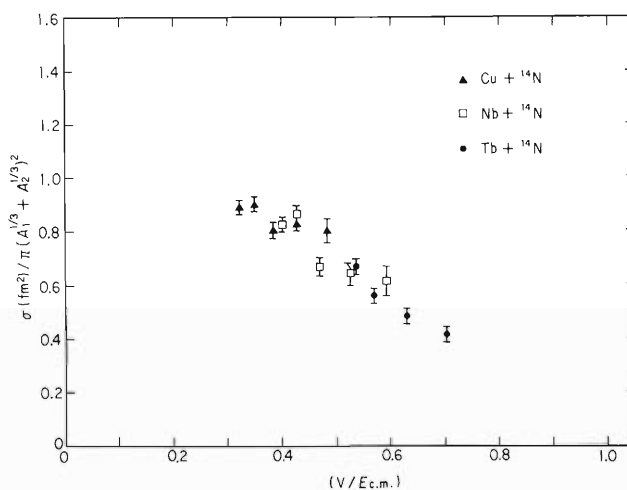
Fig. 2. Energy dependence of the complete fusion cross section. $E_{c.m.}$ is the center of mass energy and V equals to $Z_1 Z_2 e^2 / r_c (A_1^{1/3} + A_2^{1/3})$ with $r_c = 1.47$ fm.

* University of Tokyo.

In principle, the difference in the number of counts between the beam defining counter and the stopping counter gives the cross section for fusion events without charged particle evaporation. Since the fused nucleus frequently decays via charged particle evaporations, we have to make the correction for such evaporation processes.

In the case of the lighter target like Cu or ^{93}Nb, almost all of the fused nucleus decay via charged particle evaporations at the incident energies used, so that we made the following consideration: The cross section of fused nucleus decaying via fission should be negligibly small in our case. The differences in the number of counts between the beam defining counter and the stopping counter, N_f, is proportional to

$$\sigma_{cf} - \sum_{n=1} \left\{ 1 - (1 - \Omega_f)^n \right\} \sigma_n,$$

and the coincidence events between the backward counter and the above differences, N_b, is proportional to

$$\sum_{n=1} \left\{ (1 - \Omega_f)^n - (1 - \Omega_f - \Omega_b)^n \right\} \sigma_n,$$

where σ_1 denotes the cross section of fused nucleus decaying via emission of one charged particle, neutrons and γ-rays, σ_2 denotes the cross section of fused nucleus decaying via two charged particles, neutrons and γ-rays, and so on. Ω_f and Ω_b denote the solid angle of C3 and C4 counter respectively. The sets of N_f and N_b are measured as a function of Ω_f, Ω_b being fixed. Then σ_{cf}, σ_1, σ_2 etc. can be deduced as parameters from χ^2-fits.

We measured σ_{cf} for the reactions of ^{14}N ions on Cu(2.47 mg/cm^2), ^{93}Nb(2.38 mg/cm^2) and ^{159}Tb(3.76 mg/cm^2) targets at E_{lab} = 78, 88, 99, 109, 118 MeV. Figure 2 shows the energy dependence of the measured complete fusion cross section. The experimental data are in accord with the Bass model[3] with a_s = 17.0 MeV, d = 1.35 fm and R_{12} = 1.02 × ($A_1^{1/3}$ + $A_2^{1/3}$) fm, where a_s is the surface energy parameter of the liquid drop model mass formula, d is the range of the interaction and R_{12} is the cut off radius. We did not find such a kinking effect as predicted by the model of Glas & Mosel[4] with the Orsay type potential and the critical distance of approach R_{cr} = 1.00 × ($A_1^{1/3}$ + $A_2^{1/3}$) fm.

We also measured σ_{cf} for the reaction of ^{16}O ions on Cu, ^{93}Nb and ^{159}Tb targets at E_{lab} = 86, 97, 112 MeV. The analysis of this experiment is now in progress.

References

1) T. Fukuda, M. Ishihara, T. Inamura, T. Numao, and T. Nomura: IPCR Cyclotron Progr. Rep., 9, 15 (1975).

2) J. J. H. Menet, E. E. Gross, J. J. Malanify, and A. Zucker: Phys. Rev., C4, 1114 (1971).

3) R. Bass: Phys. Lett., 47B, 139 (1973).

4) D. Glas and U. Mosel: Nucl. Phys., A237, 429 (1975).

4-6. Measurement of the Efficiency of ^{8}Be Detection by Position Sensitive Detector and Study of the ^{12}C $(\alpha, ^8Be)^8$Be Reaction

T. Ooi, T. Motobayashi, K. Katori, and I. Kohno

A position sensitive detector (PSD) can provide large detection efficiency and good resolution of energy in detecting ^{8}Be nuclei.[1],[2]

The detection efficiencies were measured by observing ^{7}Be and ^{8}Be particles emitted from the ^{12}C(^{3}He, ^{7}Be)^{8}Be reaction induced by ^{3}He^{2+} beams from the cyclotron. The ^{7}Be particles were identified and detected by a ΔE-E counter telescope and ^{8}Be particles by a counter telescope of PSD and ΔE detector with divided rectangular collimator. The efficiency is obtained as the ratio of ^{8}Be yield to ^{7}Be yield, which is normalized by the incident beam intensity and the solid angle subtended by the detector.
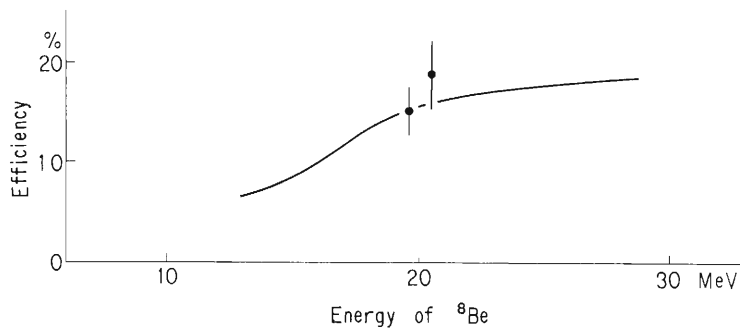
Fig. 1. Efficiency for the detection of ^{8}Be(g.s.) nuclei vs energy of ^{8}Be nuclei. The solid curve is based on calculation. The dots represent the experimental results.
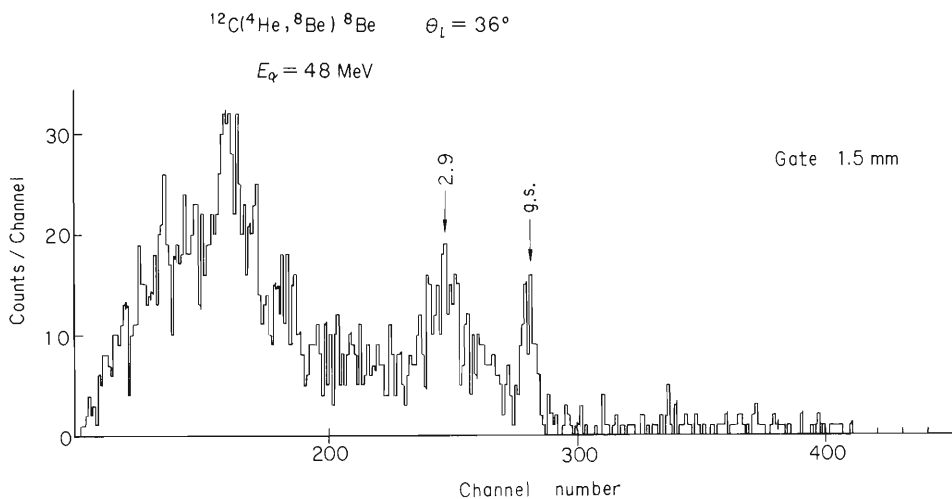
Fig. 2. Energy spectrum from the ^{12}C(α, ^{8}Be)^{8}Be reaction.

The experimental results are compared with the calculated curve in Fig. 1, where the efficiency is plotted versus the kinetic energy of ^{8}Be nuclei. The results are in good agreement with the calculated curve.

The differential cross section for the ^{12}C(α, ^{8}Be(g.s.))^{8}Be(g.s.) reaction at bombarding energy of 48 MeV was measured by the PSD system. The experiment was performed with ^{4}He^{2+} beams from the cyclotron. The target was a self-supporting foil of ^{12}C of 100 μg/cm^2 in thickness.

Figure 2 shows typical energy spectrum for the ^{12}C(α, ^{8}Be)^{8}Be reaction. The energy resolution was about 400 keV at FWHM, which is due mainly to kinematical broadening. The differential cross sections are tabulated in Table 1.

Table 1. Differential cross section for the ^{12}C(α, ^{8}Be)^{8}Be reaction.

^{12}C(α, ^{8}Be)^{8}Be $E_\alpha = 48$ MeV

Θ_{CM}	$\left(\dfrac{d\sigma}{d\Omega}\right)_{CM}$ (mb/sr)		
	Gate width = 1 mm	1.5 mm	2 mm
27.5	0.031 ± 0.010	0.033 ± 0.011	0.028 ± 0.014
30.7	0.059 ± 0.010	0.057 ± 0.012	0.062 ± 0.023
35.6	0.042 ± 0.009	0.043 ± 0.011	0.049 ± 0.013
40.5	0.025 ± 0.009	0.027 ± 0.009	0.029 ± 0.012
45.3	0.039 ± 0.009	0.039 ± 0.011	0.038 ± 0.013
50.1	0.049 ± 0.007	0.045 ± 0.007	0.049 ± 0.009
54.9	0.070 ± 0.009	0.068 ± 0.011	0.070 ± 0.013
59.6	0.137 ± 0.011	0.114 ± 0.014	0.106 ± 0.017
64.3	0.130 ± 0.013	0.124 ± 0.014	0.130 ± 0.017
68.9	0.060 ± 0.007	0.055 ± 0.008	0.055 ± 0.010
73.4	0.043 ± 0.011	0.046 ± 0.012	0.041 ± 0.015
77.9	0.043 ± 0.006	0.038 ± 0.007	0.034 ± 0.008
82.4	0.042 ± 0.007	0.043 ± 0.008	0.047 ± 0.009
86.8	0.046 ± 0.007	0.043 ± 0.008	0.061 ± 0.011

References

1) T. Ooi, T. Motobayashi, K. Katori, and I. Kohno: IPCR Cyclotron Progr. Rep., <u>10</u>, 68 (1976).

2) G. J. Wozniak, N. A. Jelley, and Joseph Cerney: Nucl. Instr. Meth., <u>120</u>, 29 (1976).

4-7. α-Transfer Reactions between 1p or 2s-1d Shell Nuclei

T. Motobayashi, I. Kohno, T. Ooi, and S. Nakajima

To investigate the reaction mechanism of α-transfer reactions induced by heavy ions, angular distributions for α-transfer reactions were measured for several targets and projectiles of 1p or 2s-1d shell nuclei, namely ^{10}B, ^{12}C, ^{14}N, ^{16}O, and ^{20}Ne. The structure of these nuclei are well studied theoretically.[1],[2] Especially in the case of ^{20}Ne and ^{16}O, α-cluster structure has been well investigated in a microscopic way by the cluster model.[3] Hence it is suitable to use these nuclei for studying the mechanism of the α-transfer reactions.

Reactions studied are listed in Table 1. The beams of ^{14}N^{4+} and ^{16}O^{5+} from the cyclotron were used. Gas target was employed for ^{16}O and ^{20}Ne, and ^{10}B target was made by evaporation.[4] Outgoing particles were identified with a ΔE-E SSD counter telescope in which E counter was a position sensitive detector. A four slit collimators in front of the telescope defined four position windows 1° apart from each other and made it possible to measure the

Table 1. The list of the reactions and the optical potential parameters used in the DWBA calculations. In the column of J^π, right hand side corresponds to the spin and the parity of the ejectile and left hand side the residual nuclei. V and W (in MeV) are the real and the imaginary well depth of the optical potentials.

Reactions	E_L (MeV)	J^π		E_x (MeV)	V (MeV)	W (MeV)
^{16}O(^{14}N, ^{10}B)^{20}Ne	76.2	3^+	0^+	0.0	75	10
		3^+	2^+	1.63		
		1^+	2^+	2.35		
		3^+	4^+	4.25		
^{10}B(^{14}N, ^{10}B)^{14}N	$\binom{73.9}{93.6}$	3^+	1^+	0.0	60	20
		1_1^+	1^+	0.72		
		1_2^+	1^+	2.16		
^{20}Ne(^{16}O, ^{20}Ne)^{16}O	94.8	0^+	0^+	0.0	65	15
		2^+	0^+	1.63		
		4^+	0^+	4.25		
^{12}C(^{14}N, ^{10}B)^{16}O	78.8	3^+	0^+	0.0	65	20
		1_1^+	0^+	0.72		
		1_2^+	0^+	2.16		
^{16}O(^{16}O, ^{12}C)^{20}Ne	95.2	0^+	0^+	0.0	65	15
		0^+	2^+	1.63		

reaction products at 4 angles simultaneously. Details of the gas target and the counter telescope are discussed elswhere[5],[6] in this progress report.

Some examples of energy spectra are shown in Fig. 1. Energy resolutions were 400 keV to 1 MeV, the main contribution to which is the energy spread of the ions in the entrance and exit windows (nickel or mylar foils) of the gas target (in the case gas target is used) or the kinematical broadening of energy of the scattered particles (in the case foil target is used). The spectrum shape was fitted by the skewed Gaussian form by a program SPFIT-4[7] on a DDP 124 computer.

Exact finite range DWBA calculations for α-transfer reactions were performed on some cases with a computer code SATURN-MARS-2[8] which was revised to be suitable for α-transfer reactions by Matsuura (IPCR). Optical potentials were determined to fit the angular distributions of the elastic scatterings of incident channel for each reaction. Only the depth of the real and imaginary parts were searched and the radius and the diffuseness of both real and imaginary
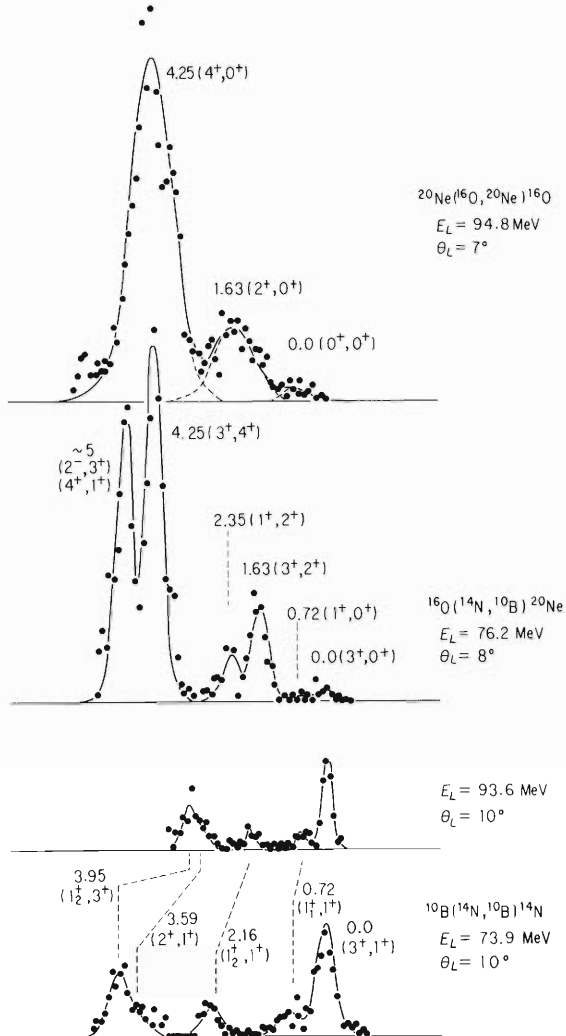
Fig. 1. Energy spectra of some α-transfer reactions. The solid lines correspond to the skewed Gaussian fit.
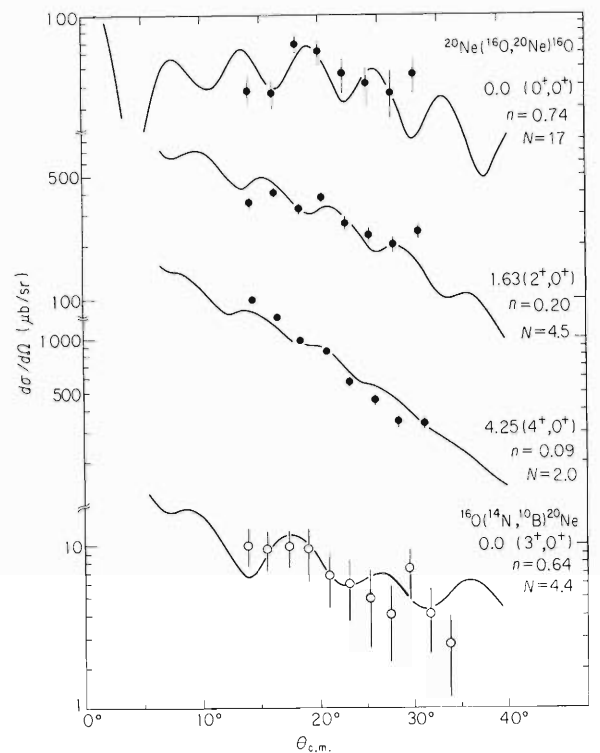
Fig. 2. Angular distributions of some α-transfer reactions. The solid lines correspond to the exact finite range DWBA calculations with the normalization constants written in the figure.

parts were taken to be the same for all cases[9] (r_R = 1.21 fm, r_I = 1.35 fm, a_R = 0.48 fm, and a_I = 0.25 fm). The DWBA form factors were constructed phenomenologically, namely from the cluster wave functions which were solved in Woods-Saxon wells (r_0 = 1.3 fm and a = 0.7 fm, the depth was determined so as to reproduce the binding energy of the α-core system). The DWBA cross section for stripping type reaction A(a, b)B is written as

$$\frac{d\sigma}{d\Omega} = NS_1 S_2 \cdot \left(\frac{d\sigma}{d\Omega}\right)_{SM},$$

where $S_1 = |\langle a | \} b, \alpha \rangle|^2$ and $S_2 = |\langle B | \} A, \alpha \rangle|^2$ are the spectroscopic factors of α-cluster in the projectile and the residual nucleus respectively, and N is a normalization constant which is necessary to fit the calculated results to the experimental data.

Some results of DWBA calculations are shown in Fig. 2 in which N has the meaning mentioned above when S_1 and S_2 were taken to be the shell model values listed in Table 2, and n denotes the overall normalization $NS_1 S_2$. The normalization constant N takes various values depending on the combination of the projectile and target, and on the spin of the final state. It is very interesting to see if these tendencies are reproduced by constructing the form factors of DWBA from the microscopic wave function.

Systems	J_a^π	J_b^π	ℓ	S
^{20}Ne $\longleftrightarrow$ ^{16}O + α	0^+	0^+	0	0.21[a]
	2^+	0^+	2	0.21
	4^+	0^+	4	0.19
^{16}O $\longleftrightarrow$ ^{12}C + α	0^+	0^+	0	0.23[b]
^{14}N $\longleftrightarrow$ ^{10}B + α	1^+	3^+	2	0.012[b]
			4	0.69
	1^+	1_1^+	0	0.004
			2	0.13
	1^+	1_2^+	0	0.082
			2	0.094

Table 2. Spectroscopic factors for the α-cluster in ^{20}Ne, ^{16}O, and ^{14}N. J_a^π corresponds to the spin and the parity of the nuclei, ^{20}Ne, ^{16}O, and ^{14}N, and J_b^π corresponds to those of the core, ^{16}O, ^{12}C, and ^{10}B respectively. ℓ is the orbital angular momentum between the α-cluster and the core nucleus.

a) Ref. 2.   b) Ref. 1.

References

1)   D. Kurath: Phys. Rev., C 7, 1390 (1973).

2)   Y. Akiyama, A. Arima, and T. Sebe: Nucl. Phys., A138, 273 (1969).

3)   T. Suzuki and K. Ikeda: Prog. Theor. Phys., 51, 1621 (1974); T. Matsuse and
     M. Kamimura: ibid., 49, 1765 (1973).

4)   Fabricated by M. Mihara (IPCR; Work Shop).

5)   T. Motobayashi: IPCR Cyclotron Progr. Rep., 10, 70 (1976).

6)   T. Motobayashi: ibid., p.72.

7)   Revised from the code SPFIT-3 (developed by T. Wada (IPCR): unpublished).

8)   T. Tamura and K. S. Low: Comput. Phys. Commun., 8, 349 (1974).

9)   I. Kohno, S. Nakajima, T. Tonuma, and M. Odera: J. Phys. Soc. Japan, 30, 910 (1971).

4-8. Critical Angular Momentum in ^{10}Be + ^{16}O Compound Reactions

I. Kohno, T. Motobayashi, T. Ooi, M. Ishihara,

T. Numao,* T. Fukuda, and S. M. Lee**

As was reported,[1] in the ^{12}C(^{14}N, ^{6}Li)^{20}Ne reaction, the compound nucleus formation is the main process at incident energies between 20 and 90 MeV, and the critical angular momenta (J_{cr}) in the compound formation have been derived from Hausser-Feshbach (HF) analysis of cross sections for individual levels in the relevant outgoing channels.

In order to see the behavior of J_{cr} in the other incident channel, we have studied the ^{10}B(^{16}O, ^{6}Li)^{20}Ne reaction at energies of 84.7, 90.6, and 98.8 MeV.

The experiments were performed with the ^{16}O^{5+} beams from the cyclotron. The target of ^{10}B was a self-supporting foil of about 87 μg/cm^2 in thickness.

Excitation functions for some ^{20}Ne levels measured at 8° are presented in Fig. 1. Solid curves indicate the HF calculation with J_{cr} values which were chosen to give the best fit to the experimental data. J_{cr} values are listed in Table 1. From the present analysis we obtained the J_{cr} values of 19, 20, and 21ħ at E_{lab} = 84.7, 90.6, and 98.8 MeV, respectively. These J_{cr} values
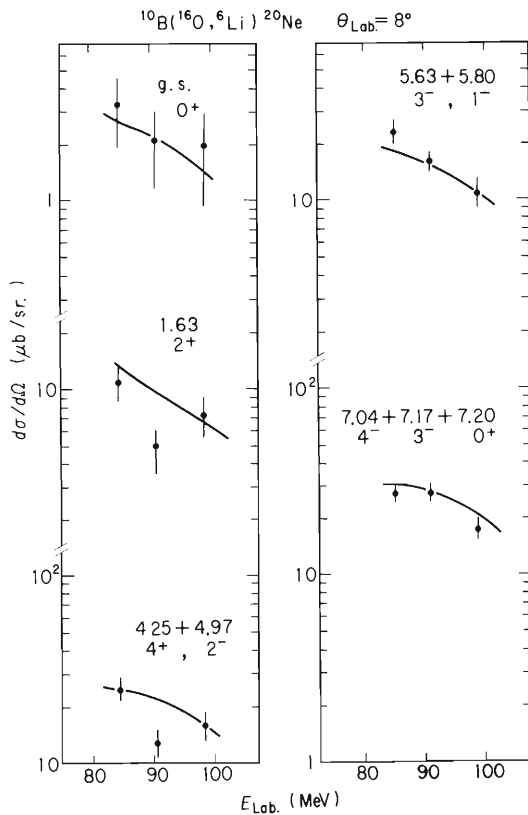
Fig. 1. Excitation functions for some ^{20}Ne states measured at 8° in the laboratory system for the ^{10}B(^{16}O, ^{6}Li)^{20}Ne reaction.

* Faculty of Science, University of Tokyo.

** University of Strasbourg.

Table 1. J_{cr}, J_{gr}, and σ_{fus} values obtained from experimental data. σ_{fus} indicates a fusion cross section.

Incident energy (MeV)	E_{CM} (MeV)	J_{gr} ($\hbar$)	J_{cr} ($\hbar$)	σ_{fus} (mb)
84.7	32.6	20	19	1170
90.6	34.8	21	20	1200
98.8	38.1	22	21	1220

are smaller than the grazing angular momentum J_{gr} by $1\hbar$. J_{gr} is defined as the angular momentum for which the transmission coefficient of the incident channel is 0.5.

The transmission coefficient was extracted from the optical model parameters which were obtained from fits to measured elastic scattering of ^{16}O from ^{10}B. A set of parameters obtained is as follows: the real well depth V = 65 MeV; the imaginary well depth W = 20 MeV; the diffusivity a_R = 0.48 fm and a_I = 0.25 fm; and the radial parameters r_R = 1.21 fm and r_I = 1.35 fm for the real well and the imaginary well, respectively.

It can be seen in Fig. 1 that considerably good fits to the data for all the outgoing channels in the $^{10}B(^{16}O, {}^6Li)^{20}Ne$ reaction are obtained. This is taken to be a proof of the dominance of the compound process similar to the $^{12}C(^{14}N, {}^6Li)^{20}Ne$ reaction.

Reference

1) T. Ooi, T. Motobayashi, I. Kohno, M. Ishihara, T. Numao, T. Fukuda, and S. M. Lee: IPCR Cyclotron Progr. Rep., 9, 10 (1975);
    C. Volant, M. Conjeaud, S. Harrar, S. M. Lee, A. Lepine, and E. F. Da Silveira: Nucl. Phys., A238, 120 (1975).

4-9. Repeated Neutron Transfer in the Elastic-and Inelastic Scattering of ^{16}O on ^{17}O

B. Imanishi, O. Tanimura,* and H. Ohnishi**

Coupled Channel Analysis of the elastic- and inelastic scatterings, ^{16}O$-^{17}$O and ^{17}O(^{16}O, ^{16}O)^{17}O* (1/2$^+$, 0.871 MeV) (E_{cm} = 11.33, 12.36, 13.43, 14.42, 15.51, and 16.48MeV) has been carried out by the use of the core-exchange model,[1)-3)] where the transfer processes, ^{17}O$^{(*)}$ (= ^{16}O$_1$ + n (0d 5/2 or 1s 1/2)) + ^{16}O$_2$ → ^{16}O$_1$ + ^{17}O$^{(*)}$ (= ^{16}O$_2$+n (0d 5/2 or 1s 1/2)), are assumed. The multi-step processes due to the transfer- and "direct" elementary-processes (see Fig. 1) are found to give important contribution to the inelastic cross sections.
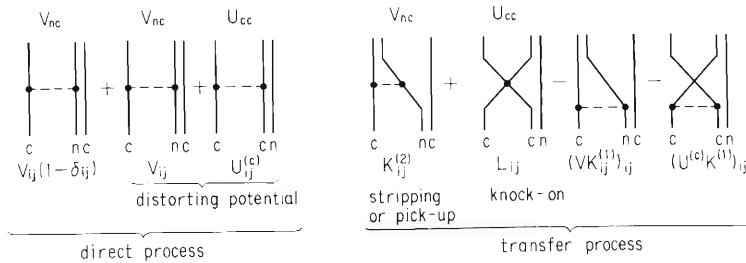
Fig. 1. Elementary processes for the elastic- and inelastic scattering of ^{16}O on ^{17}O by the core-exchange model.

The angular distributions (for example, E_{cm} = 13.43 and 15.51 Mev) calculated by the coupled channel method and by the DWBA method are compared in Fig. 2 with the experimental data of Ref. 3. The solid lines show the results due to the full elementary processes of Fig. 1, while the dotted lines the results from the transfer process only. Similar comparisons are made for the excitation functions at θ_{cm} = 60° and 129° in Fig. 4. Maher's optical potential (r_0 = 1.35fm, a = 0.49fm, V = 17.0 MeV, r_I = 1.27fm, a_I = 0.15fm and W=(0.8+0.2 E_{cm}) MeV), which was obtained from the optical model analysis of ^{16}O$-^{16}$O scattering, has been used in this analysis for the core (^{16}O)-core interaction. The coupled channel analysis shown by the solid lines gives excellent fits to the data both for the angular distributions and for the excitation functions, while the DWBA fails to fit to the data. It should be noted that the coupled channel results based on the transfer process only also agree with the data fairly well.

The results of these analyses can be summarized as follows:

1) The bump observed in the forward angular region is formed to a large part from the multi-step transfer processes, i.e., repeated transfer processes (RTP) of outer neutron between two core-nuclei, ^{16}O's, the RTP's occurring even times. In DWBA prediction this bump is formed mainly by the one-step 'direct' process. However, this contribution is rather small to

* Faculty of Science, Kyoto University.
** Colledge of General Education, Hosei University.

give the bump observed by the experiments.

2) The dominant RTP is the neutron transfer process between the 1s 1/2 orbits of respective ^{16}O-nuclei (see Fig. 4).

3) The RTP's occurring odd times interfere incoherently in the backward angular region

Fig. 2. Angular distributions of the inelastic scattering, ^{17}O(^{16}O,^{16}O)^{17}O*(1/2$^+$, 0.871 MeV) at $E_{cm} = 15.51$ MeV. The curves in the upper half of figure are obtained by DWBA calculations and those in the lower half by coupled channel calculations. The solid lines are due to the full processes, the full-dotted lines due to the transfer process and the dotted line due to the direct process.

Fig. 3. Angular distributions of ^{17}O(^{16}O,^{16}O)^{17}O*(1/2$^+$, 0.871 MeV) calculated by the transfer process only. The solid lines are the results of calculations with full RTP, the full-dotted lines with the one-step process for the transition,

^{16}O$_1$ + ^{17}O(= ^{16}O$_2$ + n (0d 5/2)) $\longrightarrow$ ^{17}O*(^{16}O$_1$ + n (1s 1/2)) + ^{16}O$_2$,

and full RTP for the transition,

^{16}O$_1$ + ^{17}O*(= ^{16}O$_2$ + n (1s 1/2)) $\longrightarrow$ ^{17}O*(^{16}O$_1$ + n (1s 1/2)) + ^{16}O$_2$,

and the dotted lines with one-step process.

with the one-step transfer process, $^{17}O(=^{16}O_1+n\,(0d5/2)) + {}^{16}O_2 \rightarrow {}^{16}O_1 + {}^{17}O* (= {}^{16}O_2+n$ (1s 1/2)).

4) The processes related to direct elementary process interfere destructively in the angular region of $90°\sim120°$ with the one- or multi step transfer processes (see Figs. 2 and 4).
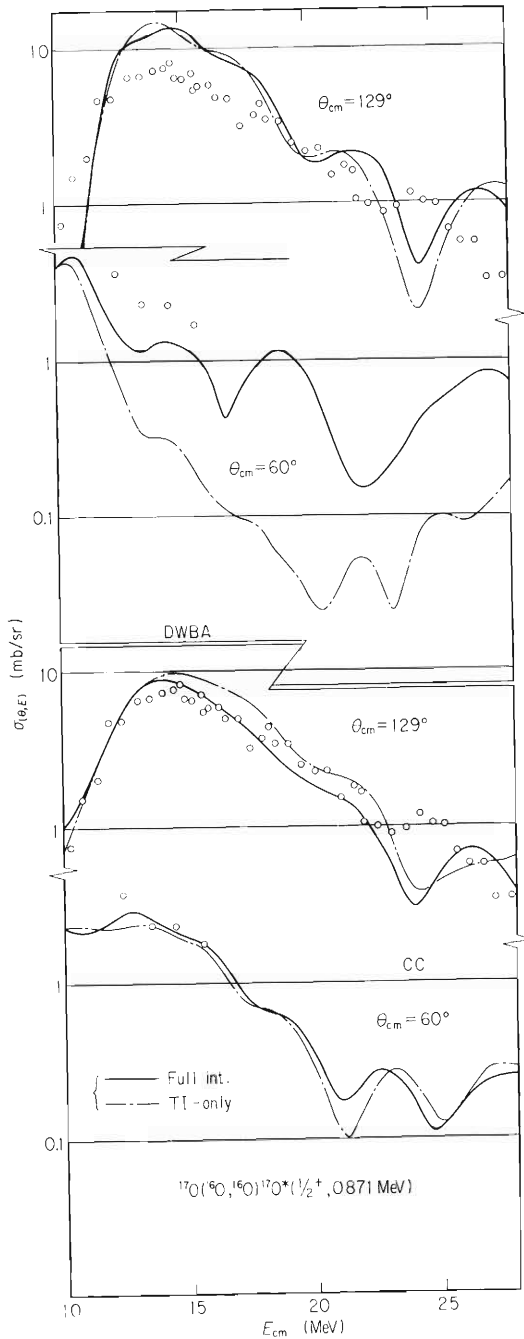
Fig. 4. Excitation functions of the inelastic scattering, $^{17}O(^{16}O,^{16}O)^{17}O*(1/2^+,0.871$ MeV). The curves in the upper half of the figure are obtained by DWBA calculations and those in the lower half by coupled channel calculations. The solid lines are due to the full processes and the full-dotted lines due to the transfer process only. At forward angle, $\theta_{cm}=60°$, both lines due to the coupled channel calculations agree with each other fairly well.

References

1) G. Baur and H. H. Wolter: Phys. Lett., 51B, 205 (1974).

2) B. Imanishi, H. Ohnishi, and O. Tanimura: ibid., 57B, 309 (1975).

3) D. Kolinsky, D. Melnik, U. Smilansky, N. Trautner, B. A. Watson, Y. Horowitz, S. Mordechai, G. Baur, and D. Pelte: Nucl. Phys., A250, 364 (1975).

4) C. K. Gelbke, G. Baur, R. Bock, P. Braun-Munzinger, W. Grechulski, H. L. Harney, and R. Boch: ibid., A219, 253 (1974).

4-10. Nuclear Deformation and Finite Size Effect of Projectile in Inelastic Scattering

T. Matsuura and T. Wada

Macroscopic treatment of inelastic scattering (generalized optical model) is a simple and practical way in obtaining the nuclear deformation parameters of L-pole (β_L) from inelastic scattering on the deformed target, and the extracted values of β_L are considered to be insensitive to the reaction mechanism or the choice of projectile causing the scattering.

However, projectile dependent systematic deviation in the deformation parameters can be seen by careful analysis of the data.[1] For the lowest 2^+ and 3^- excitations by (p, p'), (d, d'), and (α, α') scatterings on Mo isotopes, deformation parameters determined by the macroscopic model exhibit projectile dependent behavior, aside from the complicated isotope dependent differences (Table 1). It can be pointed out that in general (p, p') scattering tends to give larger values than those of (d, d') and (α, α') scatterings. Different spin or isospin structure of the projectile may be expected, in principle, to cause the above-mentioned systematic deviation. A preliminary calculation indicates, however, that this effect seems to be too small to explain the required order of magnitude.[1]

Table 1. Deformation parameters (β_L) determined by generalized optical model.

	$J^\pi(E_x \text{ MeV})$	(p, p') 12.5 MeV[3]	(d, d') 21.5 MeV[1]	(α, α') 30.87 MeV[4]
^{92}Mo	2^+(1.150)	0.080	0.083	0.078
	3^-(2.850)	0.170	0.124	0.113
^{94}Mo	2^+(0.871)	0.154	0.155	0.125
	3^-(2.533)	0.198	0.148	0.130
^{96}Mo	2^+(0.777)	0.163	0.165	0.143
	3^-(2.230)	0.179	0.153	0.138
^{98}Mo	2^+(0.788)	0.193	0.153	0.145
	3^-(2.024)	0.239	0.176	0.160
^{100}Mo	2^+(0.534)	0.259	0.224	0.187
	3^-(1.910)	0.215	0.158	0.139

In this report we propose an alternative explanation of the descrepancy by the finite size effect of the projectile, by employing Watanabe model of elastic scattering[2] as the theoretical basis and applying it to inelastic scattering. In Watanabe model, optical potential of composite particle is constructed from a phenomenological nucleon-nucleus optical potential by the folding procedure. We also assume that the inelastic scattering form factor of the composite particle projectile is constructed from the phenomenological macroscopic form factor of proton. This model may be verified under the following conditions.

(1) Composite particle is rigid enough to neglect the break-up effect during the scattering. This condition seems to hold well for α-particles but not for deuteron.
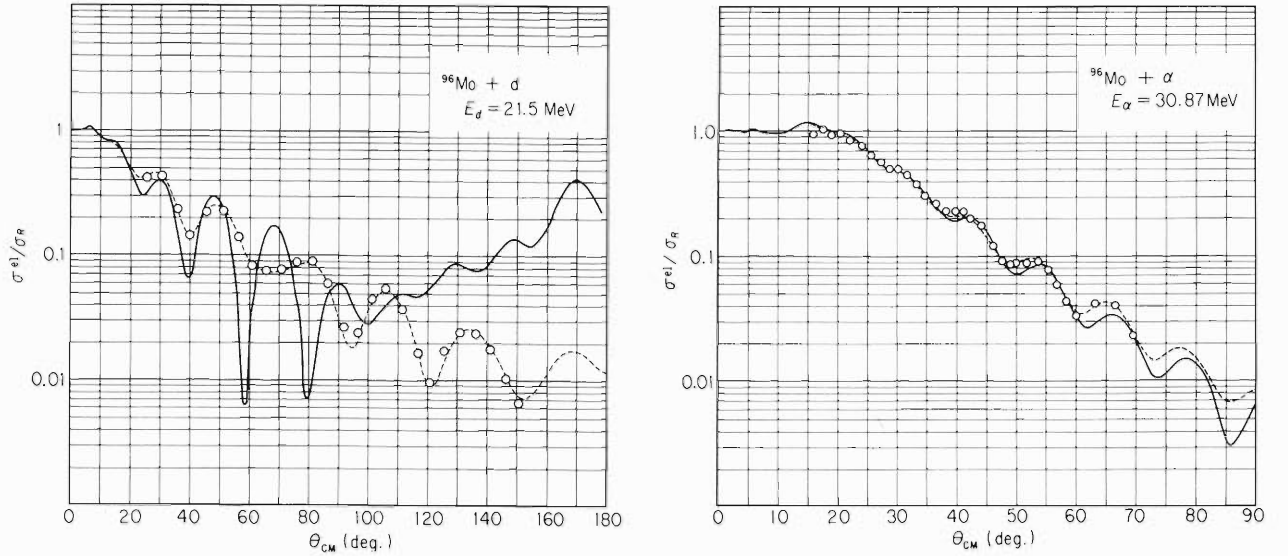
Fig. 1. Elastic scattering cross sections for ^{96}Mo + d, E_d=21.5 MeV and ^{96}Mo + α, E_α=30.87 MeV. the solid lines represent the predictions from Watanabe model and the broken lines represent the results of the best fit parameter sets of optical model analysis.

Table 2. Nucleon Optical parameters used for Watanabe model.

(1) Central depths of proton and neutron potentials

$$V_p = V_0 - 0.32 \times E + 24 \times \frac{(N - Z)}{A} + 0.4 \times Z/A^{1/3}.$$

$$V_n = V_0 - 0.32 \times E - 24 \times \frac{(N - Z)}{A}.$$

(2) ^{96}Mo + p (12.5 MeV)

$V_p = 52.504$, $W_v = 6.850$, $V_{SO} = 7.5$ (MeV)

$r_0 = r_v = 1.2769$, $a_0 = a_v = 0.5361$, $r_{SO} = 1.25$, $a_{SO} = 0.47$, $r_c = 1.25$ (fm)

(2) Contributions from two or more nucleon exchange between projectile and target are smaller than that from one nucleon exchange. This may be true for inelastic scattering because of reduction of the nuclear overlap function for exchange processes. It should be noted that one nucleon exchange effect is considered to be taken into account effectively by using the phenomenological proton optical potential.

The basic optical parameters for ^{96}Mo-p scattering ($E_p = 12.5$ MeV) are shown in Table 2. For simplicity, the same radius and diffuseness parameters are assumed for real and imaginary potentials. Figure 1 shows the results obtained from Watanabe model for elastic scatterings of ^{96}Mo-d ($E_d = 21.5$ MeV) and ^{96}Mo-α ($E_\alpha = 30.8$ MeV). Satisfactory result is obtained for α-scattering but rather poor fit for d-scattering. Deuteron break-up effect is known to be very important to reproduce the elastic scattering.[3] Thus, the analysis of inelastic scattering by our model is performed only for (α, α') case. Figure 2 shows the results for ^{96}Mo(α, α')^{96}Mo(2^+, 0.777 MeV and 3^-, 2.230 MeV) and Table 3 shows the deformation parameters determined from the usual generalized optical model and the present folding model. For 2^+ case, the above-mentioned discrepancy of β_2 values between p and α-scatterings disappears in our folding model, which indicates that the finite size effect of the projectile causes the projectile dependent
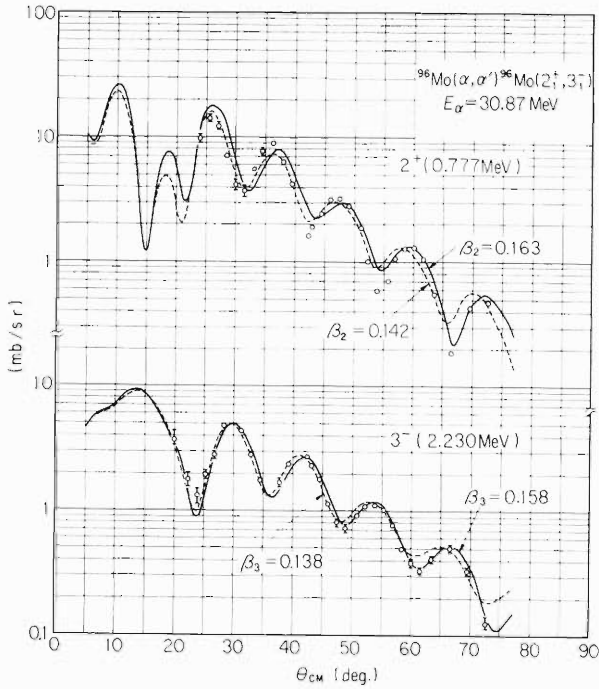
Fig. 2. Inelastic scattering cross section. The calculated cross sections are plotted by adjusting the values of deformation parameters, which are shown in the figure.

Table 3. Comparison of the deformation parameters determined by the extended Watanabe model with those by the generalized optical model.

| ^{96}Mo | (p, p') | (α, α'), 30.87 MeV | |
	12.5 MeV	Generalized optical model	Extended Watanabe model
2^+	0.163	0.143 $\beta(\alpha)/\beta(p) = 0.87$	0.163 $\beta(\alpha)/\beta(p) = 1.0$
3^-	0.179	0.138 $\beta(\alpha)/\beta(p) = 0.77$	0.158 $\beta(\alpha)/\beta(p) = 0.88$

deviation of β_L-values determined from the generalized optical model. For 3^- case, however, unfortunately only half of the discrepancy is explained by our model. To confirm the appropriateness of the idea presented here, further investigation is necessary, which includes the analysis taking the break-up effect of deuteron into account.[5]

References

1) T. Wada, H. Kamitsubo, T. Fujisawa, M. Koike, T. Nojiri, S. Yamaji, S. Kusuno, and T. Matsuura: IPCR Cyclotron Progr. Rep., 10, 54 (1976).

2) S. Watanabe: Nucl. Phys., 8, 484 (1958).

3) S. J. Burger and G. Heymann: ibid., A243, 461 (1975).

4) K. Matsuda, Y. Awaya, N. Nakanishi, and S. Takeda: J. Phys. Soc. Japan, 33, 298 (1973).

5) R. C. Johnson and P. J. R. Soper: Phys. Rev., C1, 976 (1970).

4-11. DWBA Analysis of Four-Nucleon Transfer Reaction
^{208}Pb(^{16}O, ^{12}C)^{212}Po

T. Matsuura

It has been reported[1] that the four-nucleon transfer reaction ^{208}Pb(^{16}O, ^{12}C)^{212}Po at E_{lab} = 93 MeV shows typical bell-shaped angular distributions around θ_{cm} = 85° for both $0^+_{g.s.}$ and 2^+_1(0.727 MeV) transitions, the peak values being about 750 and 1750 nb/sr, respectively. It has also been reported that the relative ratio of the spectroscopic factors extracted from an exact-finite-range DWBA analysis is $S(2^+_1)/S(0^+_{g.s.})$ = 0.64, which shows reasonable agreement with the ratio of α-decay reduced widths, $\theta^2(2^+_1)/\theta^2(0^+_{g.s.})$ = 0.61 ± 0.24.

It is known, however, that the magnitude of α-cluster transfer DWBA cross section of (^{16}O, ^{12}C) reaction is too small to reproduce the experimental cross section.[2] Here, we performed an exact-finite-range DWBA analysis, by using various kinds of α-reduced width amplitudes (form factors) for ^{212}Po = ^{208}Pb + α system, in order to see how the calculated cross
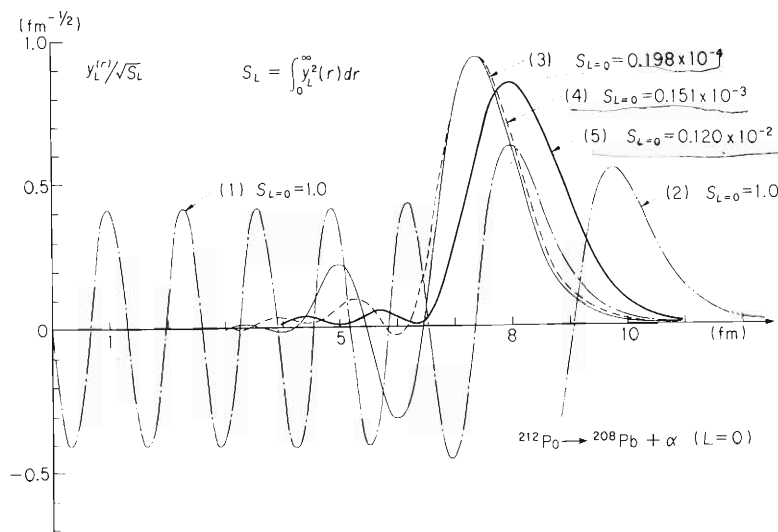
Fig. 1. Normalized reduced width amplitudes for ^{212}Po → ^{208}Pb+α(L=0).

(1) 11S state of Woods-Saxon potential
     (R=1.25×$208^{1/3}$=7.41fm, a=0.65fm, B.E.=0.1 MeV).

(2) The same as Ref. 1 except for R=1.25×($208^{1/3}$+$4^{1/3}$)= 9.39fm.

(3) Single configuration $(0h_{9/2})^2$ (0)$(1g_{9/2})^2$ (0).

(4) Glendenning and Harada.

(5) Tonozuka (89 orbits for protons and 83 orbits for neutrons). Spectroscopic factors (S_L) are shown in the figure.

section changes its magnitude by the different choice of form factors. The same parameters as those in Ref. 1 are used for optical potentials and the wave function of $^{16}O = {}^{12}C + \alpha$ system. Following form factors are examined for $^{212}Po = {}^{208}Pb + \alpha$ system.

    1) $11S(0^+)$ and $10D(2^+)$ states of the phenomenological Woods-Saxon potential $(R = 1.25 \times 208^{1/3}$ fm, $a = 0.65$ fm).

    2) $11S(0^+)$ and $10D(2^+)$ states of the phenomenological Woods-Saxon potential $(R = 1.25 \times (208^{1/3} + 4^{1/3})$ fm, $a = 0.65$ fm).

    3)   Form factors constructed from harmonic oscillator shell model wave function of $h_{9/2}^2(0)g_{9/2}^2(0)$ single configuration.

    4)   Form factors constructed from Glendenning and Harada's wave function.[3]

    5)   Form factors constructed from Tonozuka's wave function of large space configuration mixing (89 orbits for protons and 83 orbits for neutrons are promoted).[4]

In the cases of 3) − 5), asymptotic part of the wave functions are replaced by the solution of Woods-Saxon potential. Bound state approximation is used in the case of 1) and 2), by giving tentative binding energy of 0.1 MeV.

    1.   Form factor dependence

Form factor dependence of the DWBA cross section is shown in Table 1. In all cases, the angular distribution is nicely reproduced, but the magnitude changes so much by the radius of form factor. $(S(^{16}O; {}^{12}C) = 1.0$ is assumed and form factors are normalized to unity).

    2.   Absolute value of the cross section

Assuming $S(^{16}O; {}^{12}C) = (0.54)^2$ (the result of LS coupling shell model), comparison with experimental cross section is made in the cases of 3) − 5) (Table 2, with the result for α-decay). The remarkable enhancement of about 10^5 by the configuration mixing is seen, partly due to the expansion of the range of form factor and partly due to the enhancement of the spectroscopic factor, $S(^{212}Po; {}^{208}Pb)$. It should be noted, however, that even in the case of 5) (large configuration mixing) still multiplicative factor of $\times 24$ ($\times 50$) is necessary to reproduce the α-transfer (α-decay) experiment.

    3.   Relative ratio of the spectroscopic factors

The relative ratio of the spectroscopic factors, $S(2^+)/S(0^+)$, is rather insensitive to the choice of form factor, namely, 0.64, 0.57, and 0.52 for the cases 1), 2), and 4), respectively.

Table 1. The peak values of the DWBA cross sections are shown. All of the form factors are normalized to unity.

Form factor	σDW (peak) (mb/sr)	Relative ratio
1)	0.588×10^{-2} (82.5°)	1
2)	0.122×10^{1} (86°)	207
3)	0.128×10^{-2} (82.5°)	0.218
4)	0.170×10^{-2} (82.5°)	0.289
5)	0.432×10^{-1} (85°)	7.35

Table 2. Theoretical spectroscopic factors and the comparison of the
α-transfer cross sections and the α-decay reduced width with the
experiments. $S(^{16}O; ^{12}C) = (0.54)^2$ is assumed for the transfer case.

Form factor	$S(^{212}Po; ^{208}Pb)$	$\theta^2_{cal}/\theta^2_{exp}$	$\sigma_{cal}/\sigma_{exp}$
3)	1.98×10^{-5}	6.7×10^{-6}	9.88×10^{-6}
4)	1.51×10^{-4}	1.02×10^{-4}	9.95×10^{-5}
5)	1.20×10^{-3}	4.2×10^{-2}	2.01×10^{-2}

In this analysis, we have confirmed that the absolute value of the cluster-transfer DWBA cross section is still too small to reproduce the experiment even in the case of large configuration mixing, though the angular distribution and the relative ratio of spectroscopic factors are well explained.
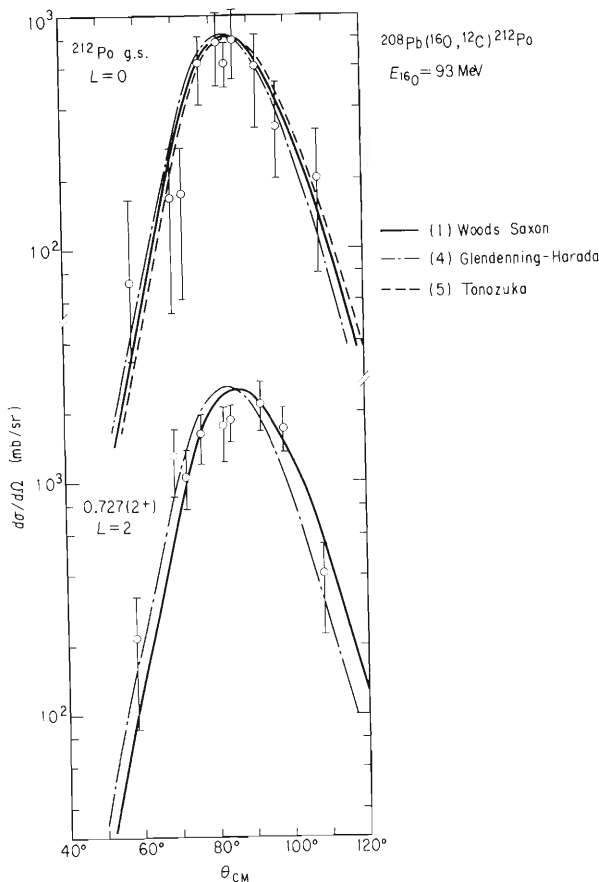
Fig. 2. DWBA cross sections with different form factors are shown. Calculated cross sections are normalized to the experimental data. See the Table 1 and 2 for the normalization factors.

References

1) R. M. Devries, D. Shapira, W. G. Davies, G. C. Ball, J. S. Forster, and W. McLatchie: Phys. Rev. Lett., 35, 835 (1975).

2) K. I. Kubo: Proc. INS-IPCR Symp. on Cluster Structure of Nuclei and Transfer Reactions Induced by Heavy-Ions, March, p.532 (1975).

3) N. K. Glendenning and K. Harada: Nucl. Phys., 72, 481 (1965).

4) I. Tonozuka: Plivate communication (Ph. D. Thesis, Department of Physics, Univ. of Tokyo (1975)).

4-12. Effects of Recoil and Sequential Transfer in $^{12}C(^{14}N,^{12}C)^{14}N$ Reaction at 79 MeV Incident Energy

T. Kammuri, T. Motobayashi, I. Kohno, K. Katori,
M. Yoshie,* T. Ooi, and H. Kamitsubo

With inclusion of the recoil effect in the DWBA treatment of the transfer reaction, additional angular momentum transfers are often intorduced, which can change the angular distribution drastically. A typical example is the one-proton transfer reaction $^{12}C(^{14}N,^{13}C)^{13}N$.[1] While no-recoil DWBA predicts strong oscillation, the full-recoil angular distribution decreases rather monotonously with angle. Here we study similar effect of recoil on the two-nucleon transfer reaction $^{12}C(^{14}N, ^{12}C)^{14}N$ at the incident energy of 79 MeV.[2] We also aim to study the competition of simultaneous and successive transfers of a neutron-proton pair.

In the sum-of-interaction formulation of the two-nucleon transfer reaction,[3] one-step DWBA amplitude is characterized by the set of transferred quantum numbers (ℓ_1, ℓ_2, ℓ). Taking post form for the interaction, ℓ_1 and ℓ_2 are related to the non-orthogonality overlap and the
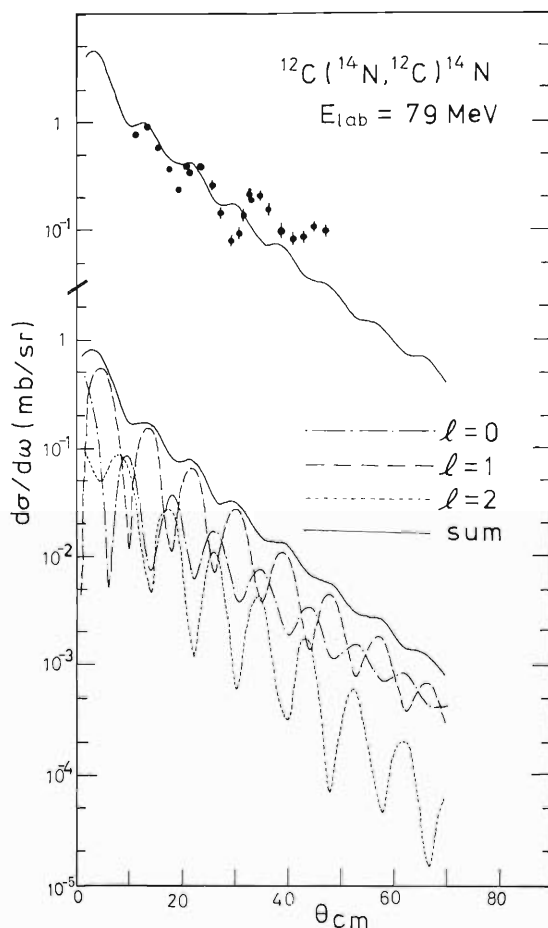
Fig. 1. Experimental and full-recoil two-step DWBA angular distributions for the $^{12}C(^{14}N,^{12}C)^{14}N$ reaction at 79 MeV incident energy. Lower part of the figure shows the calculated cross sections for the orbital angular momentum transfer $\ell = 0$ (dot-dashed), $\ell = 1$ (dashed), $\ell = 2$ (dotted) and their incoherent sum (solid curve). In the upper part, the sum is normalized and compared to the experimental data. The multiplicative factor is 5.0.

interaction matrix element respectively, and ℓ is the vector sum of ℓ_1 and ℓ_2. The same set (ℓ_1, ℓ_2, ℓ) specifies two-step amplitude, where ℓ_1 or ℓ_2 means the orbital angular momentum transfer at each step. For the case of $^{12}C(^{14}N, ^{12}C)^{14}N$ reaction with transfer of $0p_{1/2}$ nucleons, we have $\ell_i = 0$ and 1. No-recoil DWBA calculations restrict ℓ_i and ℓ to be zero, and give rapidly oscillating angular distributions as shown in Fig. 1. Full-recoil treatment allows $\ell = 1$ and 2 transfers of the same order of magnitudes as $\ell = 0$ component. The $\ell = 1$ component oscillates out of phase with even ℓ parts, so that summed cross section shows smoothly decreasing behavior.

DWBA calculations were performed by using the program code FRATS,[4] with optical parameters listed as set A in Table 1.[5] Angular shapes of one- and two-step processes are very much the same, so we have shown only the two-step post-post results in Fig. 1. The normalization factor N_{ff} is 5.0. If we use the set B which also gives good fit to the elastic scattering of ^{14}N on ^{12}C, N_{ff} becomes 25. The ratios of two-step post-post and one-step post cross sections are 1.5, 2.1, and 2.4 for $\ell = 0$, 1, and 2 respectively. Although sequential transfer has bigger cross section than simultaneous transfer process, the difference between two processes is much smaller as compared with the case of transfer of idential-nucleon pair treated in Ref. 3.

Table 1. Optical parameters for the $^{12}C(^{14}N, ^{12}C)^{14}N$ reaction.

Set	V (MeV)	r_R (fm)	a_R (fm)	W (MeV)	r_I (fm)	a_I (fm)
A	100	0.92	0.77	38.5	1.29	0.26
B	65	1.21	0.48	20	1.35	0.25

References

1) R. M. DeVries and K. I. Kubo: Phys. Rev. Lett., 30, 325 (1973);
   R. M. DeVries: Phys. Rev., C8, 951 (1973).

2) T. Motobayashi, I. Kohno, S. Nakajima, M. Yoshie, K. Katori, T. Mikumo, and H. Kamitsubo: Proc. Intern. Symp. on Cluster Structure of Nuclei and Transfer Reactions Induced by Heavy Ions, Tokyo (1975); edited by H. Kamitsubo, I. Kohno, and T. Marumori (IPCR cyclotron Progr. Report Suppl. 4, p. 725 (1975). unpublished).

3) T. Kammuri: Nucl. Phys., A259, 343 (1976).

4) T. Kammuri and S. Yamaji: DWBA code FRATS (unpublished).

5) W. von Oertzen, M. Liu, C. Caverzasio, J. C. Jacmart, F. Pougheon, M. Rion, J. C. Roynette, and C. Stephan: Nucl. Phys., A143, 34 (1970).

4-13. Collective Mass Transfer in the Collision ^{238}U - ^{238}U

S. Yamaji, W. Scheid,* H. J. Fink,* and W. Greiner*

In order to study the mass fragmentation in fission and heavy-ion scattering, it is useful to introduce a collective fragmentation coordinate defined by [1]

$$\eta = (A_1 - A_2) / (A_1 + A_2) \tag{1}$$

The mass distribution of fissioning nuclei has been explained by a dynamical treatment of the collective coordinate η.[2] The idea of quantized fragmentation dynamics can also be applied straight-forwardly to the fragmentation in heavy ion reactions.[3],[4]

Calculations of the mass fragmentation in U-U collisions [4] gave an estimate of the order of the fragmentation time. This paper is devoted to the question about the possibility of producing superheavy elements in the U-U collision. The idea is to describe the collision of the two nuclei by the relative coordinate R and the fragmentation coordinate η defined in Eqn. (1)

The collective energy of the system is of the following from

$$H(\vec{R}, \dot{\eta}, \vec{R}, \eta) = \frac{1}{2} B_{RR}(R,\eta)\dot{\vec{R}}^2 + \vec{B}_{R\eta}(R,\eta)\dot{\vec{R}}\dot{\eta} + \frac{1}{2} B_{\eta\eta}(R,\eta)\dot{\eta}^2 + V(R,\eta). \tag{2}$$

The potential and the mass parameters are consistently calculated within the renormalization method and the cranking model on the basis of the asymmetric two center shell model.[5] The fragmentation potential $V(R,\eta)$ for ^{238}U$-^{238}$U is shown in Fig. 1.

The η-motion in Eqn. (2) is quantized according to the Pauli prescription. Then the mass fragmentation is the solution of the time-dependent Schrödinger equation

$$H\psi(\eta, t) = i\hbar \frac{\partial}{\partial t} \psi(\eta, t)$$

$$H = -\frac{\hbar^2}{2\sqrt{B_{\eta\eta}(R(t), \eta)}} \frac{\partial}{\partial\eta} \frac{1}{\sqrt{B_{\eta\eta}(R(t), \eta)}} \frac{\partial}{\partial\eta} + \frac{P_R(t)^2}{2B_{RR}(R(t), \eta)}$$

$$+ \frac{L^2}{2B_{RR}(R(t), \eta)R(t)^2} + V(R(t), \eta) \tag{3}$$

, where the relative coordinate R(t) and its conjugate $P_R(t)$ are obtained by solving Hamilton's coupled equations of Eqn. (2). In order to simplify the calculations, the coupling term in Eqn. (2) is neglected because of $|\vec{B}_{R\eta}| << \sqrt{B_{RR}B_{\eta\eta}}$ as proven in Ref. 5.

* Institut für Theoretische Physik der Universität Frankfurt/M., Germany.

Equation (3) is solved directly by the finite difference method.[6] The fragmentation probability at time t and fragmentation η is $dW(\eta,t) = |\psi(\eta,t)|^2 \sqrt{B_{\eta\eta}\ (R(t),\eta)}d\eta$.

The initial conditions are chosen in the following way: We assume that dynamical effects are not important for separations $R > R_c$ where R_c is the distance of critical overlap. Therefore, we make an *ansatz* for the initial mass distribution at

$$R = R_c \ (t = 0): \quad \psi(\eta, t = 0) = \exp\left\{-\frac{1}{2}\left(\frac{\eta - \eta_i}{\Gamma}\right)^2\right\} \Bigg/ \sqrt{\int_{-1}^{1} \exp\left\{-\left(\frac{\eta - \eta_i}{\Gamma}\right)^2\right\} \sqrt{B_{\eta\eta}\ (R_c, \eta)}\ d\eta} \ .$$

Here, the coordinate η_i of the initial mass fragmentation characterizes projectile and target, and the width Γ the few nucleon transfer which can occur before the critical distance R_c is reached. The critical distance, $R_c = 14.5$ fm, is assumed to be equal to the touching distance of the two nuclei. Therefore, the collective mass transfer starts for $R = R_c$ at the time $t = 0$ when the two
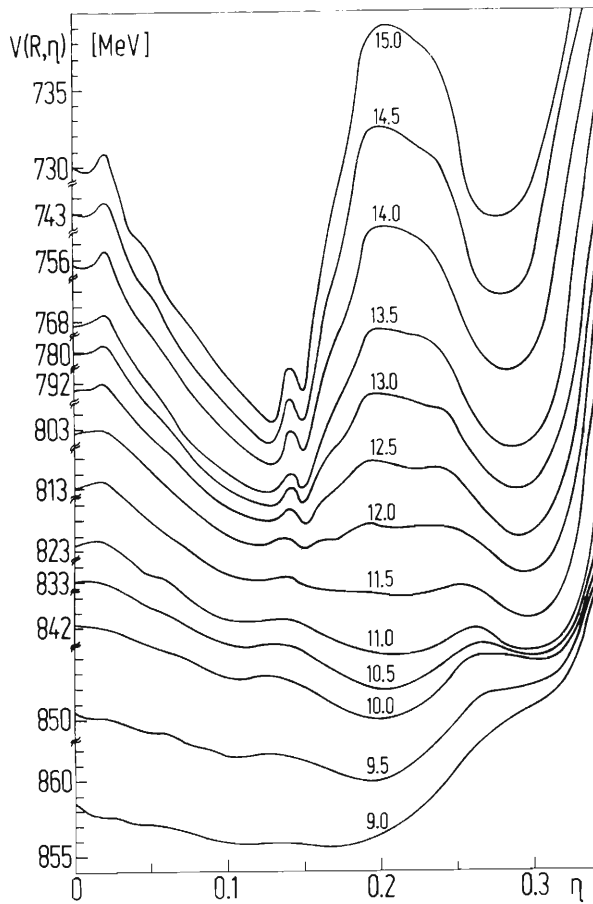
Fig. 1. The fragmentation potential $V(R,\eta)$ between the relative distances 9.0 fm and 15.0 fm calculated by the fourth order Lagrangian interpolation technique from the values of Ref. 5. The numbers at the curves show the values of the relative distance in units of fm.
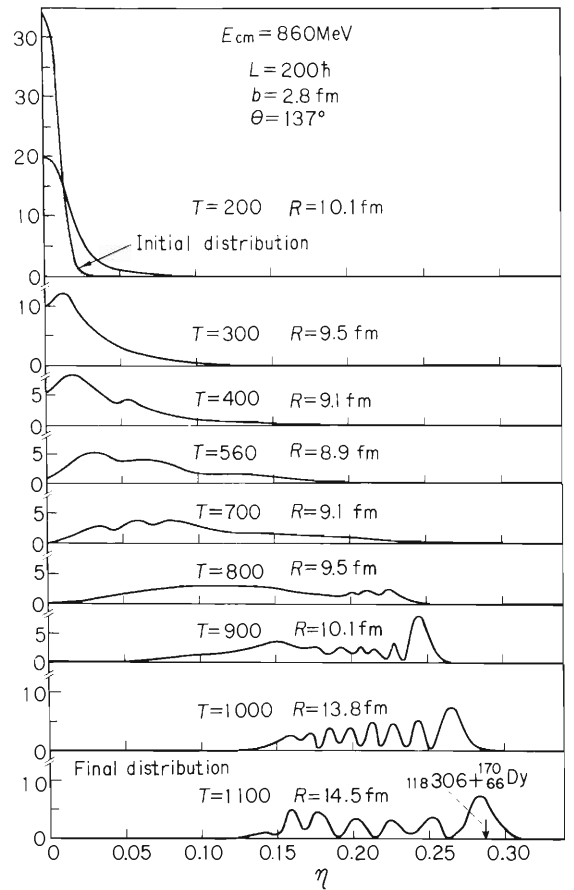
Fig. 2. The time-evolution of the mass distributions for the incident energy 860 MeV is shown. The numbers at the curves are the time in units of 10^{-23} sec.

colliding nuclei touch and continues until the two fragments separate at $R = R_c$ again.

An example of the time evolution of the mass fragmentation is presented for the incident energy E_{cm} = 860 MeV and the angular momentum L = 200 ħ in Fig.2. The width is chosen Γ = 0.0126 which corresponds to a spread in mass A of $\triangle A$ = 3.

The mass distribution spreads out up to 200×10^{-23} sec., when the colliding nuclei come close to 10.2 fm. As the small barrier at η = 0.02 in Fig. 1 disappears at 10.2 fm, the motion of fragmentation starts. However, in the region 9 ~ 10 fm and η = 0.02 ~ 0.2, the fragmentation moves very slowly due to the small driving force $- \partial V/\partial \eta$. The appreciable part of the distribution has already reached η = 0.25 at time $T = 900 \times 10^{-23}$ sec.

Such large η-values correspond to superheavy nuclei with A ~ 300. In spite of the large potential barrier at η = 0.2 for $R \approx R_c$ (see Fig. 1) larger mass transfer is possible with increasing incident energy, since smaller relative distances are reached. The present calculations give evidence for the possibility of producing superheavy nuclei in the U-U-collision.

The estimated cross sections are of the order $\sigma(\text{superheavy}) = \int_0^{b_{max}} 2\pi b \ W_b(\eta) db \triangle \eta \approx 1b$, where

$W_b(\eta) \triangle \eta$ is the probability producing superheavy nuclei (A~300) in the collision with the impact parameter b.

References

1)   P. Lichtner, D. Drechsel, J. Maruhn, and W. Greiner: Phys. Lett., 45B, 175 (1973).

2)   J. Maruhn and W. Greiner: Phys. Rev., C13, 2404 (1976).

3)   H. J. Fink, J. Maruhn, W. Scheid, and W. Greiner: Z. Physik, 268, 321 (1974).

4)   S. Yamaji, W. Scheid, H. J. Fink, and W. Greiner: ibid., A278, 69 (1976).

5)   O. Zohni, J. Maruhn, W. Scheid, and W. Greiner: ibid., A275, 234 (1975).

6)   A. Goldberg, H. M. Schey, and J. L. Schwarz: Am. J. Phys., 35(3), 177 (1967).

4-14. Elastic and Inelastic Scatterings of Deuteron from Even-Mass Isotopes of Molybdenum

T. Wada, H. Kamitsubo, T. Fujisawa, M. Koike,
T. Nojiri,* S. Yamaji, S. Kusuno,** and T. Matsuura

The experimental results have been reported.[1] The elastic scatterings were analyzed by an optical model. In the range of real potential well depths between 50 and 180 MeV, three sets of optical parameters were found to give equivalent fits to the experimental data. The parameter set with $V_R \sim 100$ MeV was found best to fit the experimental data of the inelastic scattering. The inelastic scatterings were analyzed by coupled-channel calculations using an automatic parameter search code CCSEARCH.[2] The deduced values of the deformation parameters were compared with those from other experiments with different projectiles. The inelastic scatterings from the isotopes of molybdenum have been studied with protons,[3]-[5] deuterons,[6] and alpha particles.[5],[7],[8] Although the deformation parameter is usually assumed to be an intrinsic property of the nucleus and is independent of the means of excitation, systematic differences in the values of the deformation parameters for the one-phonon states were found between the results from the inelastic scatterings with different projectiles. Figure 1 shows how different these results are one another. Although it is well known that instead of the deformation parameter β the deformation length βR must be used for comparison, there is an ambiguity in determination of R in case of complex potential. Then we compared
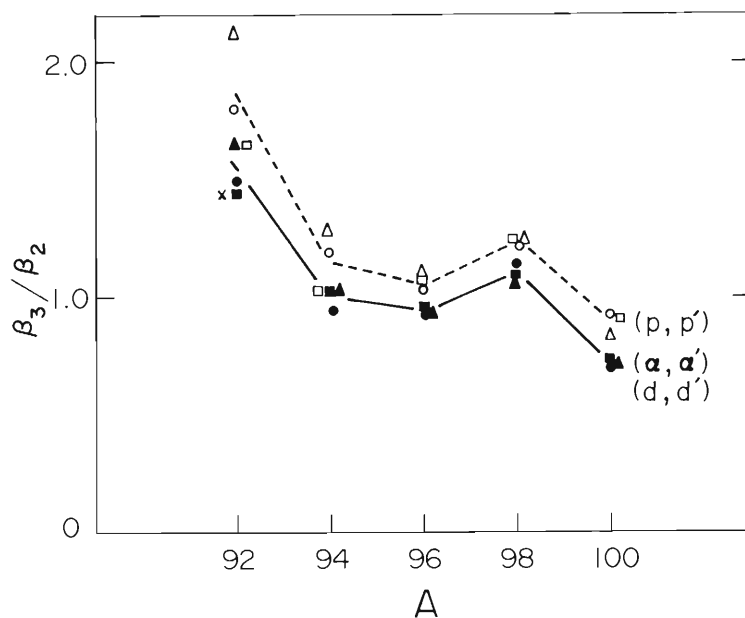
Fig. 1. Comparison of the ratio of β_3 to β_2 from different projectiles:
○ for (p,p') at 15 MeV, Ref. 3.
△ for (p,p') at 14.5 MeV, Ref. 4.
□ for (p,p') at 12.5 MeV, Ref. 5.
X for (α,α') at 31 MeV, Ref. 7.
■ for (α,α') at 30.87 MeV, Ref. 8.
▲ for (α,α') at 32.2 MeV, Ref. 5.
● for (d,d') at 21.5 MeV, present work.
The solid curve presents the average values of the results from (d,d') and (α,α'), and the dashed curve the average values of the results from (p,p').

* Osaka University.
** NAIG Nuclear Research Laboratory.

the ratio of the deformation parameters. For all the five isotopes, the ratios of β_3 to β_2 from (d, d') agree quite well with those from (α, α'), while they are smaller by about $10 \approx 20$ per cent than those from (p, p').

In order to investigate the isotopic spin dependence of the excitation, the form factors are calculated by a RPA theory where they are separated for pure isoscalar and isovector terms. The isotopic spin dependence was found to be too small to explain the differences shown in Fig. 1.

It has been shown that the deformation parameter of higher order is affected more strongly if a finite size of a projectile is taken into account.[9] We performed a folding model calculation in which the optical potential and the form factor of nucleon were folded over the internal wave function of projectile. The inelastic scattering cross section from the first 3^- state was reduced by about 30 per cent, while that from the first 2^+ state was not affected greatly. The β_3 must then be increased by about 15 per cent. This amount is similar to the difference shown in Fig. 1. For the scattering of alpha particles, the folding model gives similar results as shown in 4-10.

References

1) T. Wada, H. Kamitsubo, T. Fujisawa, M. Koike, and T. Inanaga: IPCR Cyclotron Progr. Rep., 6, 33 (1972).

2) T. Wada and S. Yamaji: Sci. Papers I. P. C. R., 68, 65 (1974).

3) H. F. Luts, D. W. Heikkinen, and W. Bartulini: Phys. Rev., C4, 934 (1971).

4) Y. Awaya, M. Matsuda, T. Wada, N. Nakanishi, S. Takeda, and S. Yamaji: J. Phys. Soc. Japan, 33, 881 (1972).

5) S. J. Burger and G. Heymann: Nucl. Phys., A243, 461 (1975).

6) Y. S. Kim and B. L. Cohen: Phys. Rev., 142, 788 (1966).

7) E. J. Martens and A. M. Bernstein: Nucl. Phys., A117, 241 (1968).

8) K. Matsuda, Y. Awaya, N. Nakanishi, and S. Takeda: J. Phys. Soc. Japan, 33, 298 (1972).

9) D. L. Hendrie: Phys. Rev. Lett., 31, 478 (1973).

4-15. Polarization Measurement of $^{12}B_{g.s.}$ Produced in ^{14}N-Induced Reaction

K. Tanaka, M. Ishihara, H. Kamitsubo, N. Takahashi,
Y. Nojiri, T. Minamisono,* A. Mizobuchi,* and K. Sugimoto*

It is known that there exist two processes called "deep inelastic collision" and "quasi-elastic scattering" in heavy ion induced reactions.[1] A recent description[2] of such processes, in which frictional forces play an important role, points out a possibility of a negative angle scattering being supposedly responsible for deep inelastic processes and a positive angle scattering for quasi-elastic processes. According to such an interpretation, the spin polarization of the reaction products presents an important parameter.

Hence we have started the polarization measurement for $^{12}B_{g.s.}$ produced in the ^{14}N-induced reaction, by measuring up-and-down asymmetry of β-ray yields with respect to the scattering plane. A 15.3mg/cm² thick natural molybdenum target and ^{14}N-beam of E=95 MeV were used. A well established adiabatic fast passage NMR technique[3] was employed to eliminate spurious asymmetry effects caused by geometrical asymmetries. The beam from the cyclotron was chopped by a mechanical chopper.[4]

The procedure during one beam cycle was as follows: During on-beam period of 40 msec,
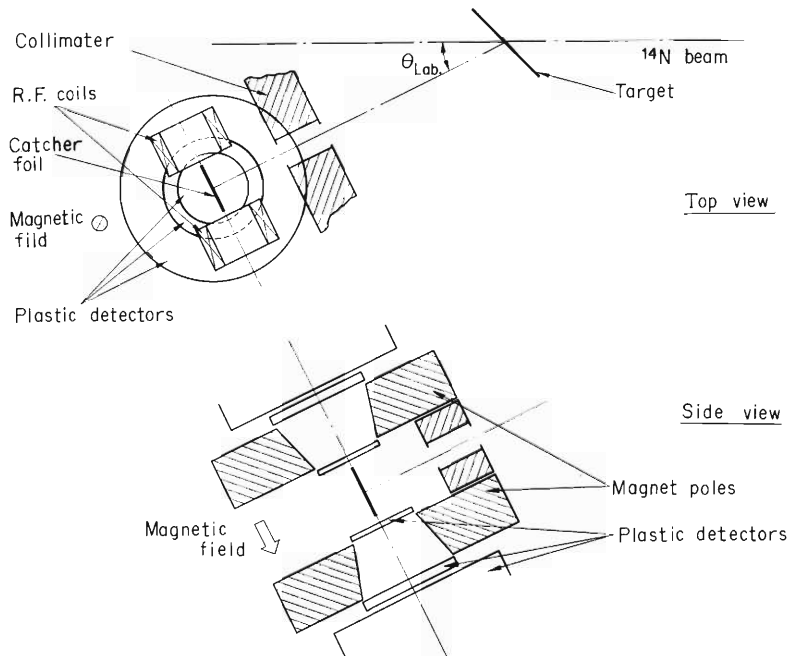
Fig. 1. Schematic drawing of the experimental arrangement.

^{12}B products were implanted into a platinum catcher foil. The initial polarization was preserved by a static field of 1.5 kG which had been found to be sufficient. During the following off-beam period of 40 msec a R.F. field perpendicular to the static field was applied for a few msec, and then β-rays from the catcher were detected by a pair of three-fold plastic detectors placed at the upper and lower side of the catcher. (Fig. 1)

In the measurement two kinds of the beam cycles were alternated with each other: One was so-called "on-resonance" cycle in which the frequency of the R.F. field was swept across a resonant point so that the polarization of ^{12}B was reversed, and the other was "off-resonance" cycle in which the frequency was swept over the region beyond a resonant point with the polarization unchanged. β-ray events Y_U, Y_L in upper and lower side of the catcher were accumulated for each kind of beam cycles. Supposing the polarization P produced in the reaction points downwards, the yields for "off-resonance" cycles can be written as

$$Y_U^{OFF} = C_U \ (1-AP),$$

$$Y_L^{OFF} = C_L \ (1+AP),$$

and those for "on-resonance" cycles as

$$Y_U^{ON} = C_U \ (1+AP),$$

$$Y_L^{ON} = C_L \ (1-AP),$$

where C_U and C_L are the geometrical factors of the upper and lower set of counters, respectively. A is the asymmetry parameter and A=-1 for ^{12}B decays. Therefore, we can derive the polarization from the ratio

$$R = \frac{Y_U^{OFF} \ / \ Y_L^{OFF}}{Y_U^{ON} \ / \ Y_L^{ON}} = \left(\frac{1 + P}{1 - P} \right)^2$$
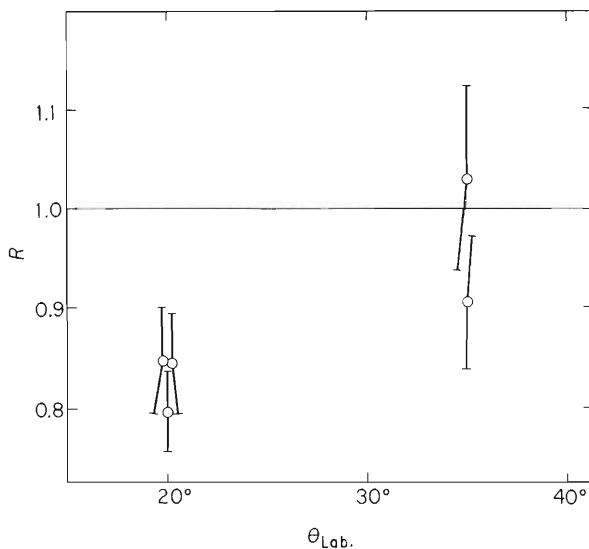
Fig. 2. Ratio R for each run. After a rough correction for depolarization effects, the polarization for $\theta_{Lab}=20°$ is derived from these values as P = $-$ 6.1 ± 1.1%. Only statistical errors are taken into account.

Figure 2 shows the present result, which gives a rather small polarization:

$$P = -6.1 \pm 1.1\%.$$

To examine these values, next experiment is now under consideration:
An enriched target is used; and the kinetic energy of the ^{12}B product is changed at small steps by choosing suitable thicknesses of the catcher foil and of the absorber inserted between the target and the catcher.

References

1) A. G. Artukh, C. F. Gridnev, V. L. Mikheev, V. V. Volkov, and J. Wilczynski: Nucl. Phys., A215, 91 (1973).

2) J. Wilczynski: Phys. Lett., 47B, 484 (1973).

3) K. Sugimoto, K. Nakai, K. Matsuda, and T. Minamisono: J. Phys. Soc. of Japan, 25, 1258 (1968);
M. Hori, S. Ochi, T. Minamisono, A. Mizobuchi, and K. Sugimoto: ibid., 34, Supplement, p. 161 (1973).

4) A. Hashizume and H. Kumagai: IPCR Cyclotron Progr. Rep., 5, 72 (1971).

5. NUCLER PHYSICS

Nuclear Spectroscopy

5-1. Gamma Rays from an Incomplete Fusion Reaction Induced by 95 MeV ^{14}N

T. Inamura, K. Hiruta, M. Ishihara,
T. Fukuda, and T. Shimoda

It has already been pointed out that high-energy charged particles, in particular α-particles, are emitted predominantly in the forward direction in the bombardment of various targets with heavy ions.[1],[2] Projectiles should then pass the grazing trajectory, according to Kaufman and Walfgang.[3] Because of this, by detecting those α-particles (hereafter we call them "direct" α-particles for convenience) it may be possible to select a reaction channel which leads to selective population of high spin states. To test this idea we made "direct" α-γ coincidence measurement in the bombardment of ^{159}Tb with 95 MeV ^{14}N.

The ^{159}Tb target was a self-supporting metallic foil (2.1 mg/cm^2). To detect α-particles we used a Si surface-barrier annular detector at 0° to the beam. The solid angle subtended was 0.73 sr (θ=16.7°− 32.6° to the beam). The γ-ray detector used was a 60 cm^3 Ge(Li) counter placed at 90° to the beam and 4 cm from the target. To make the contribution from the compound nucleus formation negligible, lower energy α-particles ($E_\alpha \lesssim 33$ MeV in lab) were cut off by using a 400 μm thick aluminum foil (annular as well) in front of the Si detector.

To see how different γ de-excitation after "direct" α-particle emission appears compared to compound nucleus formation, we also measured γ-rays in coincidence with α-particles emitted in the backward direction. The same annular detector was placed at 180° to the beam, the detection angle being 147.4°− 163.3°. We used a 100 μm thick alminum foil instead of the 400 μm thick one.

Figure 1(a) shows the γ-ray spectrum observed in coincidence with "direct" α-particles. Stronger γ-rays have been identified as those from ^{166}Yb. This suggests that three neutrons successively evapolate after "direct" α-particle emission, i.e. the ^{159}Tb(^{14}N,α3n)^{166}Yb reaction from incomplete fusion.

Figure 1(b) shows the γ-ray spectrum observed in coincidence with "compound" α-particles. Figure 2 shows intensities of cascade E2 transitions relative to the $4^+ \rightarrow 2^+$ transition in the de-excitation of the residual nuclei, such as ^{164}Yb, ^{166}Yb, and ^{168}Hf, in the bombardment of ^{159}Tb with 95 MeV ^{14}N. It is clearly seen that yields of the cascade transitions in ^{166}Yb produced via incomplete fusion are totally different from those in the compound-nucleus reaction products. The former indicates that there was no side-feeding and that entry states with limited spin values just above J=10 were populated, feeding the ground band only.

The solid line in Fig. 2 was obtained from the Gaussian distribution with a half-width of 2 $\hbar$ and a mean value of 13 $\hbar$. Provided the average angular momentum of the observed α-
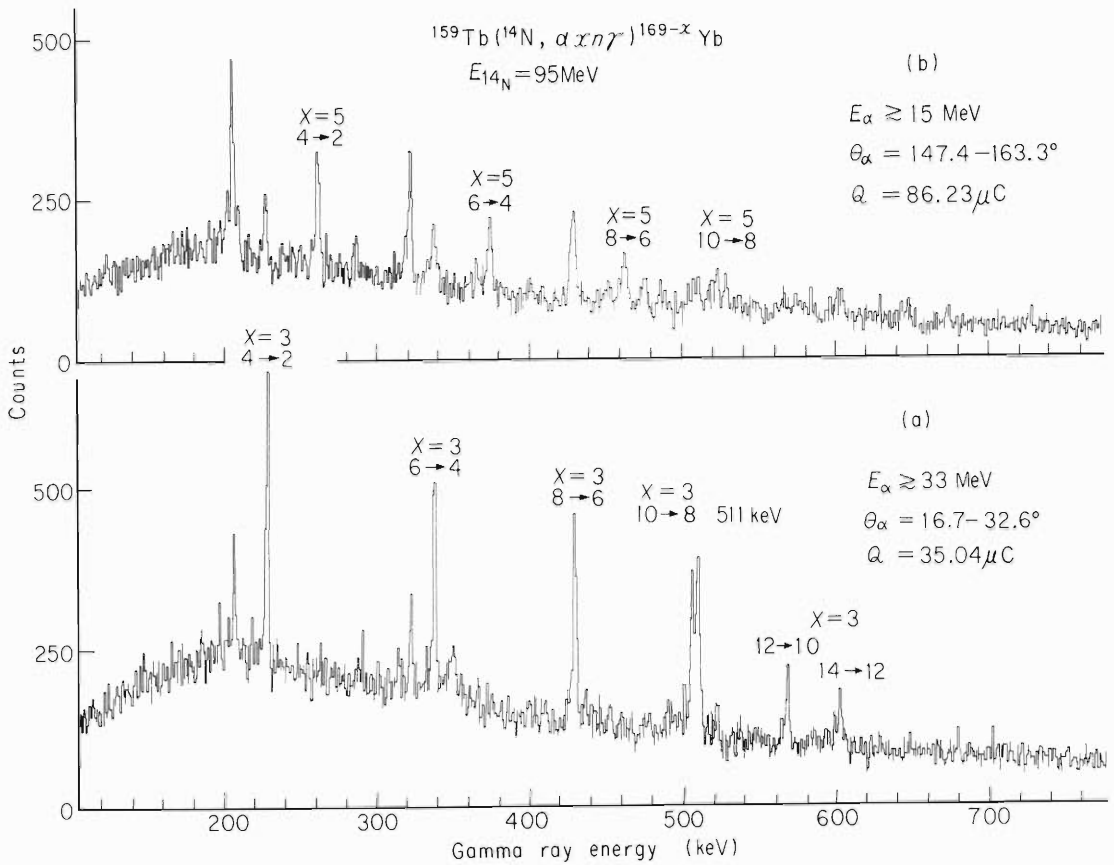
Fig. 1. γ-ray spectra observed in coincidence with a) "direct" α-particles emitted in the forward direction ($E_\alpha \gtrsim 33$ MeV) and b) "compound" α-particles emitted in the backward direction ($E_\alpha \gtrsim 15$ MeV) in the bombardment of ^{159}Tb with 95 MeV ^{14}N.
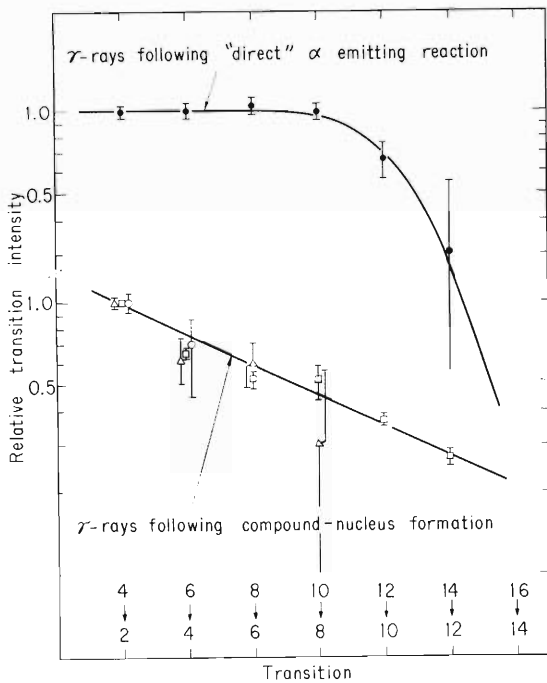
Fig. 2. γ-transition intensities relative to the $4^+ \rightarrow 2^+$ transition in de-excitation of the ^{159}Tb+95 MeV ^{14}N reaction products: ● indicates γ-rays from ^{166}Yb in coincidence with "direct" α-particles; the solid curve was obtained using a Gaussian spin distribution (half-width=2ℏ, mean=13ℏ) of states populated immediately after evaporation of three neutrons. The lower part of the drawing shows the data on γ-rays following the compound-nucleus formation: □ for $(^{14}N, 5n\gamma)^{168}$Hf, ○ for $(^{14}N, \alpha3n\gamma)^{166}$Yb, and △ for $(^{14}N, \alpha5n\gamma)^{164}$Yb; a thin line is drawn just to guide the eye.

particles ($E_\alpha \lesssim 33$MeV) is given by $\ell=21$ $\hbar$, a semi-classical value which is derived using the average kinetic energy of 40 MeV in lab, the total angular momentum removed by particle emission should be $\ell=27$ $\hbar$, on the average, because the total average angular momentum of three neutrons is estimated to be 6 $\hbar$. Then we have $\ell=40$ $\hbar$ as the mean value of the initial angular momentum. It is interesting to note that this mean value is just above the critical angular momentum $\ell_{cr}=37$ $\hbar$ in the ^{159}Tb + 95 MeV ^{14}N reaction. Perhaps the initial angular momentum distribution of the reaction channel in question is narrowly restricted to just above ℓ_{cr}.

References

1) H.C. Britt and A.R. Quinton: Phys. Rev., 124, 877 (1961).

2) J. Galin, B. Gatty, D. Guerrean, C. Rousset, U.C. Schlotthauer-Voos, and X. Tarrago: ibid., C9, 1126 (1974).

3) R. Kaufman and R. Walfgang: ibid., 121, 192 (1961).

5-2. Excited States in ^{104}Cd via the (^{3}He, 3n) Reaction

A. Hashizume, T. Katou, Y. Tendow,

and H. Kumagai

^{104}Cd was excited via the ^{104}Pd (^{3}He, 3n) reaction and excited states were investigated by measuring de-excitation γ-rays. Excitation functions, γ-γ coincidences and angular distributions were studied. Excitation functions were studied with the incident energies from 26 to 46 MeV. Typical example of excitation curves of ^{104}Pd (^{3}He, 3n)^{104}Cd taken for 658, 834, and 878 keV γ-rays were shown in Fig. 1.

In the course of this experiment, efforts were made to elucidate γ-γ coincident relations which provide very effective means to correlate many observed γ-rays and the transitions concerned in level scheme. The experimental set up of the coincidence measurement has been reported already.[1] The digitalized coincidence data in 2048 × 2048 channels were stored event by event in magnetic tapes. Digital gates were opened by playing these magnetic tapes and the coincident spectrum for each interested γ-rays was obtained. Total coincident events registered in magnetic tapes amount to about 450000 counts. Figures 2 and 3 show typical coincident spectra. In these spectra the background obtained for the same gate width in neighbourhood of the total absorption peak was subtracted and smoothing procedure of the spectrum was performed twice. From Figs. 2 and 3, it is evident that a strong coincident relation exists between 538, 878, 835, and 658 keV γ-rays; these γ-rays can be attributed to cascade transitions $(8^+) \rightarrow 6^+ \rightarrow 4^+ \rightarrow 2^+ \rightarrow 0^+$ in the order at which the photons are given
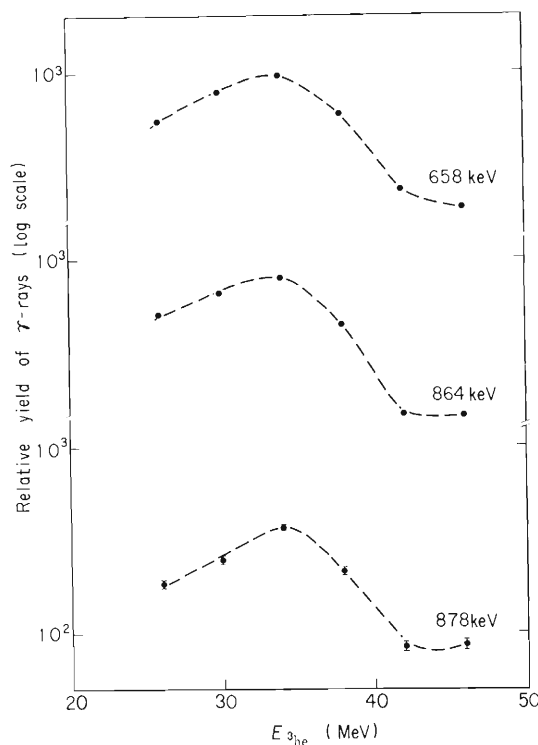
Fig. 1. Excitation functions taken by 658, 864, and 878 keV γ-rays. The dotted curves were drawn through the experimental points.

Fig. 2 and 3. γ-γ coincident spectra obtained when ^{104}Pd target was bombarded with ^{3}He of 35 MeV.

above. These results confirm the assignment of $4^+ \to 2^+ \to 0^+$ cascade transitions previously made.[2] The 316, 331, 511, and 556 keV peaks in the spectrum of Fig. 2(b) are due to different contribution of activities at the gates of the peak and background.

The calibrations of energies and the determination of relative efficiency of Ge(Li) detectors for different quantum energies were made by using ^{226}Ra source. Partial level scheme with

Fig. 4. Proposed level scheme of ^{104}Cd.

their de-excitation transitions tentatively proposed is shown in Fig. 4. In the figure, the relative intensities of γ-rays are given by the width of arrows.

Since the structure of neutron deficient cadmium isotopes ^{104}Cd, ^{102}Cd, and ^{100}Cd approachs closed neutron shell, it is expected that the level structures of these nuclei are influenced by the closed shell. On the other hand, there have been reported that ^{100}Pd, ^{102}Pd, and ^{104}Pd isotopes have collective properties. The level scheme of ^{101}Pd and ^{103}Pd is also interpreted from the view point of collective excitation where the model of variable moment of inertia plays an essential role.[3] It can be argued that some cadmium isotopes show a feature of transitional nuclei. We are investigating the excited states of ^{100}Cd, ^{102}Cd, and ^{104}Cd produced via (^{12}C, 3n) and (^{12}C, 5n) reactions on ^{92}Mo, ^{94}Mo, and ^{96}Mo. Reduction and investigation of the data obtained are now in progress.

References

1) H. Kumagai and A. Hashizume: IPCR Cyclotron Progr. Rep., 9, 70 (1975);
   H. Kumagai, M. Okano, and A. Hashizume: Reports I.P.C.R., (in Japanese), 51, 102 (1975).

2) A. Hashizume, T. Inamura, T. Katou, Y. Tendow, T. Yamazaki, and T. Nomura: IPCR Cyclotron Progr. Rep., 3, 57 (1969).

3) P. Simms, G. Smith, F. Rickey, J. Grau, J. Tesmer, and R. Steffen: Phys. Rev., C9, 684 (1974).

5-3. Internal Conversion Electrons of ^{136}Ba

M. Ohshima,* Y. Itoh,* S. Hayashibe,

M. Fujioka, T. Ishimatsu,* and A. Hashizume

The low lying level structure of ^{136}Ba is investigated from β^- decay of ^{136}Cs. Internal conversion electrons were measured with a $\sqrt{2\pi}$ iron-free magnetic β-ray spectrometer installed in Institute for Nuclear Study of Tokyo University. So far, the conversion electron data of this nucleus are scarce. Only Reising and Pate[1] and Fujioka et al.[2] have reported on this subject.

Xe gas was bombarded with a 15 MeV proton beam from the cyclotron. The outline of the target chamber and the method of preparing β-ray source were presented in the previous report,[3] but some improvements in the target chamber were made recently. The inside diameter of the chamber was made larger to be 116 mmϕ and in the chamber was inserted a glass tube of inside diameter of 80 mmϕ to prevent the collector foil from the contamination of organic substances. Consequently the collection efficiency of activity amounted to more than 40 % and the source was made thinner.

Typical conversion electron spectrum in the 120 – 160 keV region is shown in Fig. 1, with the momentum resolution of the spectrometer set at 0.05 %. The presence of β^- continuum of $E_{\beta max} \simeq 330$ keV made it difficult to measure the conversion electrons in this energy range. In Table 1 is shown internal conversion coefficients calibrated with K electron of the 163 keV E3 transition for the lower energy region and of the 340 keV E2 transition for the higher one.
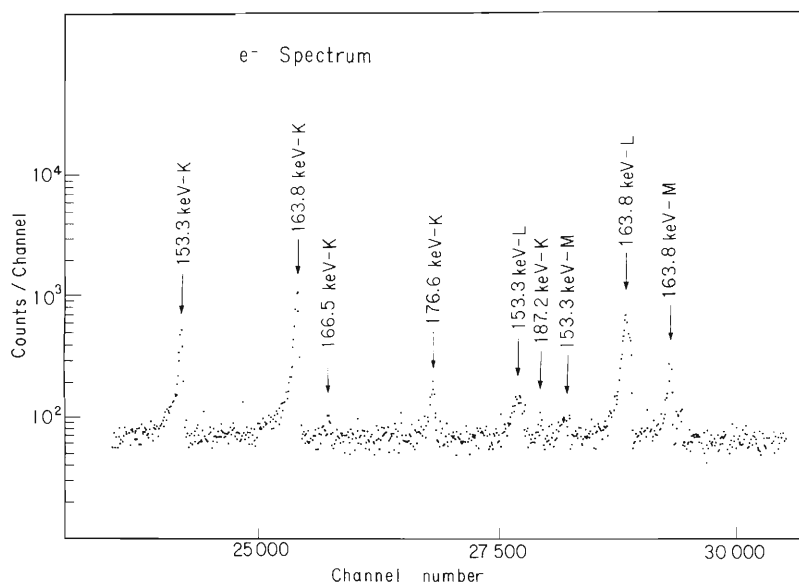

Fig. 1. Typical conversion electron spectrum in 120-160 keV region.

Table. 1. Internal conversion coefficients in ^{136}Ba.

E_γ	I_γ[a]	α_k exp.	α_k theo.		$(K/L)_{exp.}$	$(K/L)_{theo.}$	Multipolarity
66.881 (17)	4.8 (2)	0.150 (9)[b]	0.0841 8.93	(E1) (M2)			E1+(M2)
86.265 (30)	5.0 (2)	0.291 (5)	0.293	(E1)	7.24 (3)	7.26	E1
109.681 (7)	0.21 (3)	0.914 (56)	0.922		2.42 (15)	2.45	E2
153.246 (4)	5.77 (18)	0.260 (3)	0.257		3.60 (10)	3.53	E2
163.920 (2)	3.40 (12)	1.12[c]	1.12		1.25 (3)	1.26	E3
166.576 (6)	0.37 (4)	0.231 (27)	0.204 0.243	(M1) (E2)	6.87 (91)	7.51 3.79	M1+E2
176.602 (4)	10.0 (4)	0.0355 (20)	0.0406		7.36 (57)	7.65	E1
187.285 (6)	0.36 (4)	0.155 (19)	0.148 0.166	(M1) (E2)	5.65 (68)	7.55 4.16	M1+E2
273.646 (8)	11.1 (4)	0.0137 (7)	0.0126		8.83 (73)	7.83	E1
319.911 (8)	0.50 (5)	0.0318 (42)	0.0356 0.0303	(M1) (E2)			M1+E2
340.547 (8)	42.3 (13)	0.0233 (12)[a]	0.0250		5.94 (11)	5.82	E2
507.188 (10)	0.97 (3)	0.0130 (7)	0.0111 0.00798	(M1) (E2)	8.00 (100)	7.79 6.65	M1+E2
818.514 (12)	100	0.00227 (10)	0.00242		7.70 (20)	7.42	E2
1048.073 (20)	79.7 (26)	0.00150 (10)	0.00141		7.50 (26)	7.69	E2
1235.362 (23)	20.1 (7)	0.00098 (4)	0.00100		7.75 (59)	7.80	E2

a) γ-ray relative intensities are obtained from our previous work. [4]

b) These values are for $\alpha_{L_I+L_{II}+L_{III}}$. K electron is hidden among Auger electrons.

c) These values are used to normalize other electron intensities.

The proposed decay scheme is shown in Fig. 2.

For the 66 keV transition, Reising and Pate[1] measured the K and L electrons and determined the K/L ratio to be ≈ 1.3 ± 0.8 which disagrees with theoretical value of 7.01 for E1. Our more precise measurement, however, has shown that the K electron coexists with the Auger electrons and is difficult to separate from them. From the value of $\alpha_{L_I+L_{II}+L_{III}}$ we determined this transition to be almost E1 with small mixture of M2.

Three weak conversion electrons can be attributed to the transitions from newly assigned 2373 keV state to 1866 keV(4_1^+), to 2053 keV(4_2^+) and to 2207 keV(6^+) state with transition
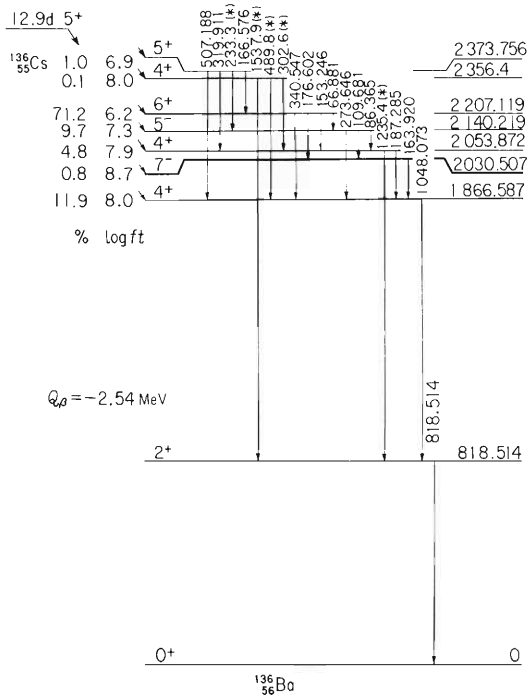
Fig. 2. Proposed decay scheme of ^{136}Ba.
(∗) Because of small transition
probabilities, it was difficult to observe
internal conversion electrons. The value
is obtained from our γ-ray work.[4]

energies of 507, 319 and 166 keV respectively. All of these transitions have M1 (+E2) character We, therefore, determined this level to be 5$^+$. This assignment is in agreement with log ft value of 6.9 which indicates this transition to be an allowed one. The branching ratios of the three transitions also support this assignment. More precise analysis is in progress.

References

1) R. Reising and B. D. Pate: Nucl. Phys., 65, 609 (1965).

2) M. Fujioka, T. Miyauchi, and H. Adachi: ibid., A95, 577 (1967).

3) M. Ohshima, M. Hirasawa, S. Hayashibe, M. Yambe, J.Katakura, M. Fujioka, T. Ishimatsu, and A. Hashizume: IPCR Cyclotron Progr. Rep., 9, 62 (1975).

4) S. Hayashibe, M. Ohshima, M. Yambe, J. Katakura, and T. Ishimatsu: Research Report of Laboratory of Nuclear Science, Tohoku University, 7, 312 (1974).

68

6. NUCLEAR INSTRUMENTATION

6-1. Efficiency for Detecting ^{8}Be Nuclei with a Position Sensitive Detector

T. Ooi, T. Motobayashi, K. Katori, and I. Kohno

The ground state of ^{8}Be decays promptly into two α particles ($t_{1/2} \sim 10^{-16}$ sec) with a break-up energy of 92 keV. The break-up α-particles from a rapidly moving ^{8}Be nucleus will travel within a cone of which axis is in the direction of the original ^{8}Be. Since the spin of the ^{8}Be ground state is zero, α particles are emitted isotropically in the ^{8}Be rest system. By vectorial addition with velocity of the center of mass, directions of α particles are confined within a narrow forward cone in the laboratory frame of reference as stated above and illustrated in Fig. 1. Therefore, at the surface of the position sensitive detector (PSD) the density of α-particles from ^{8}Be nucleus is proportional to the projection of spherical shell having a constant surface density by a point source at the target.

When two α-particles from ^{8}Be, α_1 and α_2, impinge on PSD in coincidence at point X_1 and X_2 respectively, output signals are proportional to $E_1 + E_2$ at energy contact and $X_1 E_1 + X_2 E_2$ at position contact (Fig. 1). E_1 and E_2 show energies of α_1 and α_2 respectively. The position information is

$$\frac{X_1 E_1 + X_2 E_2}{E_1 + E_2} \simeq \frac{X_1 + X_2}{2}$$

where $E_1 \simeq E_2$.
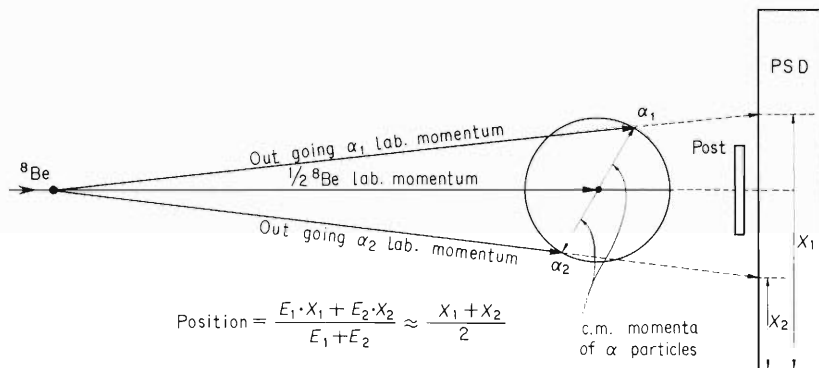
Fig. 1. Position on PSD for coincident α-particles and the post to reject other particles.

This looks as if a ^{8}Be particle came in at the point which is the average of X_1 and X_2. Strictly speaking, the point is not always on the extension of the direction of ^{8}Be, but the shift is small. For example, the shift for ^{8}Be of 20 MeV is smaller than the position resolution of PSD (=0.25mm FWHM). In this method of detection by PSD, only ^{8}Be particles can be detected with desirable solid angle and efficiency if the gate width is masked by a post and only position

signals corresponding to the area under the post are accepted so as to reject other unpaired particles as shown in Fig.1. For measurement of ^{8}Be nucleus we used a rectangular collimator which is divided by the post, or a divided circular collimator (Fig.2).
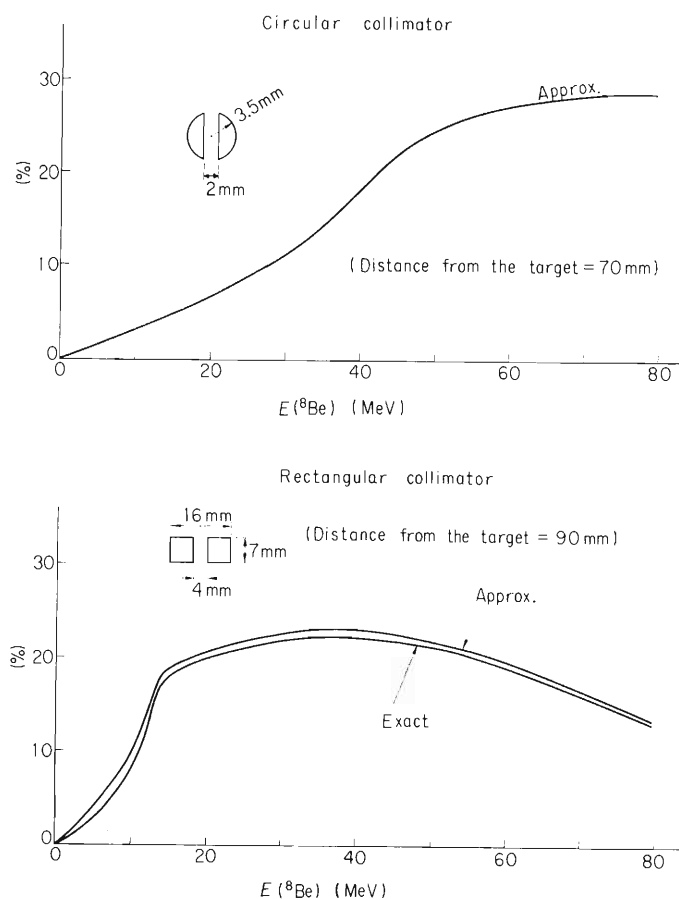
Fig. 2. Calculated detection efficiency.

To calculate overall detection efficiency of the divided collimator the ratio of number of events where the break-up α particles come in through two windows of the divided collimator to number of all ^{8}Be nucleus which would come in the whole gate width must be calculated and averaged.[1] We carried out both an exact and an approximate calculation of overall detection efficiency. In the approximate calculation we assumed that subsequent paths of two break-up α particles make the same angle with the original direction of ^{8}Be. Then, the calculation of detection efficiency reduced to an integration of the α-particles density on the detector surface limited by the divided collimator. The results calculated are shown in Fig.2. It is known from this results that in the energy of ^{8}Be below 25 MeV the divided rectangular collimator is preferable, but the divided circular collimator is better in the energy above 30 MeV for geometries given in the Fig.2.

Reference

1) T. Ooi, T. Motobayashi, K. Katori, and I. Kohno: Reports I.P.C.R., (in Japanese), 52, 145 (1976).

6-2. A Modified △E-E Counter Telescope

T. Motobayashi

To measure the reaction products of the heavy ion reaction more efficiently than before, the counter telescope was modified so as to achieve detection at many (four in this case) angles simultaneously.[1] This system is especially usefull when the tar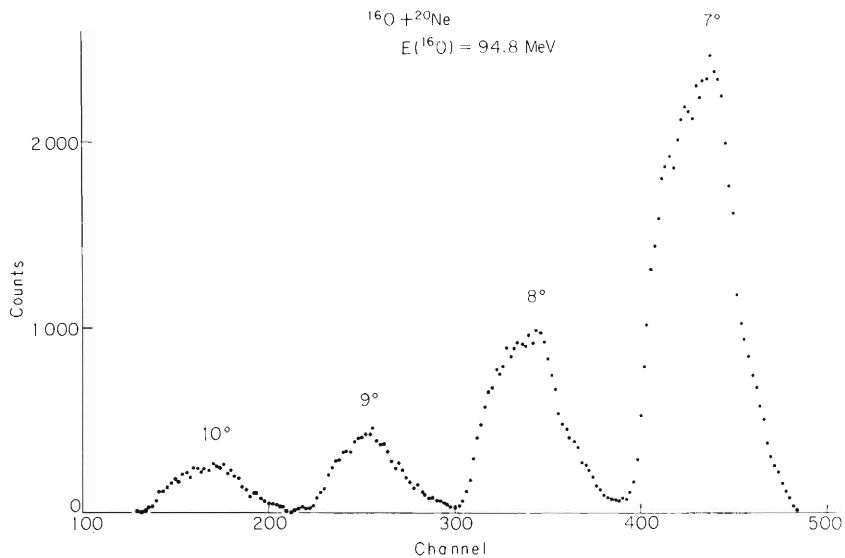get is so thin (for example a gas target) or the beam intensity is so low that the counting rate never goes up higher than the limit restricted by the detection circuit.

The modified counter telescope[2] consists of position sensitive solid state E counter (500μ thick, 7mm×25mm), △E counter (30μ, 200mm^2), and four slit collimators as illustrated in Fig. 1. The slits are all 1.5mm wide and 5.5mm high and 3mm apart from each other. In order to detect the reaction products at 1° intervals, the distance between four collimators and the target (or the front slit in the case of gas target) is taken to be 172mm. These four slit holes were carefully finished so as to have the same area in order to get the same solid angle for all four angles.

In Fig. 2 the block diagram of the detection circuit is shown. To get position signals and particle identification signals (PI signals), a position sensitive detector analyzer (dividing circuit) and a particle identifier[3] were employed. A fast coincidence between △E and E signals were taken and a pile up rejector[3] was used to eliminate chance coincidences except the ones which occur in one burst of the cyclotron. The position and the PI signals together with the energy signals were fed into three pararell ADC's after eliminating the elastic scattering events. The

Fig. 1. Schematic view of the modified counter telescope.

PA: pre-amplifier   MA: main amplifier

TEA: timing filter amplifier   PI: particle identifier

CFTD: constant fraction timing discriminater

PSD An.: position sensitive detector analyzer

TSCA: timing single channel analyzer

LGS: linear gate stretcher

Fig. 2. Block diagram of the detection circuit.

Fig. 3. Position spectrum obtained by bombarding ^{20}Ne with ^{16}O at 94.8 MeV.

signals from these ADC's were written in a magnetic disk by OKI 4500C computer, and were analyzed and monitored on-line, or transfered again to a magnetic tape for a later off-line analysis. An example of the position spectrum is shown in Fig. 3, in which each peak corresponds to different detection angle. The energy spectrum of a certain particle in a certain angle is obtained by putting an appropriate gate on PI and position spectum.

References

1) Modifications 6f this type has already achieved, for example; I. Paschopoulos, P. S. Fisher, N. A. Jelley, S. Kahana, A. A. Plit, W. D. Rae, and D. Sinclair: Nucl. Phys., A252, 173 (1975).

2) Fabricated in the work shop of IPCR.

3) Made by F. Shimokoshi (the University of Tokyo).

6-3. A Gas Target System for Heavy Ion Reactions

T. Motobayashi

A gas target system was made to use it in the study of the heavy ion transfer reactions. It is advantageous to employ a gas target because of following reasons: 1) rare gas material (Ne for example) can be used as a target: 2) the target with little impurity is easy to obtain: and 3) target thickness is rather easy to estimate by measuring the pressure of the gas.

In Fig. 1 the gas cell[1] is illustrated. The windows through which the beam passes are covered with 1.25μ m thick nickel foils and the other windows with 4μ m thick mylar foils. The energy spread of the ions after passing through the foil was measured to be about 8% of the average energy loss in the foil. This cell is able to hold the gas of about 300 torr when placed in the vacuum. The typical pressure of the gas in the experiment was about 70 torr. The beam was collimated by a collimator consisting of two slits, one of which determines the beam spot 2mm wide and 6mm high on the entrance window and prevents the scattered particles of the stray beam from entering into the detection system.

The detection system consists of two slits and shielding strips as shown in Fig. 1. The front slit (1mm wide) placed just 5mm from the window of the cell is made in one body with the shielding strips as is seen in Fig. 1 in order to detect the reaction products in forward angles without cutting the beam coming out from the cell. Consequently the minimum angle achieved was 7°. The shielding strips prevent other particles than those coming through the
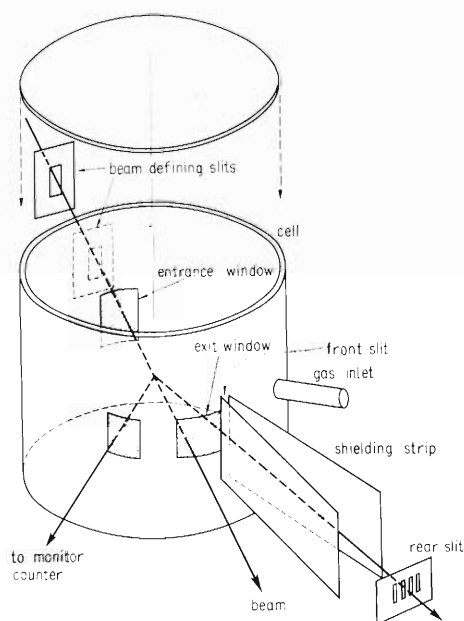

Fig. 1. The gas target system: the gas cell and the detection slits. The diameter of the cell is 60mm.
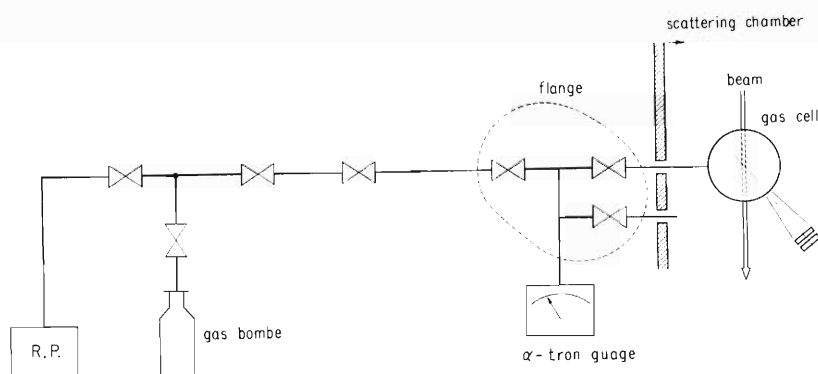

Fig. 2. Gas feeding system.

front slit from going into the detector through the rear slit. The rear slit consists of four rectangular holes.[2] The effective area of the target in the gas is determined by these two slits and the beam itself; horizontally by the two slits and vertically by the beam itself. This effective target area together with the solid angle of the slit system was estimated from the geometry of the setting by numerical calculations. The errors in these estimation come from the misalignment of the detector slit system and the errors in estimating the size of the slits. Alignment was performed with the telescope and its error was estimated to be of the order of 0.1mm. The size of the slits was measured with the microscope and the error was less than 0.05mm. These results suggest the total error in estimating the effective target area and the solid angle to be less than 10%.

Figure 2 shows the gas feeding system. The pressure was measured by an α-tron vacuum gauge[3] and monitored throughout the experiment. Since target thickness depends not only on the pressure of the gas but on the temperature, we must know the temperature correctly. However, it is rather difficult to know the temperature during the experiment because the temperature may go up being heated by the beam. Hence, the elastic scattering yield was monitored by another counter instead of measuring the temperature.

An example of the energy spectrum obtained by using this gas target system is shown in Fig. 3. The peak of double scattering caused by the two nickel foils of the windows are seen beside the elastic scattering peak. Angular distribution obtained for elastic scattering is shown in Fig. 4. In that case without any re-normalization a good fit to the data was obtained by an optical model calculation with a reasonable set of the parameters.
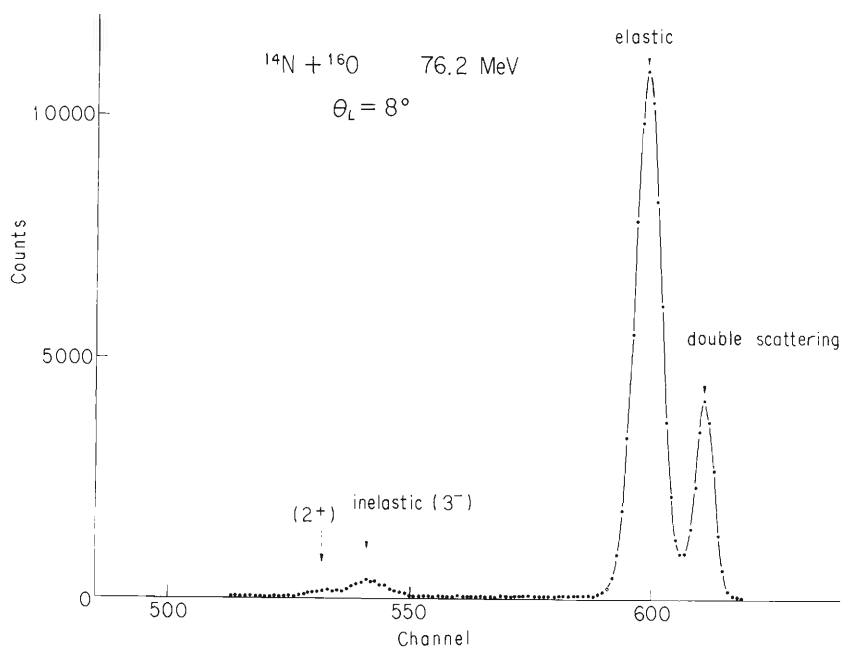

Fig. 3. Energy spectrum of the elastic scattering of ^{14}N on ^{16}O at 76.2 MeV obtained by using the gas target.
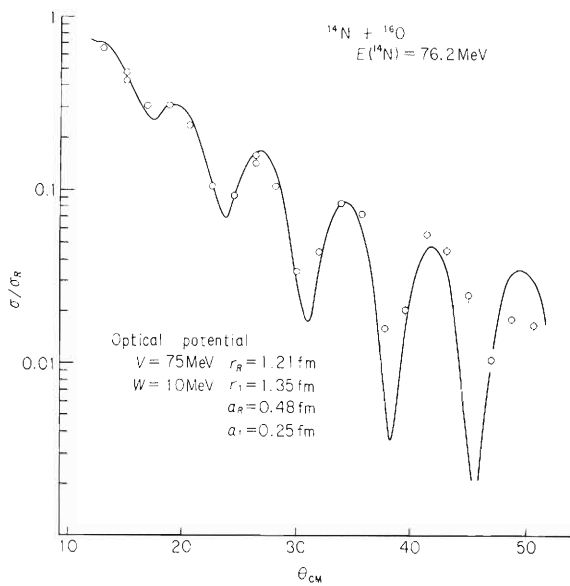
74

Fig. 4. Angular distribution of the elastic scattering of ^{14}N on ^{16}O. The solid line corresponds to the optical model calculation (see Ref. 4).

References

1)   All parts of the system were made in the work shop of IPCR.

2)   T. Motobayashi: IPCR Cyclotron Progr. Rep., 10, 70 (1976).

3)   Alphatron type 82.0 Norton Vacuum Equip. Div. 160 Charlemont St. Newton. Mass. USA (see also IPCR Cyclotron Progr. Rep., 6, 43 (1973); M. Odera et al.).

4)   T. Motobayashi, I. Kohno, T. Ooi, and S. Nakajima: IPCR Cyclotron Progr. Rep., 10, 35 (1976).

6-4. Computer Development

On-line Computer OKITAK 4500

T. Inamura, T. Wada, M. Ishihara, and H. Kamitsubo

Extensive use has been made of magnetic tapes to record multiparameter data, such as particle-γ particle-particle coincidences and $\triangle$E-E signals from particle identifiers, and to play them back for analyses later on. Eventually there is a great need for a much advanced magnetic tape unit to save time. Because of this, the present magnetic tape unit is going to be replaced by a much faster and reliable unit in a few months. The new unit is OKI 798F: the recording density is 1600 bpi, being twice that of the present unit; the tape speed is 125 ips in reading and writing, being faster than three times the present speed; and the transfer speed becomes 200 kbytes/sec, about eight times as fast as the present transfer speed. This will improve handling of magnetic tapes greatly and save considerable time during experiments on the cyclotron.

F. Shimokoshi

A particle identification system based on the Bethe-Bloch formula for the rate of energy loss of charged particles in the stopping material has been reported by several authors.[1,2] When a conventional telescope consisting of $\triangle E$ and E counters is used, the identifier output signal, PI, can be given by

$$PI = (\triangle E + \epsilon_o) \ (E + \kappa\triangle E + E_o)^{0.75}, \tag{1}$$

where E_o and κ are parameters adjusted experimentally to keep the identifier output constant for change of the particle energy and ϵ_o is a circuit constant. This formula is known to be useful in identification of light particles, such as p, t, d, ^{3}He, α, Li, Be, and B. However, it is rather unsatisfactory in identifing heavier particles. To improve the performance, a function $G(\triangle E)$ is introduced instead of $\kappa\triangle E$ (term).

$$G(\triangle E) = L : \frac{e^{M \cdot \triangle E} - 1}{e^{M \cdot 10} - 1} \times 10$$

$$= L_1 \ (\triangle E) + L_2 \ (\triangle E)^2 + L_3 \ (\triangle E)^3 + \cdots \cdots \cdots, \tag{2}$$

where L is the gain and M is the slope of the function.
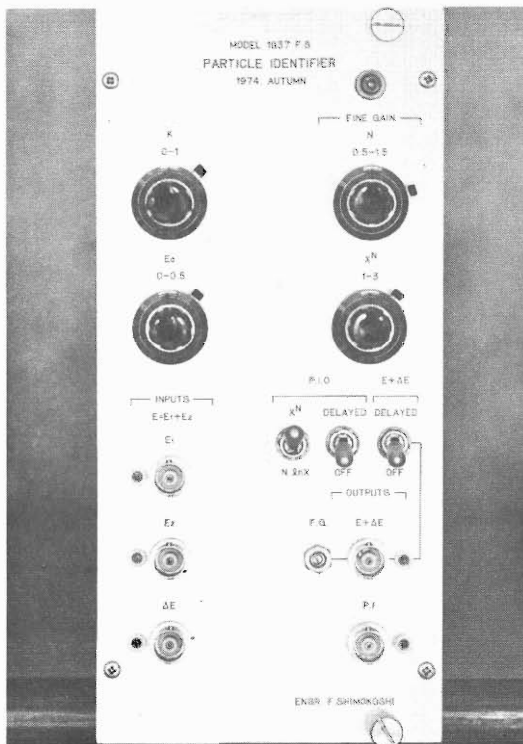
Then we have

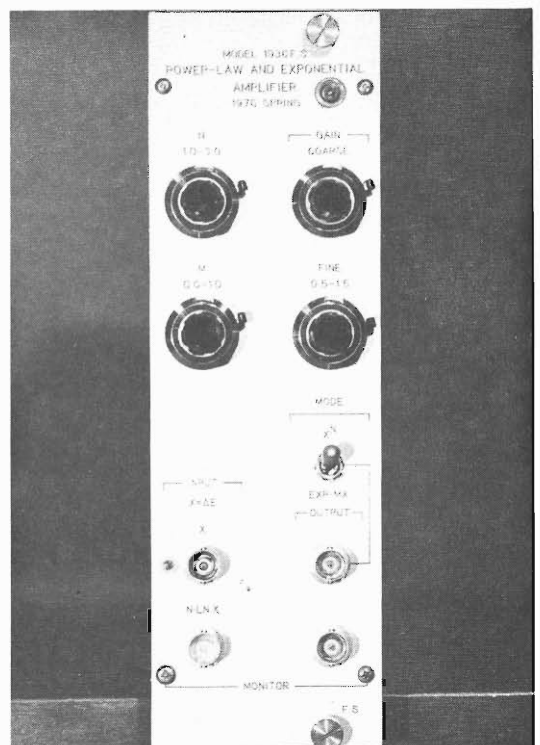Fig. 1.   Particle identifier based on the Eqn. (2).

Fig. 2.   An adapter to the particle identifier: $G(\triangle E)$ function generator for heavy particles.
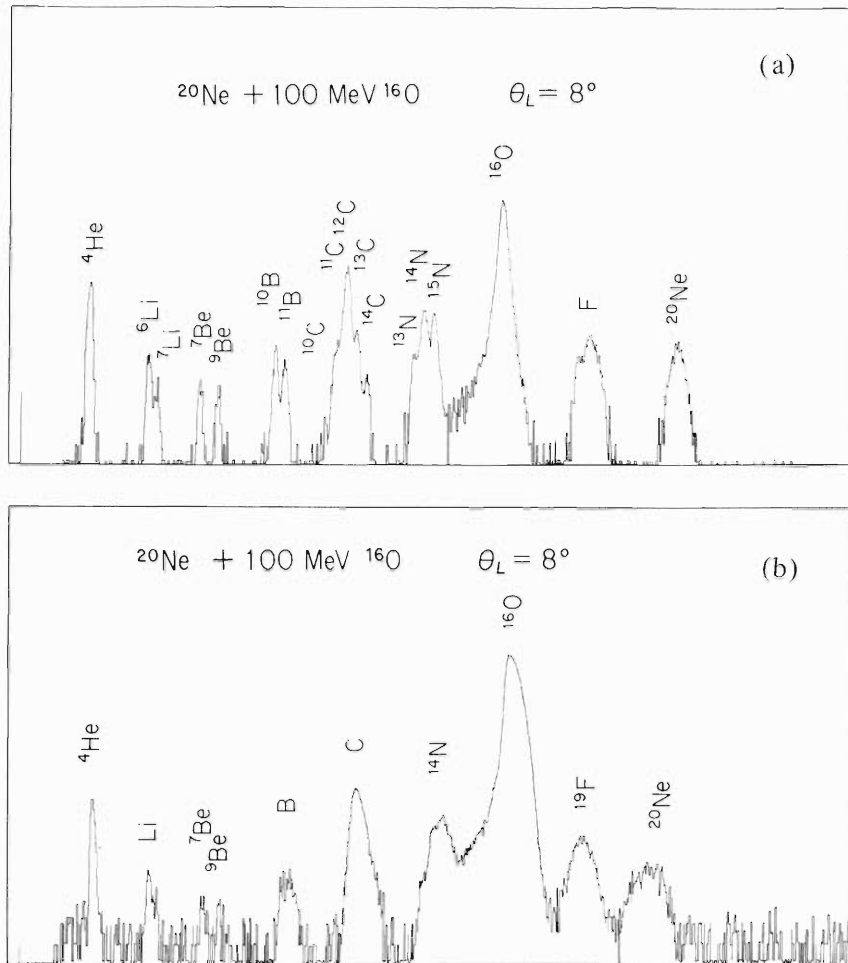
Fig. 3. PI spectrum: (a) is the spectrum observed with the adapter and (b) is
the spectrum observed without the adapter.

$$PI = (\triangle E + \epsilon_o) \ [E + G(\triangle E) + E_o]^{0.75} \tag{3}$$

A function generator for $G(\triangle E)$ is constructed as an adapter to the identifier based on Eqn. (1)
for user's convenience.

Figure 1 shows our particle identifier and Fig.2 shows the adapter.

This particle identification system has been tested on the ^{20}Ne + 100 MeV ^{16}O reaction;
the ^{16}O beam was obtained from the cyclotron, and a 30 μm Si-surface barrier detector was used
as the $\triangle E$ counter.

The PI spectrum obtained is shown in Fig.3, together with the best spectrum obtained
without the adapter for comparison. It should be noted that for the former, L_1, the coefficient
of the first order of $\triangle E$ in Eqn. (2) became 0.4, while κ=0.8 was taken for the latter.

References

1) R. G. Stokes, J. A. Northrop, and K. Boyer: Rev. Sci. Instr., 29, 61 (1958).

2) A. D. Harmanci: Nucl. Instr. and Meth., 86, 109 (1970).

7. ATOMIC AND SOLID-STATE PHYSICS

7-1.   K X-ray Spectra of Al, Ti, Cr, Fe, and Ni Induced by Nitrogen Ions

Y. Awaya, M. Akiba, T. Katou, H. Kumagai,

Y. Tendow, K. Izumo, T. Takahashi, A. Hashizume,

M. Okano, and T. Hamada

The $K\alpha$ and $K\beta$ X-ray spectra of Al, Ti, Cr. Fe, and Ni induced by 84-MeV N-ions were studied using a Bragg crystal spectrometer.[1] The $K\alpha$ spectra of Ti induced by 95-MeV and 71-MeV N-ions were also measured in order to study the dependence of the spectrum pattern on the incident energy.

After the previous report[1] was accomplished, the energy resolution of the crystal spectro-meter was improved to be 10 eV FWHM for the flourescent Ti $K\beta_{1,3}$ X-rays (4.931 keV) and 1.9 eV for the Al $K\alpha_{1,2}$ X-rays (1.54 keV). In the present work, the K X-rays of Al were measured by an EDDT (200) crystal and a proportional counter and the K X-rays of elements heavier than Ti were measured by a LiF (200) crystal and a scintillation counter. The targets, ranging in thickness from 0.8 mg/cm^2 to 1.4 mg/cm^2, were placed with an inclination of $60°$ with respect to the ion beam. The present incident energy of heavy ions per nucleon is higher than that in any other works of this kind.

The K X-ray spectra of Al, Ti, Cr, Fe, and Ni obtained are shown in Fig. 1. Each peak is labelled by symbol $K^m L^n$ which denotes the corresponding intial configuration having m K-shell vacancies and n L-shell vacancies. The symbol α or β attached to each peak means that the peak belongs either to $K\alpha$ or $K\beta$ transition.

Following experimental results are obtained.

(1)   The incident ions act more proton-like in multiple ionization process as the incident energy increases or the value of Z_1/Z_2 decreases, where Z_1 and Z_2 are the atomic number of the projectile and the target element respectively.

(2)   In the Al spectrum, the $K\alpha$ hypersatellites are excited more strongly than $K\beta$ satellites in the present work, though only the $K\beta$ satellites have proviously been observed in the case of 5-MeV N-ion impact.[2] This is because the projectile penetrates deeper into the target atom as the incident energy increases.

(3)   The width of the satellite line is always larger than that of the diagram line. This is considered to be caused by multiplet splitting, variation of distribution of L-shell vacancies among the subshells, and the M-shell ionization which occurrs in addition.
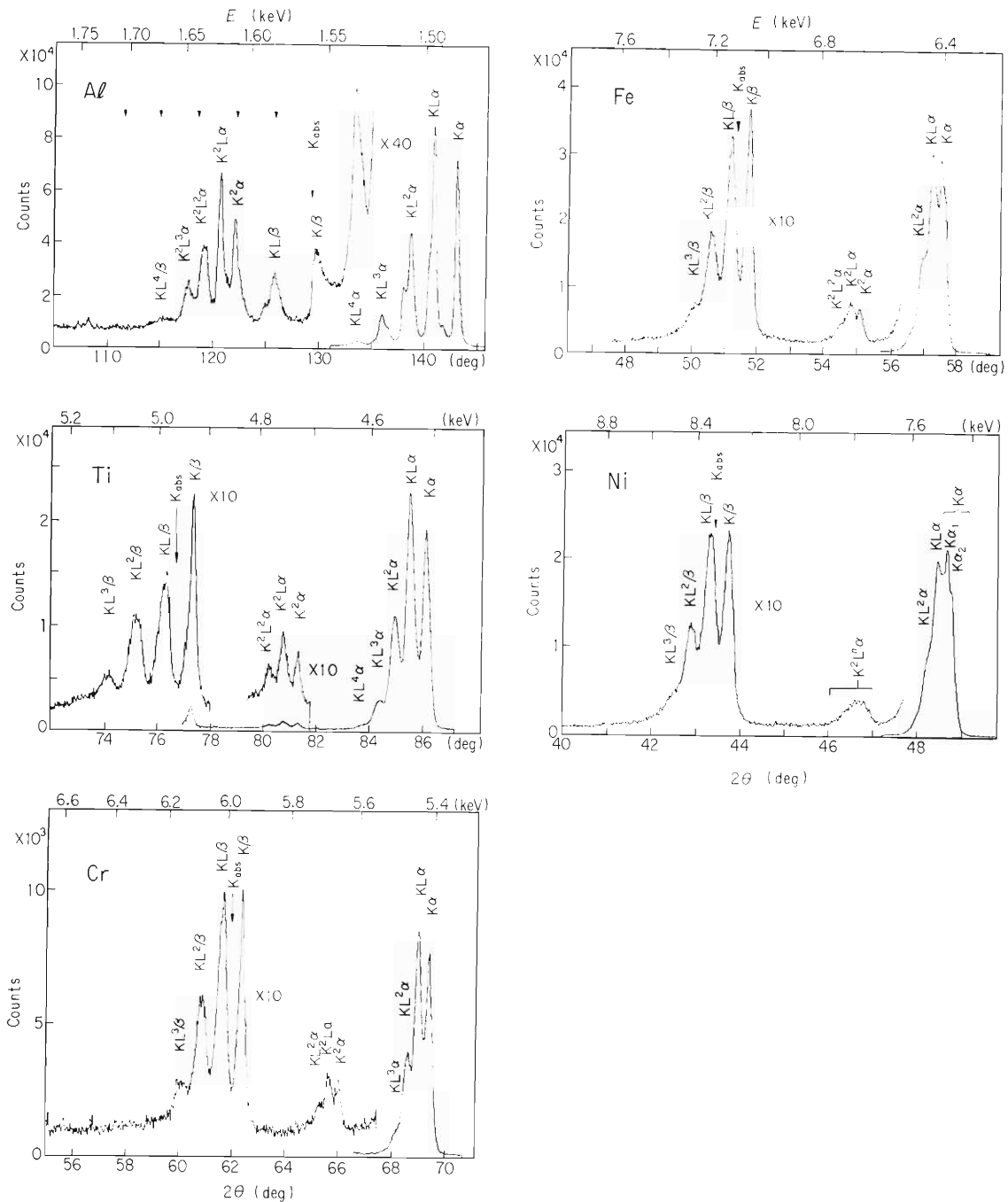
Fig. 1. The K X-ray spectra of Al, Cr, Ti, Fe, and Ni induced by 84 MeV N-ions. The K_{abs} denotes the K-absorption edge of the target element. The arrows indicate the positions of $KL^n\beta$ (n=1∼5) lines of Al observed by Knudson et al. [2]

(4) The values of the energy separation between the $K\alpha_{1,2}$ line and the $KL^n\alpha$ line (n=1∼3) and those between the $K^2\alpha$ line and the $K^2L^n\alpha$ line (n=1∼3) are almost equal for each value of n. The values of energy difference between the $K\alpha_{1,2}$ and $KL^n\alpha$ lines, the $K^2\alpha$ and $K^2L^n\alpha$ lines, the $K\alpha_{1,2}$ and the $K^2\alpha$ line, and the $K\beta$ and $KL^n\beta$ lines are shown in Fig. 2 as function of Z_2. The peak positions were determined by the chi-square fitting of multiple Gaussian curves to the overlapping peaks.

80

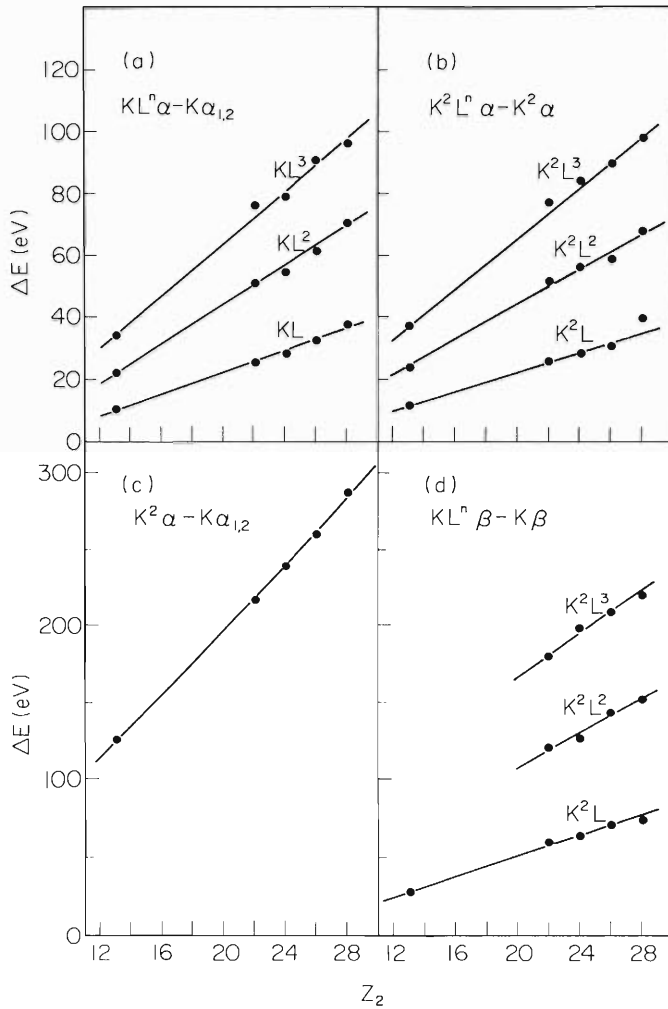The analysis concerning the intensity of satellite or hypersatellite lines relative to the diagram line is in progress.

Fig. 2. Plot of $KL^n\alpha$ satellite energies relative to $K\alpha_{1,2}$ (a), of $K^2L^n\alpha$ relative to $K^2\alpha$ (b), of $K^2\alpha$ relative to $K\alpha_{1,2}$ (c) and of $KL^n\beta$ relative to $K\beta$ (d). The curves are drawn for visual aid.

References

1) Y. Awaya, Y. Tendow, H. Kumagai, M. Akiba, T. Katou, and T. Hamada: IPCR Cyclotron Progr. Rep., 9, 79 (1975).

2) A. R. Knudson, D. J. Nagel, P. G. Burkhalter, and K. L. Dunnig: Phys. Rev. Lett., 26, 1149 (1971).

7-2. Measurement of Radiative Electron Rearrangement in Ti

M. Akiba, Y. Awaya, Y. Tendow, A. Hashizume,

T. Katou, H. Kumagai, T. Takahashi,

M. Okano, and T. Hamada

Recently low-intensity X-ray peaks have been observed in the energy region just below the $K\alpha_{1,2}$ line.[1]−[5] These peaks were first considered to be the result of the KLM or KLL radiative Auger effect,[1] or of the excitation of one or more volume plasmons in the target material by the $K\alpha_{1,2}$ X-rays.[2] As a more probable explanation, the radiative electron rearrangement (RER) process[4],[5] was proposed later. This process assumes that the $(1s)^{-1} (2p)^{-n}$ vacancy configuration transfers to the $(2s)^{-2} (2p)^{-n+1}$ one.

A $4\mu m$ thick Ti target was bombarded with 95-MeV N-ions. A flat crystal spectrometer[6] equipped with LiF (200) crystal and a NaI(Tl) scintillation counter was used to analyze the X-rays. A step angle of the spectrometer was $0.02°$, and the integrated beam current was 3 μC at each angular setting.

The X-ray spectrum obtained is shown in Fig. 1. The RER peak positions[3] are indicated by the arrows. The symbol RER_n denotes the transition from the $(1s)^{-1}(2p)^{-n}$ configuration to the $(2s)^{-2}(2p)^{-n+1}$ one. As the intensities of the RER lines are expected to be less than 0.2% of the $K\alpha_{1,2}$ line, the present poor counting statistics did not allow these lines to be observed. We are planning to make further investigation of the RER process with improved counting statistics.
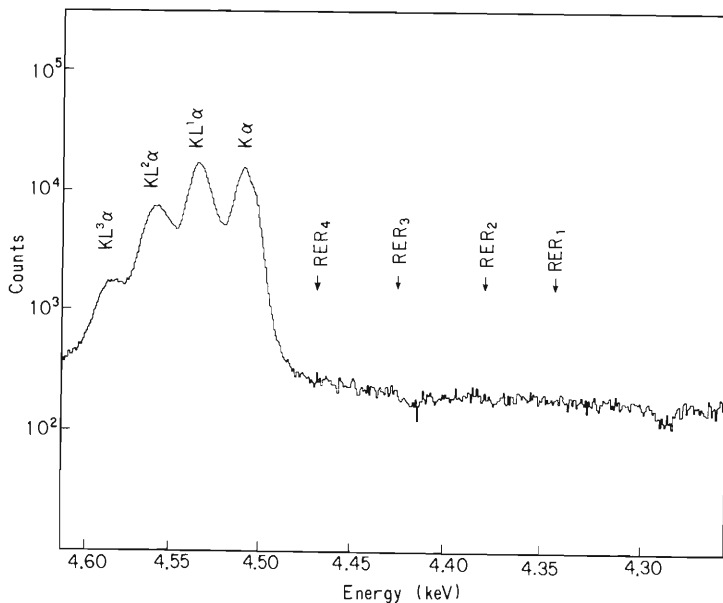

Fig. 1. Ti X-ray spectrum induced by 95 MeV N-ions in the RER energy region. The arrows indicate the RER_n peak positions (n=1∿4). The peaks labelled by $KL^n\alpha$ are the $K\alpha$ diagram and satellite lines.

82

References

1) P. Richard, C. F. Moore, and D. K. Olsen: Phys. Lett., 43A, 519 (1973).

2) J. McWhether, J. E. Bolger, H. H. Wolter, D. K. Olsen, and C. F. Moore: ibid., 45A, 57 (1973).

3) P. Richard, J. Oltjen, K. A. Jamison, R. L. Kauffman, C. W. Woods, and J. M. Hall: ibid., 54A, 169 (1975).

4) K. A. Jamison, J. M. Hall, and P. Richard: J. Phys. B, 8, L458 (1975).

5) J. Oltjen, R. L. Kauffman, C. W. Woods, J. M. Hall, K. A. Jamison, and P. Richard: Phys. Lett., 55A, 184 (1975).

6) Y. Awaya, Y. Tendow, H. Kumagai, M. Akiba, T. Katou, and T. Hamada: IPCR Cyclotron Progr. Rep., 9, 79 (1975).

7-3. The L₂-L₃X Coster-Kronig Transition Probability in Hf

M. Akiba, Y. Awaya, M. Okano, and T. Hamada

Values of L_2-L_3X Coster-Kronig transition probability, f_{23}, have been measured for some elements ranging from Z=63 to Z=96. Most of the values obtained for elements of Z≤ 90 are larger than the theoretical values by about 30%.[1] As the f_{23} value for Hf (Z=72) was not experimentally determined, it was measured using the coincidence method of K and L X-rays from the decay of ^{179}Ta to ^{179}Hf by the electron capture process.

^{179}Ta was produced by the ^{179}Hf(p, n)^{179}Ta reaction at the proton energy of 14 MeV, chemically separated from the Hf target[2] and deposited on a 5-μm Mylar film to prepare a source. The K X-rays were detected by a 90-cm³ Ge(Li) detector, while the L X-rays by a Si(Li) detector with 195-eV energy resolution (FWHM) for the 5.9-keV X-ray. The resolving time of the standard fast-slow coincidence system was 90 nsec. These detectors were set closely face to face to reduce the angular correlation effect of K X-rays and L X-rays.

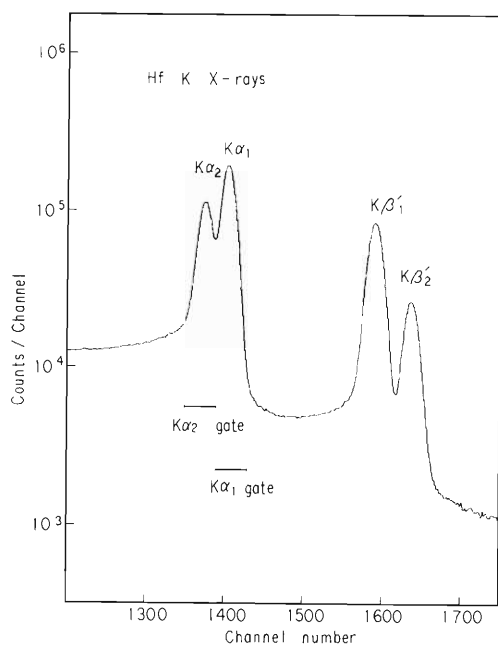Hf K X-ray spectra and gate positions of $K\alpha_1$ and $K\alpha_2$ lines are shown in Fig. 1.

Fig. 1. Hf K X-ray spectra following the decay of ^{179}Ta. The gate positions of $K\alpha_1$ and $K\alpha_2$ lines are indicated.

Figure 2 shows spectra of the L X-rays and the L X-rays in coincidence with $K\alpha_1$ and $K\alpha_2$ X-rays. Some impurity lines are observed in the L X-ray spectrum. They correspond to the Cr Kα, Mn Kα (+ Cr Kβ) and Fe Kα (+ Mn Kβ) X-rays energetically. Efforts were made to reduce the impurity lines but it failed to remove them thoroughly. There are two possible origins of impurity lines. One is that they would be fluorescent K X-rays from Cr, Mn or Fe which are contained in the housing of the Si(Li) detector induced by Hf K or L X-rays. The other is that there would be a radioactive impurity which emits the Cr, Mn or Fe X-rays. In any way, as there is the possibility that the Fe Kβ line and the Hf L$_\ell$ line overlap each
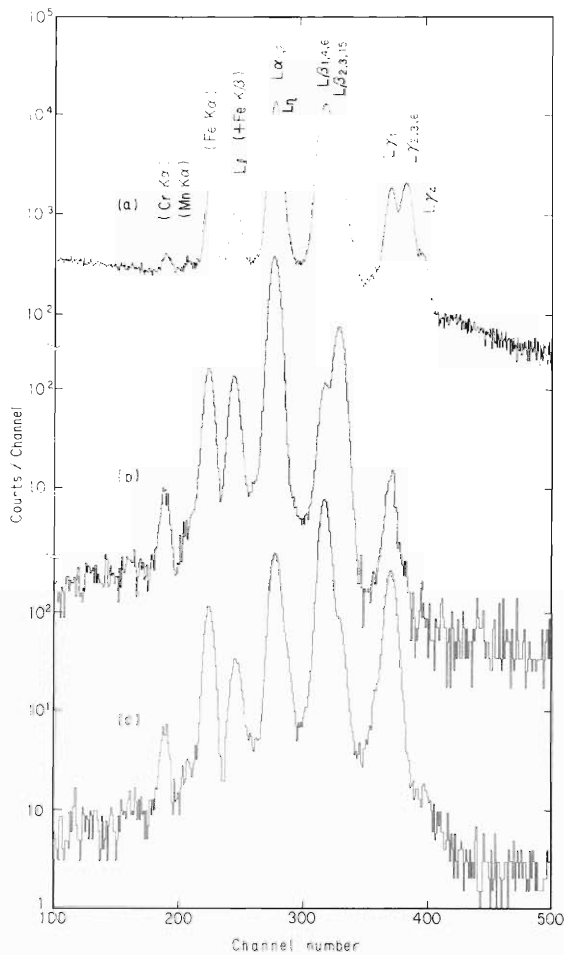
Fig. 2. Spectra of the L X-rays (a) and the L X-rays in coincidence with the $K\alpha_1$ X-rays (b) and with the $K\alpha_2$ X-rays (c).

other, the value of f_{23} is obtained as follows without adopting the $L\ell$ line in the calculation:

$$f_{23} = \frac{C_{L\alpha}(K\alpha_2)\, S_{K\alpha_1}}{C_{L\alpha}(K\alpha_1)\, S_{K\alpha_2}}$$

where $C_I(J)$ is the number of coincidence counts of I X-rays with J X-rays and S_I is the number of single counts of I X-rays.

A preliminary result obtained for the L_2-L_3 X Coster-Kronig transition probability in Hf is

$$f_{23} = 0.22 \pm 0.04$$

This value is larger than the theoretical one, 0.14. The difference between the present value and the theoretical one shows the similar tendency to that found for other elements.

References

1) W. Bambynek, B. Crasemann, R. W. Fink, H. U. Freund, H. Mark, C. D. Swift, R. E. Price, and P. Veugopala Rao: Rev. Mod. Phys., 44, 716 (1972);
   M. R. Zalutsky and E. S. Macias: Phys. Rev. A, 11, 71 (1975).

2) F. F. Felber, Jr.: University of California Radiation Laboratory Report UCRL-3618 (1957) (unpublished).

7-4.   Energy Loss and Straggling of C and He Ions in Foils of Metals and Compounds

T. Takahashi, Y. Awaya, T. Doke,* T. Hamada, A. Hashizume,

K. Izumo, H. Kumagai, T. Tonuma, and S. Uchiyama*

The mean excitation potential I in the Bethe stopping power formula may be calculated for alloys and compounds by

$$\ln I_B = (\sum_i n_i Z_{2i})^{-1} \sum_i n_i Z_{2i} \ln I_i, \quad (1)$$

if Bragg's additivity rule holds.   Here, I_B is the mean excitation potential defined by equation (1), n_i is the fractional number of atoms of the component i , Z_{2i} is the atomic number of the component i and I_i is the mean excitation potential of the component i .[1] Even for metal alloys, however, I_B deviates from the experimentally determined value I_{exp}.   Recently, Porter et al.[2,3] showed that I_{exp} of a cobalt-based alloy determined from the Bethe formula is about 15 % lower than I_B for 2.5 to 7.0 MeV deuterons.   When the second Born approximation is introduced into the Bethe stopping power formula, which has a term proportional to Z_1^3 the discrepancy between I_B and I_{exp} becomes much smaller for this alloy.

To test the Z_1^3 dependence more directly, we just began experiments on simple substances, e.g., Al, Ni, Au, and Pb foils, using C and He ions.   We are also planning to examine whether I_{exp} values for C ions are the same as for He ions in metals and compounds.   The values of I_{exp} for compounds, with and without Z_1^3 correction, will then be compared with I_B obtained from equation (1).

As for the straggling of heavy ions, the discrepancy between the theory and experiment is pointed out.[4]   We are planning to clarify the cause of the discrepancy and to establish a more plausible theory.

References

1)   C. Tschalar and H. Bichsel: Phys. Rev., 175, 476 (1968).
2)   L. E. Porter, L. C. McIntyre, and W. Haeberli: Nucl. Instr. Methods, 89, 237 (1970).
3)   L. E. Porter and C. L. Shepard: ibid., 117, 1 (1974).
4)   V. V. Avdeichikov, E. A. Ganza, and O. V. Lozhkin: ibid., 131, 61 (1975).

* Science and Engineering Research Laboratory, Waseda University.

7-5. Bonding Effects in X-ray Spectra Induced by Heavy Ions

M. Uda, K. Maeda, Y. Awaya, M. Kobayashi,

Y. Sasa, and H. Kumagai

X-ray emission spectra are sensitive to the chemical environment of the emitting atom and are of great use for the study of bonding effects. It has been recently established that heavy ion excitation enhances X-ray satellites due to multiple ionization, which appear at energies higher than the diagram X-ray lines. Ion induced X-ray spectra are then expected to show the enhanced chemical shifts of the atom since multiple ionization will reduce the electron shielding of the nuclear charge.

The present study deals with the chemical effects on both inner-shell transitions, Fe
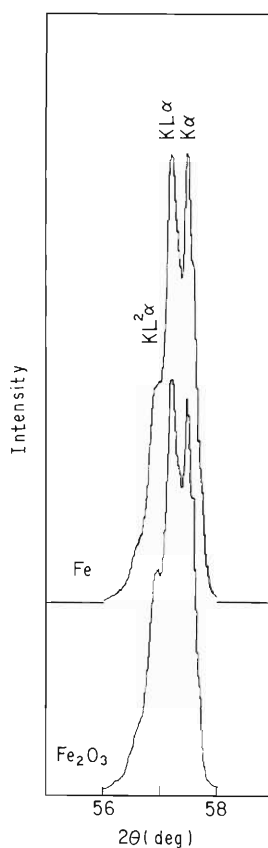

Fig. 1. Fe $K\alpha$ spectra from Fe foil of 5mg/cm^2(6μm), and α-Fe$_2$O$_3$ of 7mg/cm^2 (13μm) on Al backing and coated with thin carbon film. LiF(200) and a scintilation counter were used.
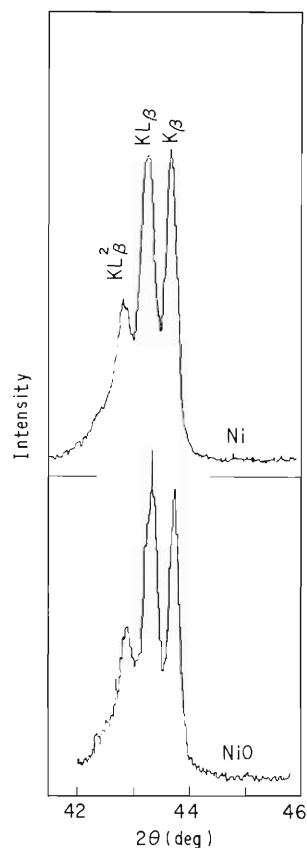
Fig. 2. Ni $K\beta$ spectra from Ni foil of 0.9mg/cm^2(1μm), and NiO of 1.1mg/cm^2 (1.5μm) on Al backing and coated with thin carbon film. These spectra were measured with LiF(200) and a scintilation counter.

Kα and Al Kα, and valence band spectra, F Kα, Al Kβ, and Ni Kβ. For this purpose, spectra from Fe, α-Fe$_2$O$_3$, Al, NaF, Na$_3$AlF$_6$, AlF$_3$, (CF$_2$)$_n$ . . . . . teflon, Ni and NiO were examined. The target materials were in the form of thin films of a few μm in thickness

Fig. 3. Al Kα and Kβ spectra from Al foil of 0.9mg/cm^2 (3μm), and AlF$_3$ of 1.1mg/cm^2 (4μm) on Ni backing and coated with thin carbon film. X-rays were measured with the gas flow proportional counter through EDDT(020).

Fig. 4. F Kα spectra from NaF of 1.4mg/cm^2 (5μm), Na$_3$AlF$_6$ of 1.5mg/cm^2 (5μm), AlF$_3$ of 1.0mg/cm^2 (3μm) and teflon of 0.9mg/cm^2 (4μm). Except the teflon which was self-supported, all the other targets were coated with thin carbon film on mylar backing. RAP(001) and the proportional counter were employed.

This thickness was suitable to reduce the absorption and the charging effects and also the temperature rise caused by the stopped ions in the target during measurements. N^{4+} of 84 MeV was used throughout the experiments. All the X-ray spectra were obtained with an on-line Bragg spectrometer described elsewhere.[1] Each line in Figs. 1 - 4 is labeled by the electron vacancies in the initial state.

Figures 1 and 2 show Fe $K\alpha$ and Ni $K\beta$ spectra from corresponding metals and oxides respectively. No appreciable change in spectra from the metals and the oxides could be observed under these experimental conditions. Figure. 3 gives Al $K\alpha$ and $K\beta$ spectra from Al and AlF_3 which are modified with satellites caused by the multiple ionization in L shells and with the hypersatellites resulting from double holes in K shell and multiple holes in L shells. Difference between $K\alpha$ spectra from Al and AlF_3 is not remarkable. However, F $K\alpha$ emission spectra from several fluorides shown in Fig. 4 reflect differences of the chemical environment. Increasing the electronegativity or the effective charge of F atom from teflon to NaF through AlF_3 and Na_3AlF_6, relative intensities of the satellites caused by the multiple ionization of L shells were increased. This fact suggests that differences in the electronic configulations around atoms can be seen in an enhanced manner under appropriate experimental conditions. The study of the effect of energy change of the incident ions is under way.

Reference

(1) Y. Awaya, Y. Tendow, H. Kumagai, M. Katou, and T. Hamada: IPCR Cyclotron Progr. Rep., 9, 79 (1975).

7-6. Positron Study of Phase Transformations in Alloys

S. Tanigawa,* R. Nagai,* M. Doyama,* and N. Shiotani

The line shape measurements of positron annihilation radiations were carried out to understand the aging behavior of quenched Al-Ag and Al-Zn alloys and to clarify the crystallization mechanism of amorphous Pd-Si and Ni-P alloys.

The Al-12 at.% Ag alloy was homogenized at 530°C for two hours and then quenched into ice water. The isochronal annealing (held at each temperature for 10 min.) was performed. The results are shown in Fig. 2. The definition of S-parameters is shown in Fig. 1. S-parameters decreased in the temperature range between 50°C and 100°C, increased at about 180°C, had a small hump at about 200°C, and then greatly increased at about 260°C. The stage near 75°C, the hump near 200°C, the dip near 220°C and the large increase near 260°C are due to the annealing of quenched-in vacancies, the formation of spherical G. P. zones, the reversion of the G. P. zones and the formation of hexagonal structure of γ' phase, respectively. Similar measurements were performed for the Al-10.3 wt.% Zn alloy, which was homogenized at 300°C for two hours and quenched into
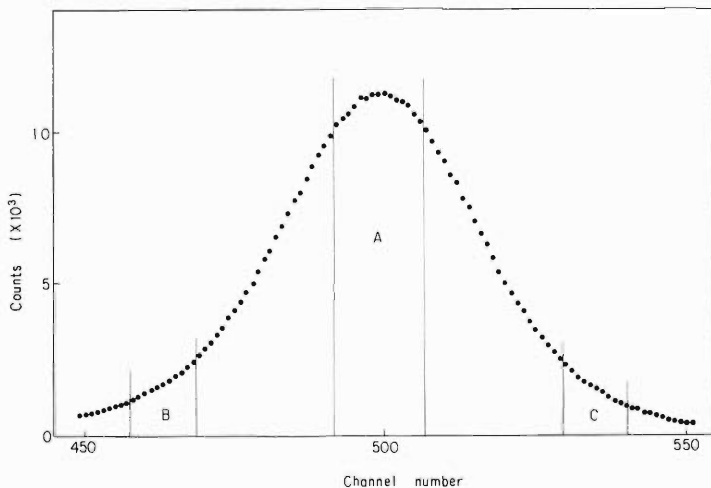
Fig. 1. The definition of S- and h-parameters. S-parameter is given by A/(B+C) and h-parameter is given by the A part devided by the area under the curve.
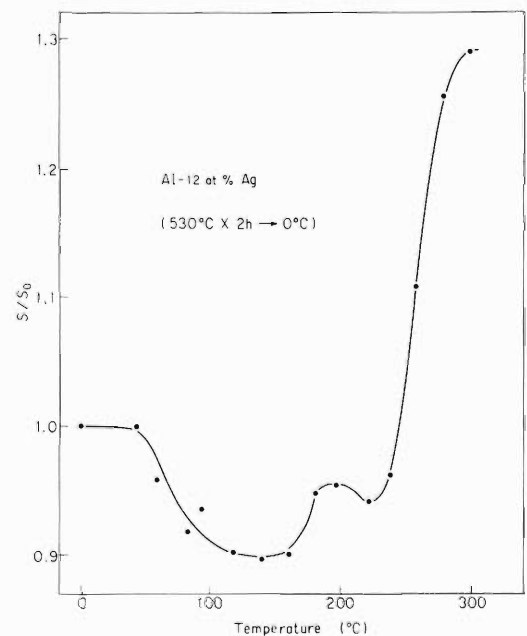
Fig. 2. The variation of S-parameter for Al-12 at.% Ag alloy as a function of isochronal annealing temperature.

* Department of Metallurgy and Materials Science, Faculty of Engineering, The University of Tokyo.

ice water. The results are shown in Fig. 3. The large hump at 160°C corresponds to the formation of α' phase. These general features are in good agreement with those of the Al-Cu system.[1]

The $Pd_{0.80}Si_{0.20}$ and $Ni_{0.81}P_{0.19}$ amorphous alloys were prepared by the usual roller squeezing and the electrodeposition methods, respectively. Figure 4 shows h-parameters as a function of temperature for the Pd-Si alloy. The definition of h-parameters is also shown in Fig. 1. The results for both alloys suggested that the amorphous state contains few vacancy-type defects in accordance with the previous results[2],[3] and that the possibility of the microcrystalline disorder structure should be excluded.
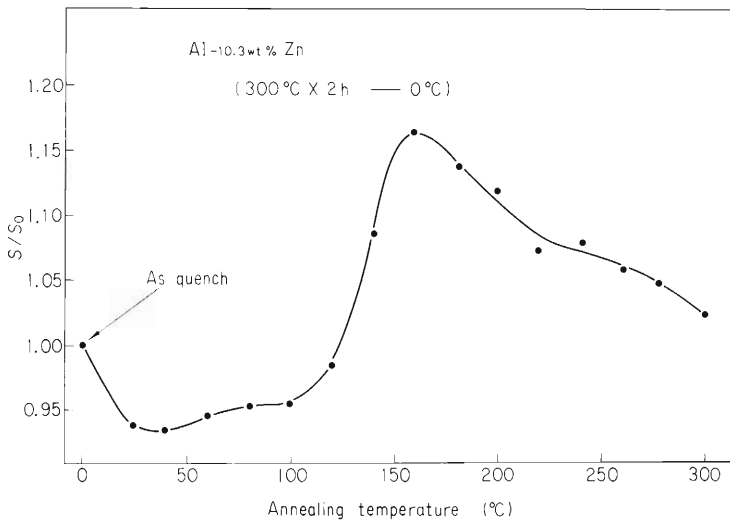
Fig. 3. The variation of S-parameter for Al-10.3 wt.% Zn alloy as a function of isochronal annealing temperature.
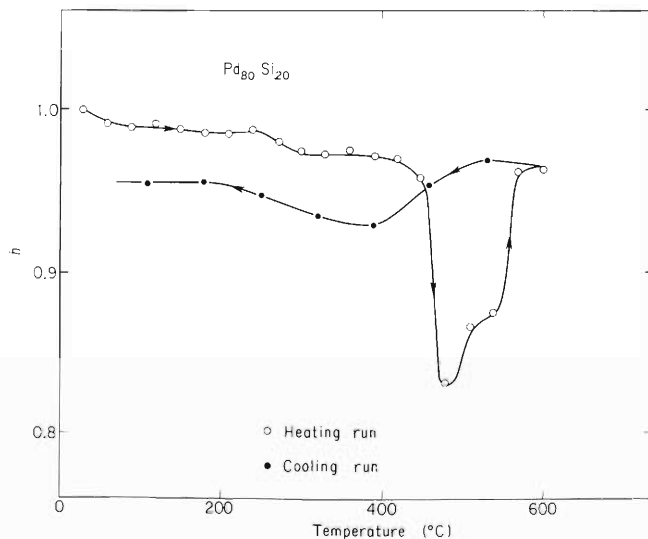
Fig. 4. The h-parameter in the $Pd_{0.80}Si_{0.20}$ amorphous alloy as a function of temperature.

References

1) R. Nagai, S. Tanigawa, and M. Doyama: Scr. Met., 10, 529 (1976).

2) H. S. Cheng and S. Y. Chaung: phys. stat. solidi (a), 25, 581 (1974).

3) M. Doyama, S. Tanigawa, K. Kuribayashi, H. Fukushima, K. Hinode, and F. Saito: J. Phys., F, 5, L230 (1975).

7-7. Positron Lifetime Measurements for Aluminum and Magnesium Using the Internal Sources Produced by Nuclear Reactions

K. Hinode,* S. Tanigawa,* M. Doyama,* and N. Shiotani

Positron lifetime measurements were carried out for high purity aluminum and magnesium. As the positron source, ^{22}Na was produced in the aluminum and the magnesium specimens themselves by the nuclear reactions ^{27}Al(^{3}He, $2\alpha)^{22}$Na and ^{24}Mg(d, $\alpha)^{22}$Na, respectively. In the case of aluminum, the thickness of the specimen was large enough to stop all the incident ^{3}He particles. A schematic drawing of the specimen is given in Fig. 1.

Figures 2 and 3 show the temperature dependences of positron mean lifetime, τ_M, for aluminum and magnesium, respectively. For aluminum, change of τ_M was well explained by the positron trapping model.[1]-[3] The evaluated value of the vacancy formation enthalpy in aluminum was 0.75eV. In the case of magnesium, change of τ_M shows no similar behavior as that observed in aluminum. Two interpretations are considered to account for this fact. One is that thermally created vacancies in magnesium cannot trap the positrons. The other is that the vacancies in magnesium can trap the positrons as in aluminum but unlike in aluminum the local electron density at the vacancies where the
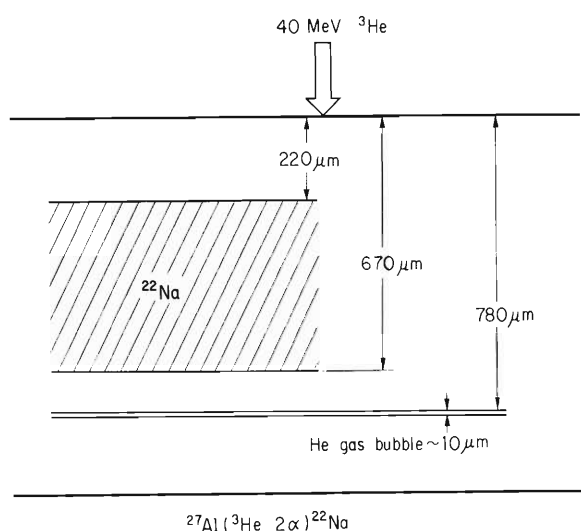

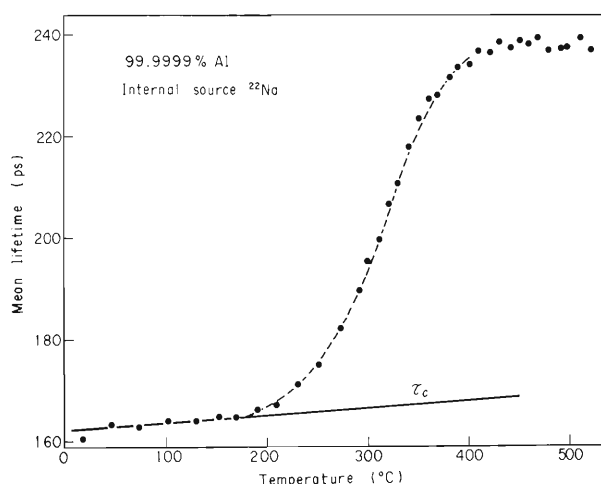Fig. 1. Schematic drawing of the aluminum specimen.

Fig. 2. Positron mean lifetime, τ_M, as a function of temperature in aluminum. Dashed line is a curve drawn to fit the experimental results on the basis of the trapping model.

* Department of Metallurgy and Materials Science, Faculty of Engineering, The University of Tokyo.

positrons are trapped is not appreciably different from the average electron density of the perfect lattice sites.

In the case of internal sources, the annihilation of positrons in the source is negligible, but there is an appreciable long-lived component in all spectra in addition to the bulk component as shown in Fig. 4. The intensity of the long-lived component is about 5 % of the total intensity. This component may have arisen from the annihilation of positrons at the He bubble region (see Fig. 1) The very long lifetime of this component (about 900ps) suggests the formation of positronium (Ps) in this region.
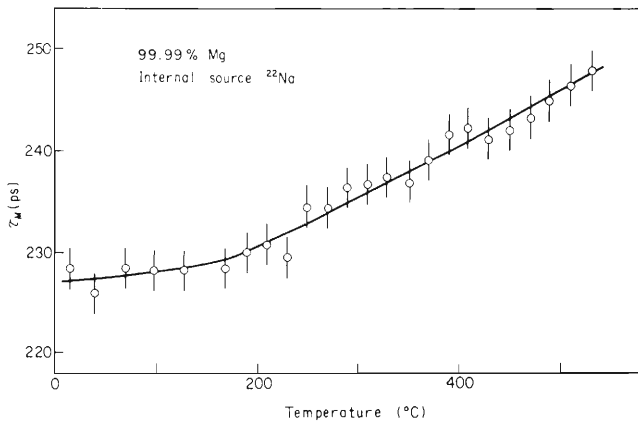
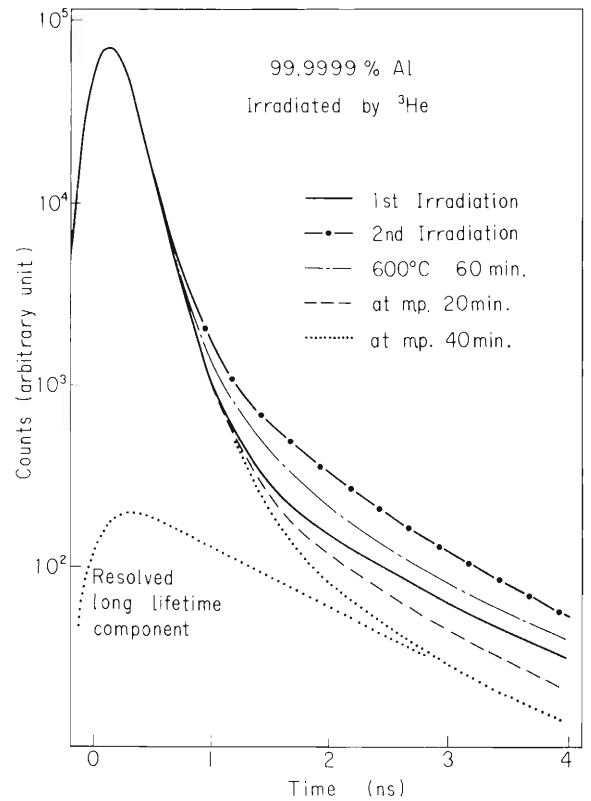Fig. 3. Positron mean lifetime, τ_M, as a function of temperature in magnesium.

Fig. 4. Positron lifetime spectra measured after various treatments for aluminum. Long-lived component can be evidently seen in each spectrum.

References

1) W. Brandt: "Positron Annihilation", Academic Press, N.Y., p. 155 (1967).

2) B. Bergersen and M. J. Stott: Solid State Commun., 7, 1203 (1969).

3) D. C. Connors and R. N. West: Phys. Let., 30A, 24 (1969).

7-8. Atomic Displacements in Metals Caused by Irradiation

H. Sakairi, E. Yagi, A. Koyama, and R. R. Hasiguti*

Many problems in the study of radiation damage of solids by energetic particles are concerned with the atomic displacement cascades. A matter of primary interest is the number of displaced atoms created by collision cascade caused by primary knocked-on atoms with the energy E_p, which is called a damage function and denoted by $\nu(E_p)$. Analytical expression giving $\nu(E_p)$ was first presented by Kinchin and Pease based on a simple model.[1] Values of $\nu(E_p)$ calculated were, however, larger than experimental ones by a factor of 4~5. Several mechanisms were presented as the origin of this discrepancy, among which a focused replacement collision sequence was considered to be the most probable mechanism.[2] The form of the damage function derived on the basis of focused replacement mechanism was presented in the previous report.[3] It was shown in that report and by other researchers[2] that the discrepancy can not be removed if only that mechanism is taken into account.

Recently Robinson and Torrens presented a new model from the analysis of their results of computer simulation.[4] In their model they took a distance criterion for permanent displacement of lattice atoms, instead of a threshold energy criterion which was adopted in the Kinchin-Pease model. In the new model, a displacement threshold energy is assumed to be very low, and the movement of all displaced atoms are followed by a computer till their energy becomes very low that they can be regarded as being at rest. Then only the cascade atoms which are separated from vacancies by a distance larger than recombination radius r_v are stabilised, and the others are annihilated by recombination with vacancies. The essential defference between these two models is that in the Kinchin-Pease model the stability of each Frenkel pairs is independent of the distribution of other pairs, while in the Robinson-Torrens model it is dependent on it.

The numerical results of the simulation by Robinson and Torrens suggests that the damage function $\nu(E_p)$ is expressed as

$$\nu(E_p) = \frac{\hat{E}}{\alpha + \beta\hat{E}} \ .$$

Here $\hat{E}$ is a quantity called the damage energy, given by

$$\hat{E} = E_p - Q \ ,$$

Q being a loss due to electron excitation in a displacement cascade, and α and β are parameters which are functions of recombination radius of Frenkel pairs, r_v. With these equations and the assumption that $r_v = 2.5a$ (a: lattice constant), they calculated the number of displaced atoms in
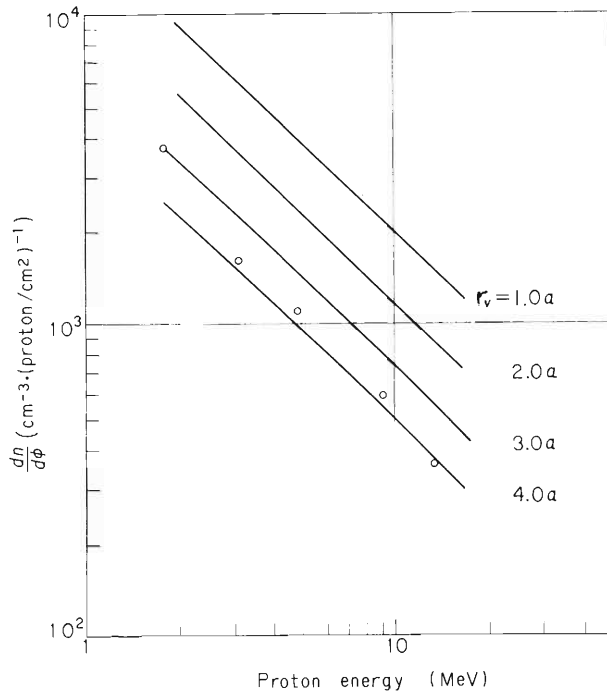
94

Fig. 1. Comparison of the calculated results and the experimental ones on the defect introducing rate in copper irradiated with protons.

copper metals irradiated with neutrons. The ratio of the calculated values to the experimental ones was 2.1 for thermal neutrons and 2.2 for fission neutrons.[5]

We calculated the same quantity for proton irradiations in the same manner and compared the results with the experimental ones obtained with the cyclotron, a part of which was reported previously.[6] The results of the calculation were expressed as a defect introducing rate, $dn/d\phi$, ϕ being the irradiation dose. The experimental results of the rate of resistivity increase, $d\rho/d\phi$, were also converted to $dn/d\phi$. Both of them are shown in Fig. 1. The experimental points fell on a calculated curve for $r_v = 4.0a$. This value of r_v is somewhat larger than the one deduced from the experimental results on the radiation annealing of the damage.[7] The value of $r_v = 2.5a$, which was assumed in the calculation by Robinson and Torrens, made the calculated values of $dn/d\phi$ twice as large as the experimental ones, as in the case of neutron irradiations.

As recognised by Robinson and Torrens themselves, their simulation has some weak points such as the lack of a molecular dynamical treatment. Nevertheless, it seems to be also a promising mechanism in removing the discrepancy between the theory and the experiment. At the present stage, it can be said that the focused collision mechanism and the recombination one make almost equal contribution to correct the damage function.

References

1) G. H. Kinchin and R. S. Pease: Rep. Prog. Phys., 18, 1 (1955).
2) M. W. Thompson: "Defects and Radiation Damage in Metals", Cambridge Univ. Press, London, Chap. 5 (1969).

3) H. Sakairi, E. Yagi, A. Koyama, and R. R. Hasiguti: IPCR Cyclotron Progr. Rep., 8, 101 (1974).

4) M. T. Robinson and I. M. Torrens: Phys. Rev., B9, 5008 (1974).

5) M. T. Robinson: Proc. Intern. Conf. "Fundamental Aspects of Radiation Damage in Metals" (Gatlinburg, 1975), USERDA: CONF-751006-P1, 1 (1975).

6) H. Sakairi, E. Yagi, A. Koyama, T. Karasawa, and R. R. Hasiguti: IPCR Cyclotron Progr. Rep., 5, 101 (1971).

7) W. Schilling, F. Burger, K. Isebeck, and H. Wenzl: "Vacancies and Interstitials in Metals" (Ed. by A. Seeger et al.), North-Holland, Amsterdam, p. 284 (1970).

7-9. Observation of Defect Structures of Slightly Reduced Rutile (TiO$_2$) by Channeling Method

E. Yagi, A. Koyama, H. Sakairi, and R. R. Hasiguti*

Stoichiometric rutile, TiO$_2$, is an insulator. Upon slight reduction it becomes an oxygendeficient non-stoichiometric rutile, TiO$_{2-x}$, which is an n-type semiconductor. It is well established that some kinds of defects introduced into rutile crystals by slight reduction give rise to the n-type semiconductivity. But the problem of whether the dominant defects introduced by slight reduction are oxygen vacancies or titanium interstitials has been in controversy, although the evidences are somewhat in favor of titanium interstitials.[1]

If titanium interstitials are dominant defects, it is to be expected that channeling experiments would give decisive information about that problem as described below. Figure 1 (a) shows a crystal structure of rutile. It has an open channel along the [001] axis. It is illustrated by dotted square in the end view of atomic arrangement for the [001] axial direction (Fig. 1 (b)). It has been proposed that a titanium interstitial is at the (1/2, 0, 1/2) type site. If this is the case, the titanium interstitial lies at the center of the [001] channel. Therefore the channeling method is directly sensitive to such interstitials.
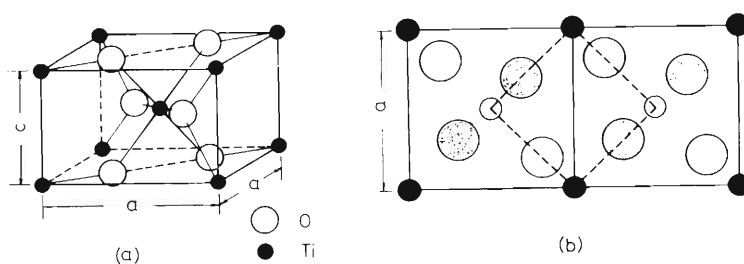

Fig. 1. (a) A unit cell of a rutile crystal. Lattice constants a=4.594Å and C=2.959Å. (b) The end view of atomic arrangement for the [001] axial direction. An open channel is indicated by a dotted square.

The stoichiometric single crystal specimen was reduced at 1100°C in vacuum of 10^{-6} mmHg for 240 h, and submitted to channeling experiments. Oxygen deficiency was estimated to be about 2 × 10^{20}/cm^3, which corresponds to x ≃ 0.0062 in TiO$_{2-x}$. After the experiments were over, the specimen was oxidized at 1100°C in air for 240 h and was submitted again to channeling experiments as the stoichiometric specimen.

Channeling effects were investigated with respect to a [001] axis by means of backscattering using 5.77MeV protons accelerated by the cyclotron. The beam was collimated to

less than 0.025°. The irradiated zone was 0.8mm² and the beam currents were about
1 nA. The backscattered protons were measured by a surface-barrier solid state detector
(FWHM ≃ 15keV) placed at a scattering angle of about 150°. Irradiation for backscattering
measurements was performed at room temperature.

In order to investigate the effect of non-stoichiometric defects, an angular scan was
performed through the [001] axis. Figures 2(a) and 2(b) indicate the normalized
backscattering yields from titanium ions at 4000Å depth as a function of the angle θ
between the incident beam direction and the [001] axis (Ti-dip) in case of TiO_2 and
TiO_{2-x}, respectively. The angular dependence of the scattering yields from oxygen ions
(O-dip) was also obtained. As to the O-dip, the normalized minimum yield χ_{min} and the
angular half-width at half-minimum $\psi_{1/2}$ have the same values 0.065 and 0.22° respectively
in both cases of TiO_2 and TiO_{2-x}. As to the Ti-dip, the half-angle $\psi_{1/2}$ has the same
value 0.29° in both cases. The striking feature is that the very sharp peak with the
half-angle ψ_p of 0.05° and with the maximum yield of 0.027 is observed at the center of
the Ti-dip in case of TiO_{2-x} and not in TiO_2. In the latter case the value of χ_{min} is 0.014.
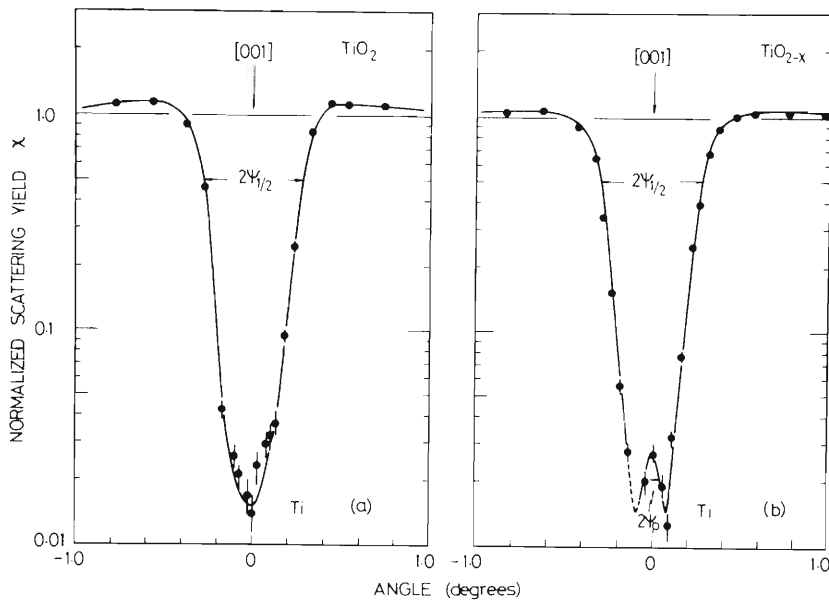

Fig. 2. Backscattering yield from titanium ions in TiO_2 (a),
and in TiO_{2-x} (b) as a function of the angle θ between the
incident beam direction and the [001] axial direction.

It is known that for incidence parallel to a major axis the probability density of
channeled beam flux attains higher values than that of random beam flux (flux-peaking
effect).[2] As a result the backscattering yield of channeled particles from interstitials in the
center of a channel can be several times greater than that of random particles. Therefore,
they are expected to give rise to a peak with the higher scattering yield than the random
yield in an angular scan of the backscattering yield. The result shown in Fig. 2(b) can be
interpreted as superposition of a dip obtained with respect to titanium ions at normal
lattice sites and a peak obtained with respect to titanium interstitials. The observed small

peak was explained well quantitatively on the assumption that all of excess titanium ions in TiO_{2-x} become interstitials.

By the analysis of this peak it was confirmed that main defects in a slightly reduced rutile are titanium interstitial ions and they are located within $0.4\overset{\circ}{A}$ of the [001] mid-channel axis. This result supports the interpretation of electron paramagnetic resonance (EPR) experiments that a so-called C-center is a titanium interstitial ion.[1] The effect of radiation damage by protons was also investigated on a stoichiometric specimen. The damage production rate of Frenkel pairs for titanium ions at room temperature was estimated to be about $4.4 \times 10^{-20}/(p/cm^2)$ in atomic fraction.

References

1) R. R. Hasiguti: Ann. Rev. Mater. Sci., 2, 69 (1972).

2) J. U. Andersen, O. Andreasen, J. A. Davies, and E. Uggerhøj: Rad. Effects, 7, 25 (1971).

7-10. Perturbed Angular Correlation of Gamma-Rays Emitted from ^{111}Cd in NiFe$_2$O$_4$

H. Sekizawa, K. Asai, T. Okada,

N. Shiotani, E. Yagi, and S. Ambe

It is well known that to account for the magnetic properties of materials containing transition metal ions one must know the cation-cation interactions. In contrast to transition metal ions, nominally diamagnetic cations have no unpaired electrons by themselves, so that the hyperfine magnetic fields in them reflect directly the interactions with neighboring magnetic ions.

In this report we present experimental data on the time differential perturbed angular correlation (PAC) of γ-rays emitted from ^{111}Cd in NiFe$_2$O$_4$ and then discuss the hyperfine magnetic field on ^{111}Cd nuclei in NiFe$_2$O$_4$ at room temperature.

The sample was prepared by nitric acid method. We dissolved pure Ni and Fe metal powder in nitric acid and added ^{111}In chloride to the solution. The solution was dried, and then the residue was ground and fired for 2 h in air. The sample was packed in an acrylate tube 4mm in diameter and 8mm long. The spectra were taken with a conventional fast-slow two detector set up. Two NaI(Tl) scintillation counters were used as the detectors. An external magnetic field was applied perpendicular to the plane of the two counters. The magnitude of the magnetic field was 3800 oe, which was sufficient to saturate the magnetization of NiFe$_2$O$_4$.

The general expression for the time differential angular correlation function perturbed by a perpendicular magnetic field H is

$$W(\vartheta, t) \propto \exp(-t/\tau) \left[1 + \sum_{k \text{ even}} A_{kk} P_k \left\{\cos(\vartheta - \omega_m t)\right\}\right] . \tag{1}$$

where θ denotes the angle between the two γ-rays, t is the time interval between the two cascade γ-rays, τ is the life time of the intermediate Cd(5/2$^+$) state and ω_m is the Larmor frequency. Since factor A_{kk} for $k \geqq 4$ is much smaller than A_{22}, the coincidence counts are modulated with opposite phase for θ=90° and 180°. We define the normalized difference in the coincidence counting rates as follows.

$$R(t) = \frac{W(90, t) - W(180, t)}{W(90, t) + W(180, t)} = \frac{(3/4)A_{22} + (5/16)A_{44}}{1 + (1/4)A_{22} + (9/6)A_{44}} \cos 2\omega_m t \quad \ldots \ldots \tag{2}$$

Figure 1 shows the coincidence counts for θ=90° and 180° after substracting accindental coincidence counts which are calculated from the γ-ray intensity.

R(t) showed an oscillation whose amplitude decreased as the time increased. The decrease of the amplitude can be ascribed to a distribution of the hyperfine magnetic field of ^{111}Cd. If we assume a gaussian distribution of the field $f(H) \propto \exp[-(H-H_0)^2/(\sqrt{2}\Delta H)^2]$, the normalized
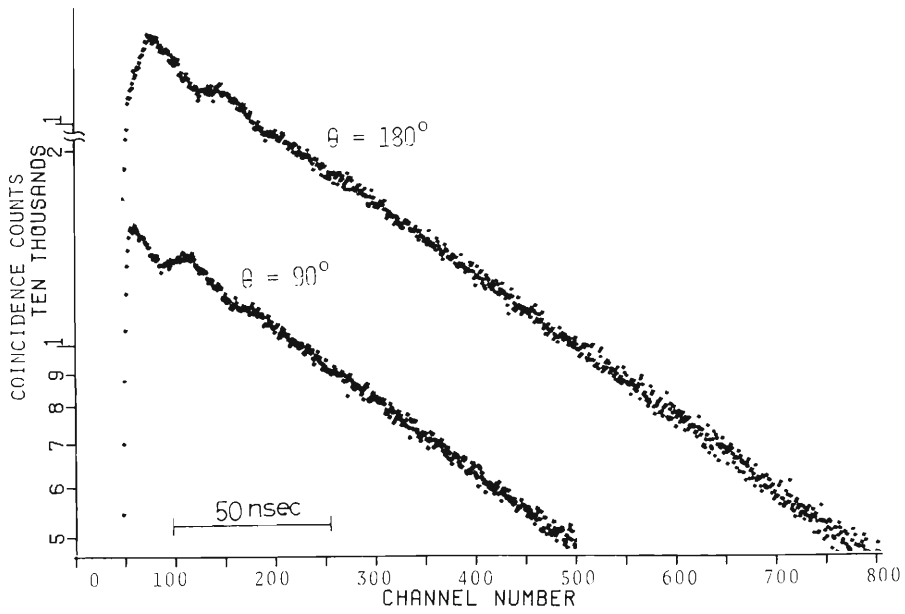
Fig. 1. Coincidence counts of γ-rays from ^{111}Cd in $NiFe_2O_4$ with an external polarizing field of 3.8kOe applied perpendicular to the axis of the two detectors. The data at $\theta=180°$ is shifted vertically for the sake of clarity.

difference in coincidence counting rate R(t) becomes as follows:

$$R(t) \propto \exp[(\sqrt{2}\triangle\omega\cdot t)^2] \, \cos2\omega_0 t \quad \ldots \ldots \ldots \ldots \ldots \quad (3)$$

where $\triangle\omega=\gamma\triangle H$, $\omega_0=\gamma H_0$, and γ is the gyromagnetic ratio of $5/2^+$ state of ^{111}Cd nucleus. We tried a computer fitting of the experimental data, based on the above assumption. The fitted curve is shown in Fig. 2. The value of H_0 was found to be 93kOe and $\triangle H$ to be 17kOe at room
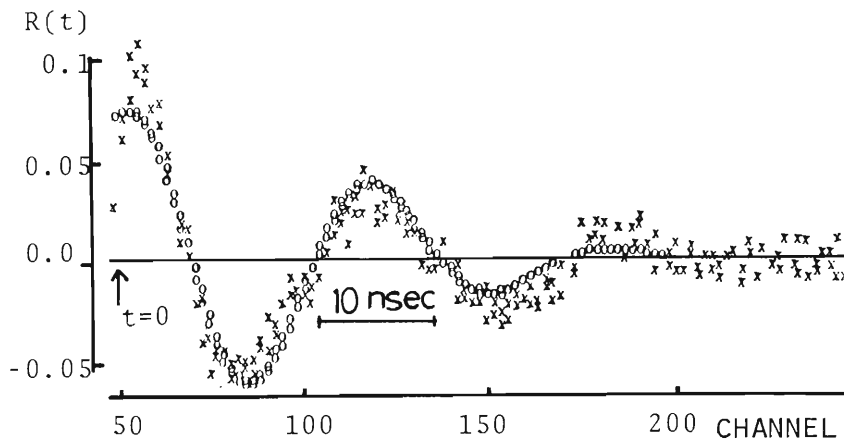
Fig. 2. The normalized difference in the coincidence counting rates R(t). The experimental data are shown by the symbol X, and the computer fits of Eqn. (3) by o.
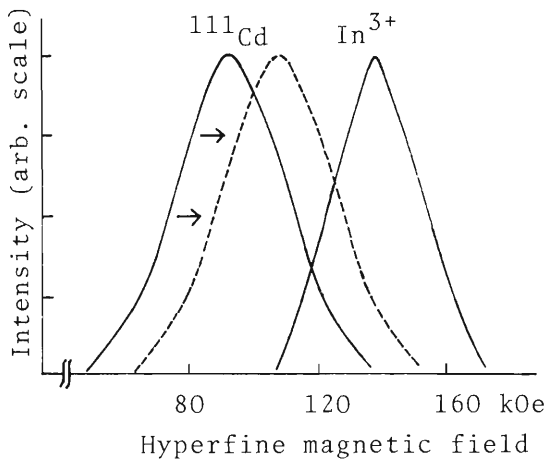
Fig. 3. The hyperfine field of diamagnetic ions at A site in $NiFe_2O_4$. The data on In^{3+} are the NMR data at 4.2K quoted from Ref. 1. For Cd ion the solid line is the spectrum at room temperature, and the dotted line is shifted based on the assumption that the hyperfine magnetic field of Cd ion is proportional to the saturation moment of $NiFe_2O_4$.

temperature. If we assume that the hyperfine magnetic field of Cd ion is proportional to the saturation magnetization of $NiFe_2O_4$, H_0 will be 108kOe at OK. Figure 2 shows the normalized difference in the coincidence counting rates R(t). To know the direction of the hyperfine magnetic field, we took the spectra at $\theta=135°$. This result indicates that the hyperfine magnetic field is parallel to the net magnetization.

In^{3+} seems to occupy preferentially the tetragonal (A) site (80%) according to the magnetization data.[1] Therefore, the daughter nucleus ^{111}Cd is in the tetrahedral site. Figure 3 shows the hyperfine magnetic field of Cd ion (our data) and that of In^{3+}.[1] Thus, the direction of the field of Cd ion is the same as that of In^{3+}, but the magnitude of the field of Cd ion is a little smaller than that of In^{3+}.

It would be necessary for a full discussion to consider the effect of the preceeding decay of ^{111}In carefully, and also to investigate the spectra at lower temperature.

Reference

1) Y. Miyahara and S. Iida: J. Phys. Soc. Japan, 37, 1248 (1974).

7-11. Nitrogen Ion Implantation in CdTe for Optical Waveguides and Waveguide-type Electrooptic Modulators

T. Nishimura, H. Aritome, K. Masuda,

S. Namba, and I. Kohno

CdTe has a higher electrooptic coefficient and a lower attenuation coefficient in the infrared region than GaAs, and is the only material among II-VI compound semiconductors from which p-n junction can be obtained. From these points CdTe is one of the most interesting materials for optical integrated circuits in the infrared region.

H^+ ion implantation into low-resistive CdTe can produce a thin compensated layer of free carriers in the substrate. The ion implanted region, which has a much smaller free carrier concentration than the substrate, has a higher refractive index than that of the substrate. Optical waveguides and waveguide type electrooptic modulators using CdTe could be fabricated in this manner, and were reported recently.[1],[2] Further improvement in the optical absorption loss and the efficiency of electrooptic modulation however, is important for practical use. If the carrier compensation in the thin layer can be done by chemical doping and the lattice damage induced by ion implantation can be removed, low absorption loss and high efficiency of the electrooptic modulation will be expected. The layer thickness can be easily controlled by the ion energy. From these points, nitrogen ion was chosen because it has the possibility of being the p-type dopant having the maximum penetration depth in CdTe. The cyclotron was used to accelerate nitrogen ion to have penetration depth enough for optical waveguiding in CdTe.

As a preliminary study chemically polished <001> oriented n-type CdTe wafers with carrier concentration of 9.8×10^{17} /cm^3 were ion implanted at 80 MeV with a dose of 1×10^{15} nitrogens/cm^2.

In order to measure the electrooptic coefficient, a gold electrode was deposited on an ion implanted layer and an indium electrode was deposited on the other side of the substrate. The sample was placed between crossed polarizers and the transmittance was measured as a function of applied voltage. But the voltage enough for measuring the change of the optical output could not be applied because considerable current flowed through the ion implanted layer of the sample. The reason is not understood at present why the carrier compensation is not enough for production of the high resistive layer. It is not so far successful to measure the electro optical properties in the sample implanted by nitrogen ion. The study of the annealing behavior is now in progress to understand these results.

References

1) D. L. Spears, A. J. Strauss, S. R. Chinn, I. Melngailis, and P. Vohl: Digest of the Topical Meeting on Integrated Optics (Optical Society of America, Salt Lake City, 1976), TuD 3.

2) T. Nishimura, H. Aritome, K. Masuda, and S. Namba: Japan. J. appl. Phys., 15, 2283 (1976).

104

7-12. Helium Embrittlement of CTR Materials Simulated by Alpha Particle Bombardment

R. Watanabe,* H. Shiraishi, H. Shinno,

H. Kamitsubo, I. Kohno, and T. Shikata

Investigation of the mechanical properties of metallic structural materials irradiated by fast neutrons is urgently needed for the design of the controlled thermonuclear reactor. Fast neutron causes embrittlement of metals. The embrittlement is thought to be due to cascades of displaced atoms caused by various kinds of collisions and due to helium atoms created by (n, α) reactions. But the details of the mechanism of the embrittlement has not yet been clarified.

The aim of this study is to develope new structural metals and alloys which are highly resistant to neutron irradiation embrittlement. Neutron irradiation experiments is extremely expensive and time consuming. In contrast, α-particle injection study by the cyclotron for the simulation of fast neutron irradiation damage is much easier and also considered to be applicable for estimating one of the aspects of the degradation phenomena of materials caused by neutron irradiation. With regard to helium embrittlement, such phenomena as helium diffusion, change of the helium distribution profile in the specimen, and helium release from the specimen will be studied.

We constructed a new target chamber as shown in Fig. 1. This apparatus is characterized by the following specifications.

1) The sample is heated and held at a certain constant temperature which can be as high as 1000°C during the α-particle bombardment. The vacuum is maintained at 2×10^{-6} Torr at
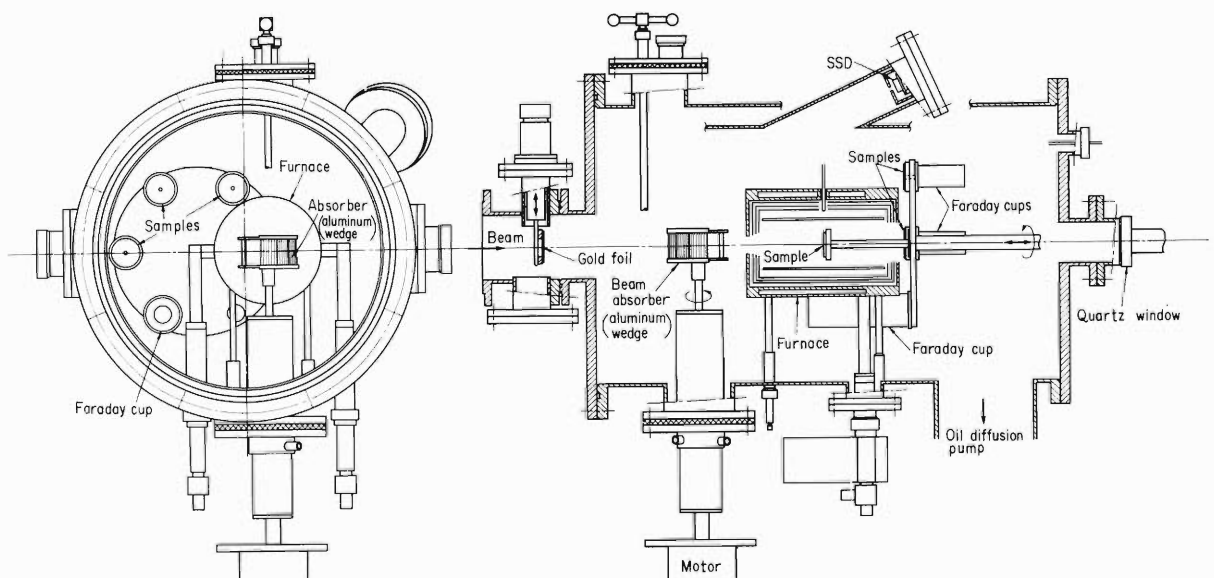

Fig. 1. Schematic illustration of the target chamber for helium injection by the cyclotron.

1000°C.

2)   A cylindrical frame structure on the side of which six wedge type aluminum plates are stuck along half of the circumference is driven to rotate in front of the target. The injected helium atoms are uniformly distributed in the direction of the sample thickness. The maximum rotation speed of the absorber drum is 1000 rpm. The time required to oscillate the beam from surface to bottom of the specimen can be reduced to 10^{-2} sec. This value is shorter by two to three orders of magnitude than that obtained in the usual wedge and piston movement type absorber system. The rotating axis of the beam absorber is coupled to the outer drive motor through the oil seal device.

3)   Following beam current measuring system is employed to avoid the disturbance by the thermal electron ejection. The total α-particle beam is transmitted through a thin gold foil 10 μm thick and the scattered beam is continuously monitored by a solid state detector. At the same time, the transmitted beam is measured by the Faraday cup and the ratio of the scattered to the transmitted beam is determined. This ratio is used for the determination of the helium injection dose of the sample.

The preliminary operation test of various components is now under way. The α-particle bombardment of samples will be started at the beginning of 1977.

8. RADIOCHEMISTRY AND NUCLER CHEMISTRY

8-1. Charge and Mass Spectra of Ions Occurring along the α-Particle Tracks in Mica

M. Aratani

Ions sputtered from aluminosilicate mica have been investigated under bombardment with α-particles from an ^{241}Am source (500 μCi, 1 cm $\times$ 1 cm) in a charge spectrometer[1] and with 10 KeV He$^+$ ions in an ion probe mass spectrometer.[2] In the α-bombardment the source was placed in close contact behind mica foils of various thicknesses in order to study ions originating from various points on the α-tracks. The 10 KeV He$^+$ ion was expected to give information quite similar with that α-particle gave at its stopping point.

Also, the change in sputtered ion intensity with time in the ion probe mass spectrometer was measured for the same matrix which had been bombarded with the ^{241}Am source for one month.

Intensity ratios of silicon ions with various charge states are given in Table 1 and those of various ions in Table 2, where R_a is the range of ^{241}Am α-particle. In the case of $0.36R_a$ and

Table 1. The intensity ratios of Si^{n+} ions from various points along the α-particle tracks in mica.

Thickness of mica	Ions		
	ΣSi^+	ΣSi^{2+}	ΣSi^{3+}
0*	—	—	—
$0.36R_a$**	1.0	0.3	0.1
$0.48R_a$**	1.0	0.3	0.1
$\simeq R_a$***	1.0	1.8×10^{-3}	1.4×10^{-4}
$1.2R_a$	0	0	0

* Data could not be obtained because of the presence of recoil ions from ^{241}Am.

** See text.

*** The values are those of $^{28}Si^{n+}$ ions only.

0.48R$_a$, where 6 μm and 8 μm mica foils were used respectively, α-particles with lower energies than the maximum energy at the surface of the mica foil and were responsible for the sputtering of ions in the present experimental condition. The values in Table 2 have already been corrected by considering the atomic percentage of each element in the mica foils. The values, therefore, give removability of matrix atoms as free ions.

As is shown in Table 1, multicharged ions are less abundant at all points observed, especially in the neighborhood of the stopping point. Table 2 shows that potassium ion has predominant removability from the matrix, which can be attributed to its site in mica. Complicated behaviors of aluminium ion and aluminium oxide ion may be related to the two kinds of aluminium sites, tetrahedral and octahedral, in mica.

The results obtained on post effect of the one month α-bombardment are illustrated in Fig. 1. The abscissa represents time of peeling, accordingly the peeled depth, by a 2 KeV Ar$^+$ ion beam impinging on the surface of the damaged mica. The ordinate indicates the sputtered ion intensity relative to that from the surface of mica without damage. Energy and current density of ion beam were kept constant and as low as possible in order to be free from giving any disturbance to the sample. The change in the sputtered ion intensity with time suggests that there should exist some differences in the matrix state with the depth. The gradual decreases seen in Fig. 1 lead us to the conclusion that there are matrix portions near the surface giving high intensities of sputtered ions, but those portions gradually disappear with the depth. The high intensity of sputtered ion can be attributed to the existence of latent tracks, consequently the damaged parts. Further analysis of the sputtered ion intensity curve may offer more interesting information about the post effect in the particle tracks.

Table 2. The intensity ratios of ions from various points along the
α-particle tracks in mica.

Thickness of mica	Ions					
	ΣSiO^+	ΣAlO^+	ΣK^+	ΣSi^+	Al^+	ΣO^+
0*	—	—	—	—	—	—
0.36R$_a$**	0	1.2	13	1.0	0.8	0.05
0.48R$_a$**	0	1.2	12	1.0	0.8	0.03
$\simeq$R$_a$***	0.005	0.002	8.1	1.0	3.4	0.09
1.2R$_a$	0	0	0	0	0	0

* See Table 1.

** See Table 1.

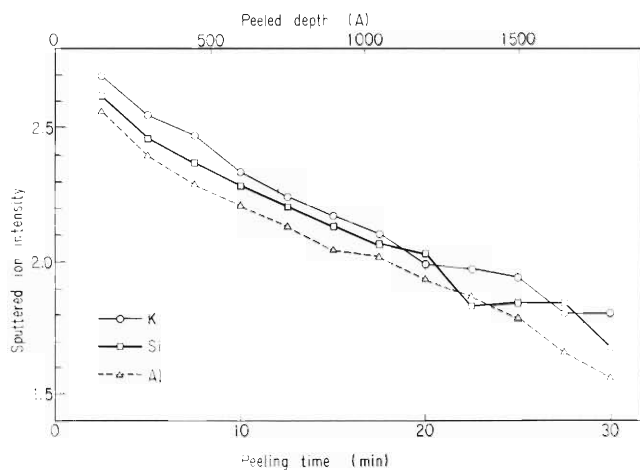*** The values are those of [44](SiO)$^+$, [43](AlO)$^+$, [39]K$^+$, [28]Si$^+$, and [16]O$^+$, respectively.

Fig. 1. The change in sputtered ion intensities* with peeling time from the surface of the damaged mica by the preceding α-bombardment.

* The values are relative to those of sputtered ion intensities from the surface of mica without damage.

References

1) Y. Kawana and M. Aratani: Int. J. Mass Spectrom. Ion Phys., 10, 493 (1973); M. Aratani, K. Nakamura, and N. Saito: Mass Spectroscopy, 23, 315 (1975).

2) K. Nakamura, S. Aoki, Y. Nakajima, H. Doi, and H. Tamura: ibid., 20, 1 (1972).

8-2. Mössbauer Emission Studies of Defect Atoms in Solid after Nuclear Decays and Reactions

F. Ambe and S. Ambe

The behavior of ^{119}Sb and ^{119m}Te contained as dilute impurity atoms on recrystallization of p- or α-irradiated SnTe and SnSb was studied and the results were compared with those for the recoil atoms formed by p- and α-reactions.[1)-4)]

The ^{120}SnTe samples irradiated with 15 MeV protons were melted and recrystallized under argon, and their ^{119}Sn Mössbauer emission spectra were measured against a $BaSnO_3$ absorber at 78K.

As can be seen in Fig. 1, the emission spectra showed a marked dependence on the composition of the sample. On the basis of a systematics of the isomer shift for defect and normal ^{119}Sn atoms in Sn-Sb-Te system[1),4)] the peaks with an isomer shift of about 2.3 mm/s were attributed to ^{119}Sn in the Te site of ^{120}SnTe and the other peaks with an isomer shift of
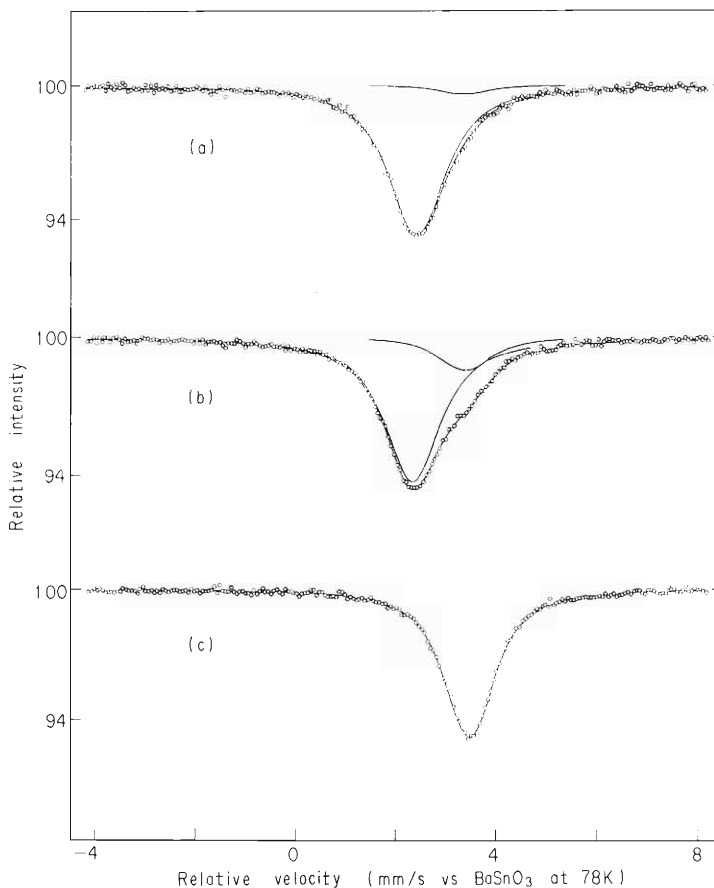
Fig. 1. ^{119}Sn-Mössbauer emission spectra of
(a) ^{120}SnTe$_{0.97}$, (b)^{120}SnTe, and (c) ^{120}SnTe$_{1.03}$
which had been irradiated with protons, melted,
and recrystallized.

approximately 3.4 mm/s to those in the Sn site. Since no displacement of the atom is expected in the EC decay of ^{119}Sb to ^{119}Sn,[3),4)] it can be concluded from the present observation that the impurity ^{119}Sb atoms are distributed between the Sn and Te sites in the stoichiometric ^{120}SnTe samples, and that in non-stoichiometric samples the ^{119}Sb atoms are distributed preferentially in the site of deficient element. These results are reasonably interpreted in terms of the fact that Sb has an electronegativity lying between Sn and Te.

By comparing the present results with those for recoil ^{119}Sb atoms after p-reaction, it can also be concluded that no melting of the SnTe matrix occurred along the track of the recoil ^{119}Sb, because the distribution of ^{119}Sb after melting is much different from that of recoil ^{119}Sb atoms.

Similar measurements on ^{119m}Te was also carried out using α-irradiated ^{117}SnSb. An emission spectrum of ^{119}Sn arising from the successive EC decays, ^{119m}Te $\xrightarrow{EC}$ ^{119}Sb $\xrightarrow{EC}$ ^{119}Sn, in a recrystallized ^{117}SnSb sample is shown in Fig. 2. The emission line is attributed to ^{119}Sn atoms in the Sb site from its isomer shift, which shows that the ^{119}Sb atoms arising from ^{119m}Te in the recrystallized samples are exclusively stabilized in the Sb site of the matrix. This finding is again interpreted in terms of the electronegativity sequence of Sn, Sb and Te.
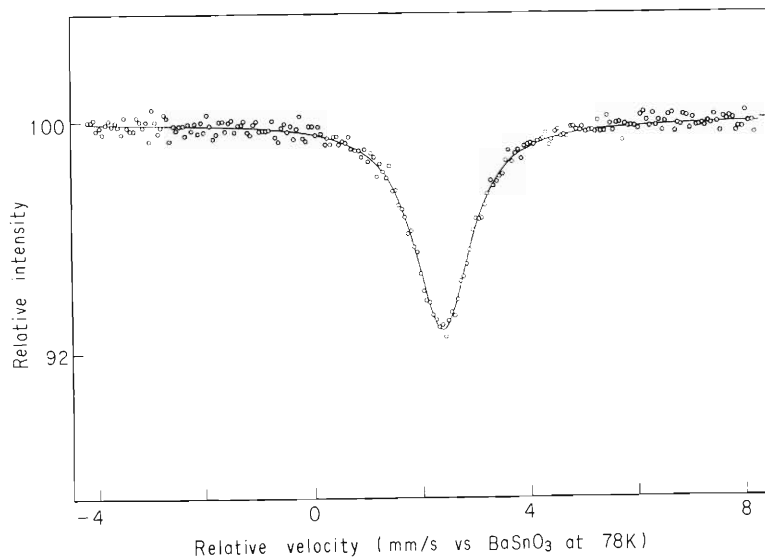
Fig. 2. ^{119}Sn-Mössbauer emission spectra of ^{117}SnSb irradiated with α-particles, melted, and recrystallized.

References

1) F. Ambe and S. Ambe: IPCR Cyclotron Progr. Rep., 8, 108 (1974).

2) F. Ambe and S. Ambe: ibid., 9, 89 (1975).

3) F. Ambe and S. Ambe: Chem. Phys. Lett., 39, 294 (1976).

4) F. Ambe and S. Ambe: J. Physique, in press.

9. RADIATION CHEMISTRY AND RADIATION BIOLOGY

9-1. Isomerization of cis-2-Butene Induced by Heavy-Ion Irradiation

Y. Harata, M. Matsui, and M. Imamura

Isomerization of cis-2-butene to trans-form by C- and N-ion irradiation was studied in benzene solution at room temperature. Photochemical and radiation chemical studies on the cis-trans isomerization of olefinic compounds including 2-butene have been the subject of numerous papers. Most of the results have been interpreted as indicating the pathways in which electronically excited states participate. In radiolysis, ionic mechanisms have occasionally been proposed for isomerization of stilbene and 2-butene.

The investigation here reported was motivated by the desire to determin whether excited states might play an important role in the heavy-ion radiolysis more than in γ radiolysis. In fact, the yields of trans-2-butene, G(t), were found to be as low (2 – 3) as that observed for γ-irradiation (∼ 2) under relatively high dose (>10^{18} eV) conditions. Heavy-ion-induced isomerization may, therefore, be considered to proceed via excited-state pathways as in the case of γ-irradiation under these conditions.

We have found, however, that G(t) increases steeply with decreasing heavy-ion dose and reaches a value of the order of 10^3. The high G(t) value, somewhat higher than that for heavy-ion irradiation, was also observed for γ-irradiation under similar conditions.

Unexpectedly and abnormally high yields of trans-2-butene at low radiation doses may be interpreted in terms of chain reaction in which cationic species participate; the important role of cation radicals of cis- and trans-2-butene was admittedly proved from a series of scavenging experiments.

The present study gives important insight not only into the primary processes in heavy-ion radiolysis but also into the kinetic behavior of positive holes produced primarily in liquid benzene. Extensive studies on both γ and heavy-ion radiolyses are in progress and the details will be published.

9-2. Emission and Absorption Spectra of KBr Irradiated with Heavy Ions at 4.2 K

K. Kimura and M. Imamura

Emission and absorption spectra were measured at 4.2 K with a single crystal of KBr irradiated with He-, C-, and N-ions. Set-up of the measurements is shown in Fig. 1. These results were compared with those obtained by X-irradiation.

Emission bands observed with X-irradiated KBr are a σ-emission at 280 nm and π-emission at 510 nm, which are attributed to relaxed excitons, $^1\Sigma_u$ and $^3\Sigma_u$, respectively. The F and H centers are formed directly from hot excitons.
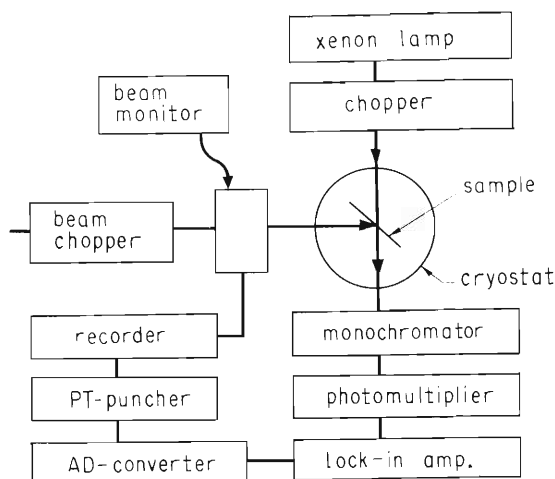
Fig. 1. Set-up for the measurements of emission and absorption spectra at 4.2 K.
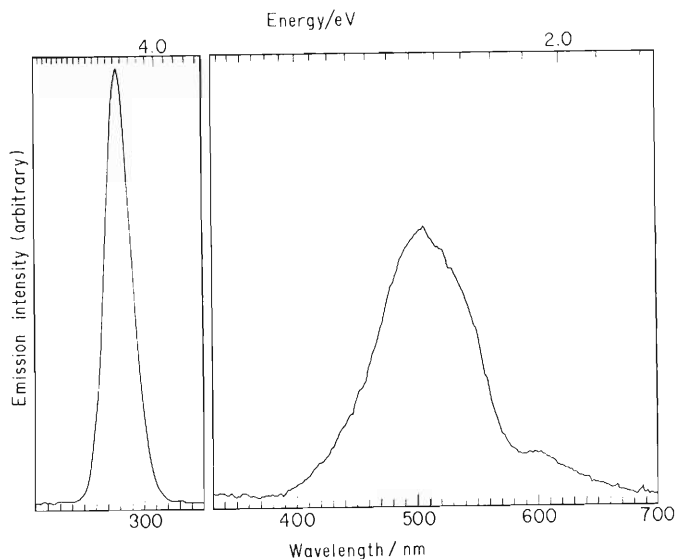
Fig. 2. Emission spectrum of KBr at 4.2 K under irradiation of 85 MeV, 1-nA C-ions. Intensity scale of the right-hand spectrum is expanded by 5 times.
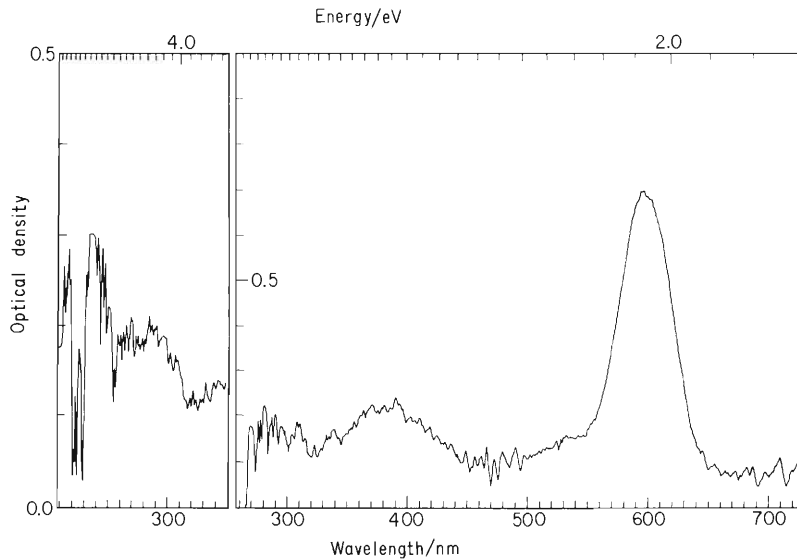
Fig. 3. Absorption spectrum of KBr at 4.2 K recorded
immediately after irradiation of 85 MeV, 1-nA C-ions.

Figure 2 shows an emission spectrum observed on heavy-ion irradiation at relatively low dose and dose rate. Significant features revealed by comparing these results with that of X-irradiation are: (1) An intensity ratio of the σ- to π- emission increases with increasing LET: 2.1 for X-rays, 6 − 7 for He-ions, and 10 − 12 for C-ions; (2) A half width of the π-emission band broadens with increasing LET: 0.41 for X-rays, 0.44 for He-ions, and 0.51 for C-ions; (3) A Peak wavelength of the π-emission band shifts to shorter wavelengths with increasing LET and radiation dose.

Figure 3 shows the absorption spectra recorded at 4.2 K immediately after C-ion irradiation. Absorption bands centered at 600 and 380 nm are attributable to the F and H centers, respectively. A 285 nm band is characteristic to heavy-ion irradiation, attributable to the H' center, the dimeric H center. A 530 nm band, which also appears in X-irradiation, has not been assigned. Intensities of these absorptions increase linearly with increasing dose except for the H center whose intensity tends to saturate.

These results may be interpreted as due to the high density of the intermediates produced with high-LET heavy-ion beams. We have assumed the reactions of the longer-lived $^3\Sigma_u$ exciton with each other and/or with the F, H, and H' centers, which result in the decrease in the emission intensity and the band-width broadening. The H' center formation and the saturation of the H center with increasing dose may be accounted for by the reaction, H + H → H', and by decomposition of the H center with $^3\Sigma_u$ exciton.

9-3.   Influence of Air Layer in Front of Samples on the Inactivation of Phage ϕX174 by Cyclotron Beam

F. Yatagai, S. Kitayama, T. Takahashi, and A. Matsuyama

Various effects of high-LET radiations on biological materials have been investigated by many workers. Such biological effects include at least two different events; one is the event occurred within the track core and the other is that induced by δ-rays at points far from the track core. When there is an air layer in front of the sample, some fraction of δ-rays scattered by the air layer also reaches the target. Contribution of such δ-rays will make obscure the observations of characteristic biological effects due to the irradiation by the high-LET particles.

In order to study this problem, inactivation of phage ϕX174 which is of single-hit kinetics has been studied. The high-LET radiations used were α-particles and N-ions of 1.2 and 4.6 MeV/amu.

The experiment was carried out using two different irradiation methods as shown in Fig. 1. Figure 1(a) shows the method in which the sample on a polycarbonate film (5 μm in thickness) is covered with the same type of film in order to eliminate the influence of air layer in front of the sample (method CF). Figure 1(b) shows the method in which the sample on the polycarbonate film is exposed to air (method EA).

(a) Covered with polycarbonate film (CF)

Vuccum window   Samples   Paper pad

beam

Polycarbonate film (thickness, 5μm)

(b) Exposure to air layer before samples (EA)
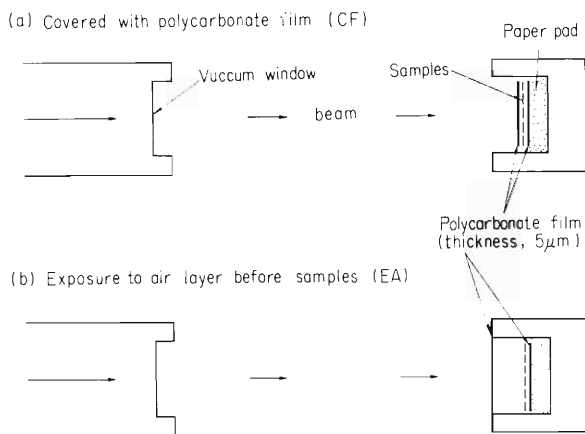
Fig. 1.   Irradiation method; samples are covered with a polycarbonate film (a), and they are exposed to air (b), see text.

In method EA, another polycarbonate film is placed at about 2 mm before the sample so that the beam energy at the sample may be equal to that in method CF. Method CF can be considered a good approximation to the case of irradiation of biological samples in water since the highest energy of secondary electrons in our experiment is about 10 keV and the range of the electron is about 2.4 μm in water. Other procedures of cyclotron-beam irradiation and dosimetry were already described.[1]   Survivals after irradiation were measured by the plaque-forming ability of ϕX174.

Survival curves somewhat concave upward were obtained after irradiation by α-particles and N-ions as shown in Fig. 2. The simple target theory is inapplicapable to these cases, but the target concept in broad sense may still be relevant. Therefore, effective inactivation cross section,

S_{eff} was calculated from D_{10} value in order to express the effectiveness per particle. As can be seen in Table 1, values of S_{eff} for EA samples were found to be higher than those for CF samples even in low energy α-particles and N-ions.

The result obtained shows that the lethal effect on φX174 is enhanced by secondary electrons ejected from the track core of α-particles and N-ions passing through the air layer in front of the sample.
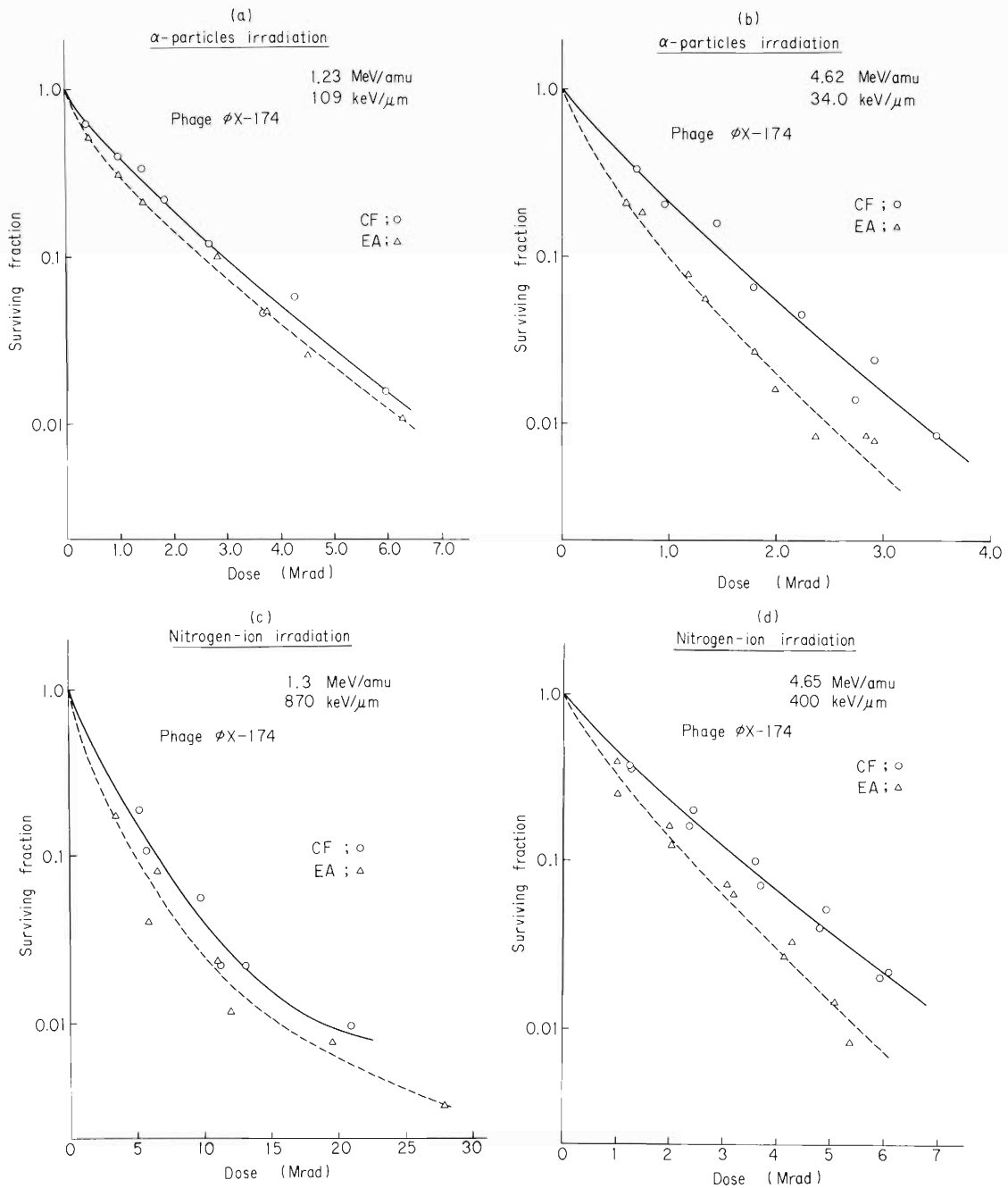

Fig. 2. Survival curves of phage φ X 174 for 1.23 MeV/amu α-particles (a),
4.62 MeV/amu α-particles (b), 1.3 MeV/amu N-ions (c), and 4.65 MeV/amu N-ions (d).

Reference

1) F. Yatagai, T. Takahashi, Y. Kitajima, and A. Matsuyama: J. Radiat. Res., 15, 90 (1974).

Table 1. Radiosensitivity of phage ϕX1974.

Particles	a-particles		N-ions	
	4.62 MeV/amu	1.23 MeV/amu	4.65 MeV/amu	1.3 MeV/amu
	34 keV/μm	109 keV/μm	400 keV/μm	870 keV/μm
$S_{eff}(\mu m^2)$ CF	8.36×10^{-4} [1.70]	1.36×10^{-3} [2.77]	4.37×10^{-3} [8.90]	4.94×10^{-3} [10.1]
$[S_{eff}/S_0]$ EA	1.25×10^{-3} [2.55]	1.59×10^{-3} [3.24]	6.10×10^{-3} [12.4]	6.54×10^{-3} [13.3]

9-4. The Effects of Cyclotron Beams on Survival of Cultured Chenease Humster Cell V-79

Y. Yamawaki,* F. Yatagai, I. Kaneko,
K. Sakamoto, S. Okada, and A. Matsuyama

In view of the current interest in high-LET radiations in radiation therapy, some fundamental cellular studies were initiated by use of the cyclotron beams. Heavy-ion beams have been reported to show several biological and physical features, i.e., comparatively high relative biological effectiveness (RBE) value compaired with that for X- or γ-rays, the dose depth characteristics, no oxygen effect and no recovery of the Elkind-type in the tissues. It seems likely that because these characteristics, heavy ion irradiation is more feasible in therapy for inactivation of tumour tissues as compared with X- or γ-rays.

Our program in the first year was to solve several technical problems which do not arise in X- or γ-ray experiments. When we irradiate the cultured Chinease hamster cells by the cyclotron beams, it is necessary to give them a very small dose of 100 – 1000 rad. Therefore, in the dosimetry system, two sets of the detector of silicon surface barrier type were used for counting very small number of particles elastically scattered by a thin metallic foil (Fig. 1.(a) and (b)). Moreover, using a mechanical chopper, number of particles passing through the vacuum was
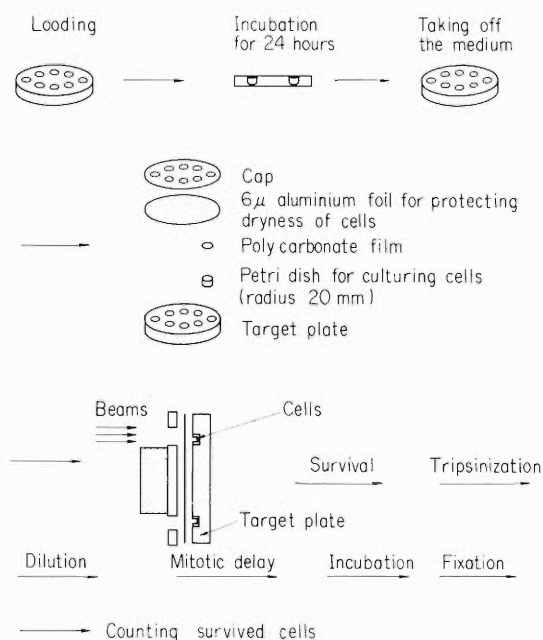
Fig. 1(a) Schematic representation of cell-handling procedures.
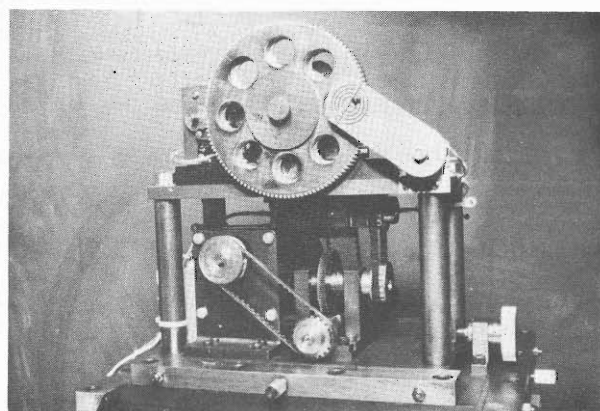
Fig. 1(b) Photograph of exposure apparatus. Petri dishes are in place.
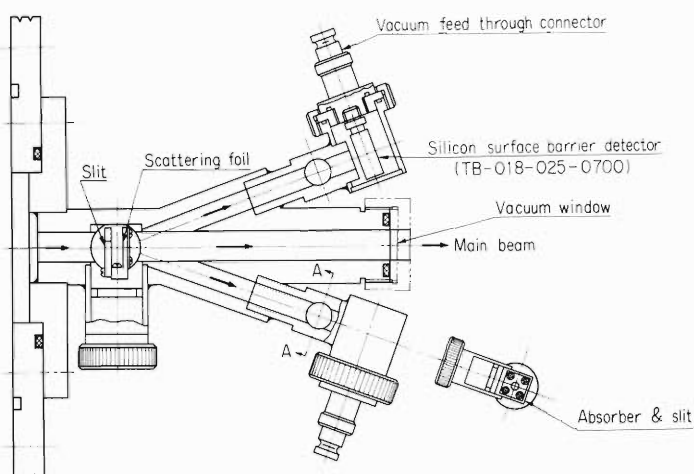
* Faculty of Medicin, University of Tokyo.

Fig. 2(a) Sketch of overall arrangement for dosimetry and exposure of mammalian cells to cyclotron beams.
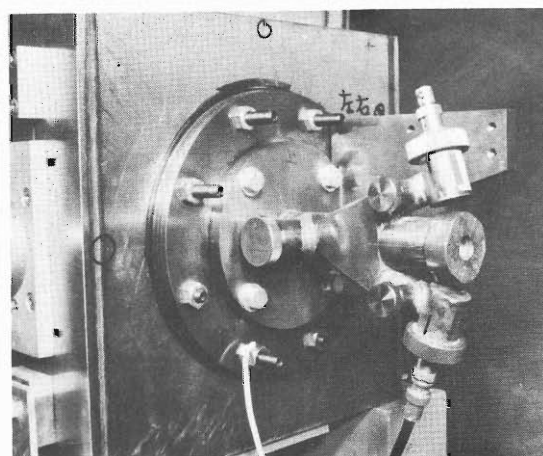
Fig. 2(b) Photograph of overall arrangement for dosimetry and exposure of mammalian cultured cells to cyclotron beams.

decreased. Physical limitation was overcome by extensive adaptation of the cell culture procedures (Fig. 2. (a) and (b)). About 7×10^4 cells were seeded in each petri dish and allowed to grow for approximately 24 h at $37°C$. For determination of colony-forming ability, cells were trypsinized off the vessel as soon as possible after the exposure to cyclotron beams, and the resulting suspensions were diluted appropriately for single plating.

The survival curve of cultured Chenease humster cell V-79 exposed to nitrogen ions was of the exponential type with D_0-value of 190 rad. This survival curve without a shoulder suggests that irradiation with nitrogen ions does not cause sublethal damages in the cells which allow the Elkind-type recovery. The cells irradiated with alpha-particles showed a survival curve having a shoulder and the extrapolation number was 2. The RBE for nitrogen obtained at D_0 was 1.9 and the value for alpha-particle obtained at exponential part of the survival curve was 1.55.

These preliminary results should be confirmed by further investigations. Studies on recovery from the cell damages caused by the cyclotron beams and comparative studies on strand breakage of DNA in the mammalian cells due to heavy ions as well as other types of radiations are also scheduled in our programs.

9-5. LET Effect on the Trapped-Electron Formation in Organic Glasses at 77 K

A. Kira, M. Matsui, and M. Imamura

Ionizing radiation produces mobile electrons in condensed matter. In glassy liquids at low temperature, a part of the electrons disappears by geminate recombination and the remainder is trapped in the media. The yield of the trapped electron is expected to reflect the competition between recombination and trapping; the ratio of these processes is considered dependent on LET. The measurement of the trapped-electron yield under varied LET conditions, therefore, will furnish valuable information on kinetics of the geminate recombination which is one of the basic problems in radiation chemistry.

During this period, we have been preparing to determine the G-values of trapped electrons for alcohols, ethers, and alkanes at 77 K by measuring their optical absorption bands characteristic to the glasses. Since the target area subjected to the optical measurement is to be irradiated homogeneously, our efforts were devoted to design the suitable apparatus for heavy-ion irradiation. A series of performance tests were carried out satisfactorily for 19.9-MeV ^{4}He-ion irradiation of ethanol glass.

10. PREPARATION OF RADIOISOTOPES AND LABELED COMPOUNDS

10-1. Production of Radioisotopes and Preparation of Labeled Compounds for Medical Use

T. Nozaki, S. Ambe, Y. Ito, M. Iwamoto,
T. Karasawa, M. Okano, K. Fukushi, T. Irie,
T. Hara, and K. Taki

Our works in the present period can be summarized as follows: (1) a rapid biosynthesis of selenomethionine-^{73}Se was made possible, (2) some radio-halogen derivatives of cholesterol were synthesized and their behaviors in animal body measured, (3) aluminum arsenide (AlAs) was proved to be a suitable target substance for the production of ^{77}Br and ^{73}Se by the reactions of ^{75}As(α, 2n)^{77}Br and ^{75}As(p, 3n)^{73}Se, respectively, and (4) efforts have been continued for the improvement in the distribution measurement of positron emitters in human body by the use of ^{18}F. The production of ^{18}F, ^{43}K, and ^{123}I has also been continued to supply them to medical users.

The Ge(^{3}He, xn)^{73}Se reaction was used in our preparation of selenomethionine-^{73}Se, though the ^{75}As(p, 3n)^{73}Se is clearly preferable when protons of higher energy are available. The excitation curve for the former reaction was measured as shown in Fig. 1. The bombarded germanium was dissolved in HNO_3-HF containing selenium carrier (0.1 mg), and the selenium was reduced with hydrazine into precipitate of red selenium, which was then converted into $H_2^{73}SeO_3$. A strain very effective to the present synthesis was screened and used. After a con-
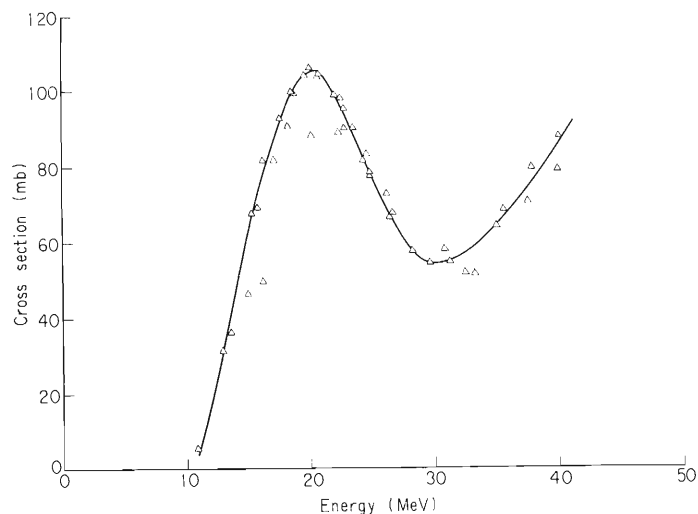

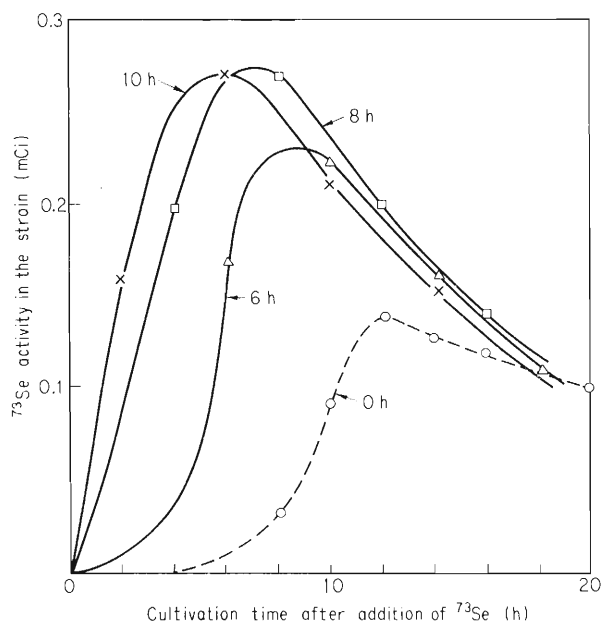Fig. 1. Excitation curve for the reaction of Ge(^{3}He,xn)^{73}Se.

Fig. 2. Uptake of ^{73}Se by the precultivated strain. Figures on the curves are precultivation times. Ordinate value is for the addition of 1.00 mCi of ^{73}Se.
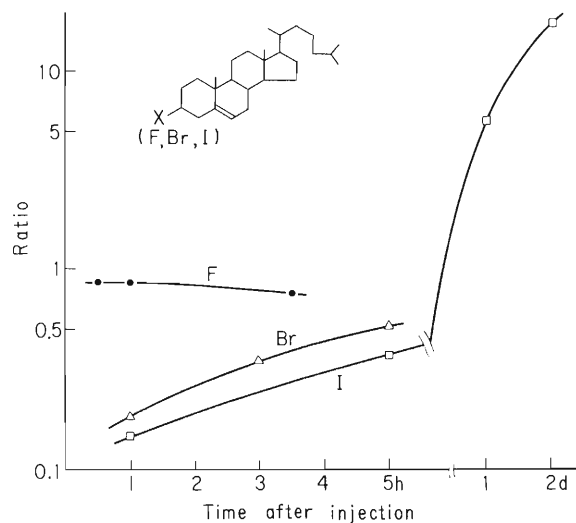

Fig. 3. Adrenal-to-blood concentration ratio for cholesteryl halides.

venient time of precultivation of the strain in a medium for the synthesis of methionine, the H$_2^{73}$SeO^3 was added to the medium and the cultivation continued. The precultivation time and cultivation time were so selected from our experimental results shown in Fig. 2 as to give the optimum incorporated activity of ^{73}Se, nuclide of 7.1 h half-life. The strain containing ^{73}Se was then treated with hydrochloric acid to give its hydrolysis products, from which selenomethionine-^{73}Se was separated by starch column chromatography. It took about four half-lives of ^{73}Se for the entire process, and about 50 μCi of the final product was obtained from 1 mCi of ^{73}Se in the germanium target.

Following radio-halogen derivatives of cholesterol were prepared and their organ distribution intercompared: cholesteryl fluoride, bromide and iodide; 6-fluoro-3-acetoxy-5-hydroxy-cholestan, 5-fluoro and 5-bromo-3-acetoxy-6-hydroxy-cholestan; 19-iodocholesterol, 6-bromomethyl- and 6-iodomethyl-19-nor-cholest-5[10]-en-3β-ol; and excitation-labeled ^{123}I- and ^{77}Br-cholesterol. The labeled cholesteryl halides were prepared by isotopic exchange and halogen interchange reactions. They showed slow clearances from blood, reflecting their hydrophobic character. Time

dependences of their adrenal-to-blood concentration ratios are shown in Fig. 3. The flurohydrins, which were synthesized by the reaction of $B^{18}F_3$ with epoxide, demonstrated high adrenal con-concentrations shortly after intravenous injection. In general, the fluorine-carbon bonds in the steroids showed much higher stabilities than the other halogen-carbon bonds. For adrenal imaging, 6-iodomethyl-19-nor-cholest-5[10]-en-3β-ol was found to be superior to the bromomethyl compound. The ^{123}I excitation labeling gave an organic yield of about 50 %, with its one third being of fairly stable iodosteroid. This iodosteroid, however, showed no particularly interesting in vivo behavior. Similar labeling with ^{77}Br gave poorer and less reproducible organic yield.

Aluminum arsenide, which is stable up to about 2000 K, was found to be a very nice arsenic target. It is commercially available as grey powder soluble in condensed polyphosphoric acid containing H_2O_2. The ^{77}Br in the target was separated carrier-free by this dissolution and subsequent distillation. Carrer-free separation of the ^{73}Se from the target is now under study by the use of solvent extraction of elementary selenium.

11. RADIATION MONITORING

11-1.   Routine Monitoring

K. Igarashi, I. Sakamoto, and I. Usuba

Results of routine radiation monitoring on the cyclotron from April 1975 to March 1976 are described.

No remarkable change in leakage radiation and residual activities was observed during this period.

(1)   Surface and air contamination

The surface contamination has been kept below 10^{-5} $\mu Ci/cm^2$ on the floor of cyclotron room and the underground passage, and below 10^{-7} $\mu Ci/cm^2$ in the experimental areas, hot laboratory and chemical laboratories.   The contamination was wiped off twice a year, and after each decontamination, the higher level contamination could be reduced below 10^{-7} $\mu Ci/cm^2$.

When the accelerating chamber was opened, slight contamination of the air in the cyclotron room was observed.   The value of radioactivity concentration (beta-gamma) was 10^{-12} $\mu Ci/cm^3$.

Tritium still remained in the accelerating chamber since the last triton acceleration in December 1970.   The tritium concentration of the air in the chamber was of the order of 10^{-5} $\mu Ci/cm^3$.   As the air in the chamber is purged completely before overhauling, air contamination was not found in the cyclotron room.

(2)   Drainage

The radioactive concentration of the drain water from the cyclotron building was found to be of the order of $10^{-6} - 10^{-7}$ $\mu Ci/cm^3$.

The total quantity of activities in the aqueous release in this period was about 55 μCi, and the radioactive nuclides found by the gamma-ray spectrometry were mainly ^{58}Co and ^{60}Co.

(3)   Personnel monitoring

The external exposure dose received during the present period, by all cyclotron workers to whom the gamma- and, to some of them also, the neutron film badge are provided, are shown in Table 1.   The collective gamma-ray dose to the workers was 2040 man-mrem, while the thermal and fast neutron exposure were too small to be detected.

Table 1. Annual exposure dose distribution of the cyclotron workers from April 1975 to March 1976.

Workers	Dose distribution (mrem)		
	Undetectable	10–100	>100
Operators	1	4	2
Nuclear Physicists	12	12	1
Physicists of other fields	4	1	1
Radiochemists	0	7	1
Radiation chemists	3		
Biological chemists	3		
Health Physicists	1		

Average annual dose per person: 38.5 mrem

Maximum individual annual dose: 320 mrem

11-2. Neutron and Gamma-Ray Dose Measurement around Targets Bombarded by Deuterons

I. Sakamoto

In the course of an experiment on fast neutron irradiation of biological samples, the neutron and gamma-ray dose distribution has been measured at various distances from a thick beryllium target and a thin deuterium target* bombarded by 15 MeV deuterons at a current of 750 nA.

The fast neutron flux was measured by activation method employing the reaction of ^{32}S (n, p) ^{32}P whose threshold energy is about 2 MeV. The value of flux obtained was converted into the dose equivalent rate using the conversion factor given in ICRP Publication 21. The minimum detectable level of neutron flux in this measurement was about 5×10^5 n cm^{-2}s^{-1}.

A "rem meter"** was also used to measure the dose equivalent rate for fast and slow neutrons at a point 270 cm apart from the target.

The gamma-ray dose was measured with the BeO thermoluminescent dosimeter, the range of measurement of which is 20 mR to 2000 R.

The result of the measurement is shown in Fig. 1. In all cases, the dose rates decrease with the distance a little more slowly than those expected from the inverse square law. The ratios of neutron dose to gamma dose are about 45 for the Be target and about 30 for the D target.
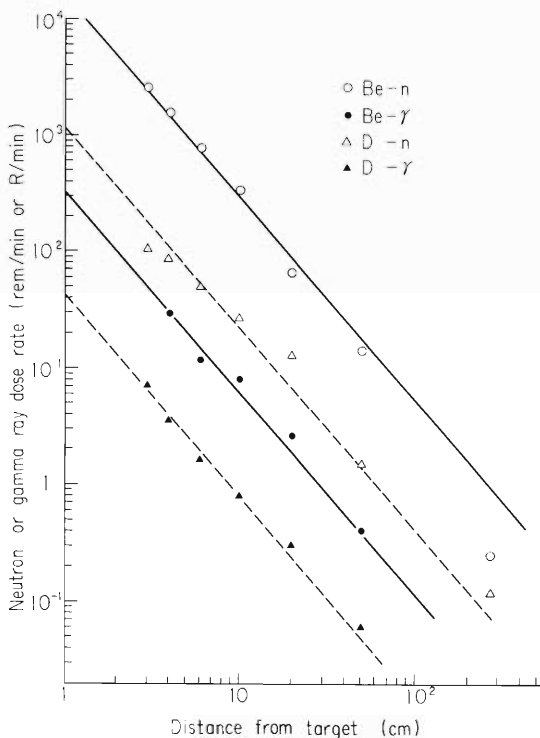
Fig. 1. Neutron and gamma-ray dose rate distribution around targets bombarded by deuterons.

---

*   Code No. DBT 53, produced by The Radiochemical Centre, Amersham, England.
** Neutron Dose Rate Meter 2202, manufactured by AB Atomenergi, Sweden.

12. HEAVY ION LINEAR ACCELERATOR PROJECT

12-1. Status of Constructional Work in 1976

M. Odera

During the Period between the fall 1975 and July 1976, effort was made in cooperation with Sumitomo Heavy Industries Co. to fabricate a proto-type drift tube which contains a compact quadrupole magnet capable to deliver high field gradients without excessive heating of its exciting coil. It proved successful and details of factory production prescription were fixed. Measured maximum field gradients and characteristics of field harmonics of the quadrupole magnets were satisfactory. Distortion of the tube shell by electron beam welding was small, which made possible to align the acceleration axis by use of the optical targets inserted in the center of the shell. The alignment was cross-checked by a hot wire magnetic method and the result was found consistent with each other.

The first tank was completed and its vacuum and radiofrequency characteristics were measured when the tank was still in the factory. Several vacuum leaks were located and stopped within a week. After that, a pressure of 2×10^{-6} Torr was reached in a day. A range of resonant frequency expected in the initial design was obtained and power loss was found to be within the value estimated by models.

The accelerator vault was completed in October and installation of the first tank and the injector high voltage terminal will be completed until the end of November 1976. A proto-type final stage amplifier and its power supply are under construction and will be installed in Spring 1977.

A proto-type hot cathode PIG ion source was constructed. The test stand for the ion source of the cyclotron was modified to accept the new source. Its poles were replaced with those which have cross section designed to give proper focusing force to extracted ions. It is expected that the similar cross section will be used for the linac source unless any trouble was found by the test stand operation. Study of generation and beam formation of the multiply charged heavy ions in the ion source assembly will be made throughout 1977.

12-2. Fabrication of the Drift Tubes of the First Accelerator Tank

Y. Miyazawa and M. Odera

Figure 1 shows cross sections of the drift tubes which contain quadrupole magnets. Shell, end plates, and bore tube are made of OFHC copper and are welded by electron beam. Stem is made of ordinary copper and welded to the shell under the inert gas atmosphere. The outer diameter of the drift tube is 160 mm and the diameter of the magnet yoke is 150 mm leaving 10 mm for the shell. Thickness of the yoke is 15 mm and density of magnetic flux in the yoke is well below saturation for the highest excitation of coil. Figure 2 shows excitation characteristics of the field gradient.
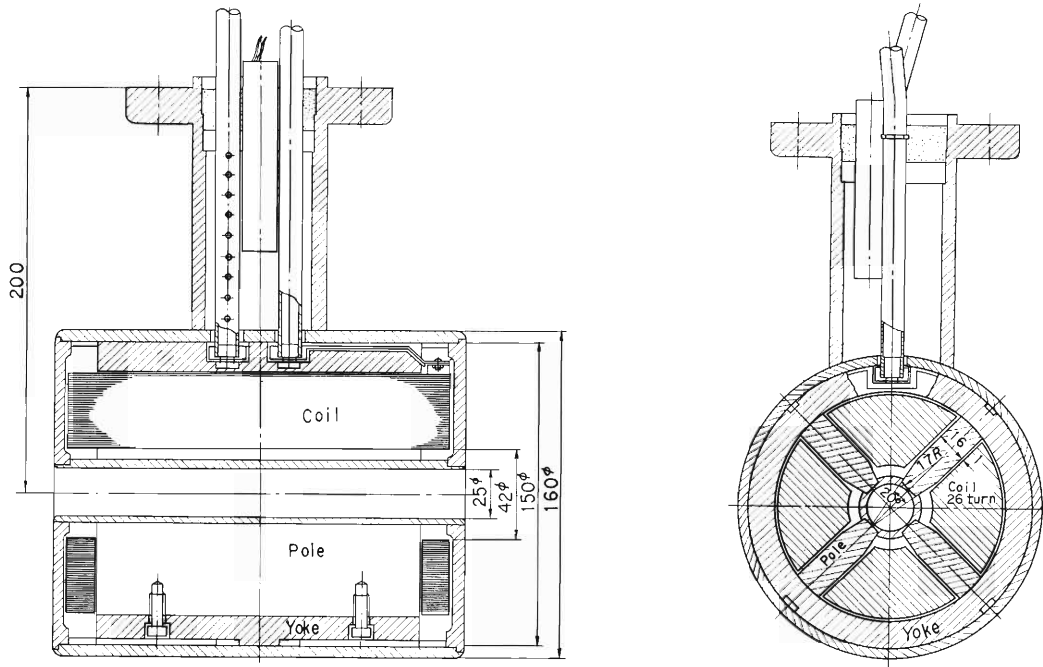
Fig. 1. An example of drift tube structure and its cross sections.
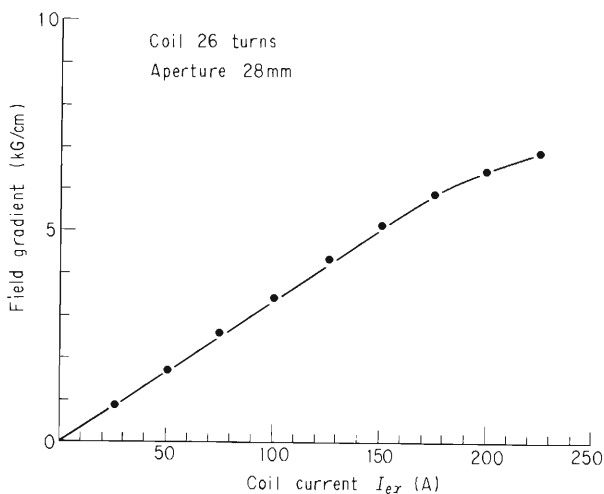
Fig. 2. Excitation characteristics of the field gradient.

Two kinds of coils, the tape coil and the quadrant stacked coil were made. Both types have achieved packing factor above 90 % and enable to realize necessary field gradients for continued excitation. Direct cooling of the coil and the tube shell is made by Freon-113 flowing around the coil and in the grooves cut in the surface of the magnet yoke. The liquid is supplied through copper tubes which also serve as current leads. A thermo-switch is sealed in the stem and detects unusual temperature rise of the coolant and cuts off power supply of the magnet to avoid vaporization of the Freon and sudden pressure rise in the drift tube.

Figure 3 shows drift tubes attached on the center conductor of the accelerator resonator. Since those tubes have no magnets, smaller diameter can be used than that for the tubes containing magnets. They are fabricated by welding copper blocks in inert gas, and shaped by a milling machine. Cooling is made by water.
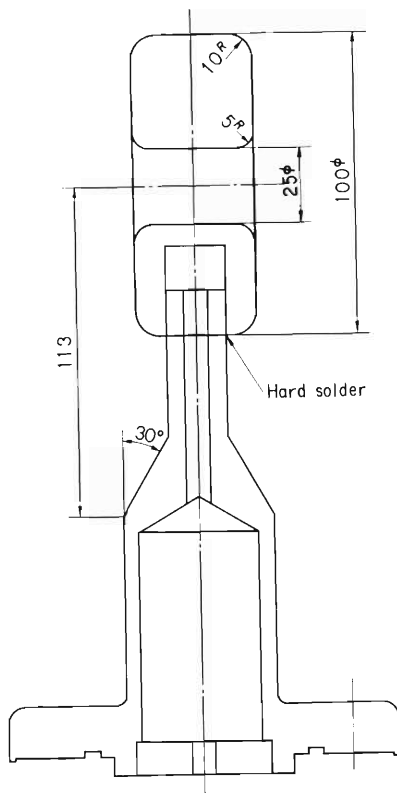
Fig. 3. Drift tube structure attached on the inner conductor of the resonator.

12-3.   Fabrication of Quadrant-stacked Spiral Plate Coil

I. Takeshita and M. Odera

Improvement of the plate coil previously reported[1] was made by use of thin (1 mm) plates instead of thick (3 mm) plates.   Figure 1 shows structure of the coil.   Two holes are drilled and slots are cut in the square plates.   Portion of slots of neighboring plates are butt joined by hard solder to make a square spiral.   This part of the procedure requires most handwork.   Perhaps vacuum or hydrogen furnace hard soldering will be more suitable for large number fabrication. After heat treatment to soften copper, the square spiral is shaped into quadrant by pressing in a cylindrical die.   Then insulation papers impregnated with epoxy resin are inserted and heattreated to make stacked coil layers into a solid monolithic structure.   Bore to accept pole piece is drilled and surfaces are finished by a milling machine.   Short circuiting of layers across insulator caused by the cutting process are removed by chemical etching.   Procedure after insertion of insulation paper is entirely the same with that of the tape-coil.   However, for a fixed number of effective turns, the number of layers for the quadrant stacked coil is the half of that of the tape-coil and so copper sheets twice as thick can be used for a given space.   Since the number of insulators is also half, better packing factor can be achieved if insulator of the same thickness is used.   Figure 2 is a photograph of the coil made in this way.
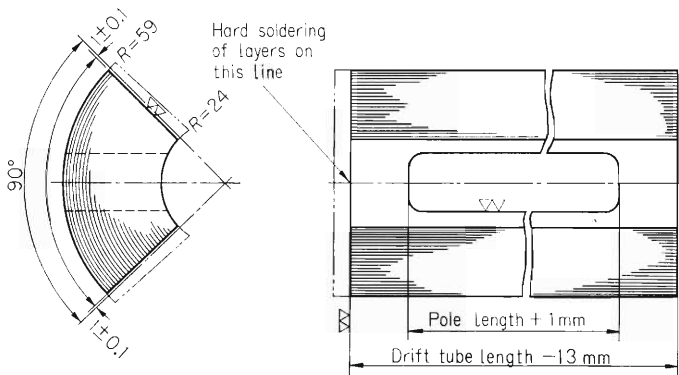

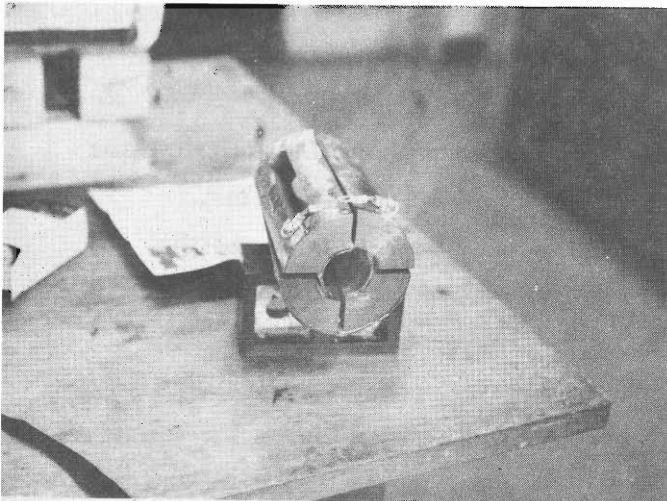Fig. 1.   Structure of a quadrant coil.

Fig. 2.   Photograph of the coil fabricated.

Y. Miyazawa, T. Inoue, M. Hemmi, Y. Chiba,
F. Yoshida, and M. Odera

Figure 1 shows the principle of the function of tape coil.[1] Currents flowing in the two layers of copper tape are made to form a closed single turn around a pole by cutting alternate slots in the tape as shown in the figure. Directions of turns for neighboring poles automatically change alternately and symmetry of turn number for each pole is assured. Thus, coils for a quadrupole magnet can be formed simply by winding copper tape with suitable slots as described above. This ingenious tape coil proposed by Main[1] has also excellent packing factor and is capable of giving a large ampere-turns for limited volume. However, cooling must be made on the surface of the coil and heat generated in the innermost region must be brought to the surface by conduction. Since no current flows at the part where slot is cut, effective packing factor in that region is half the apparent conductor density. Though current density and heat generated per volume of conductor are largest there, the region is directly in contact with colling liquid and so temperature rise will not be excessive. Because permissible working temperature of insulator is limited to a temperature below 120°C, any part of the coil structure must not be heated above this limit. Besides, since boiling temperature of Freon-113 is 47.5°C, surface
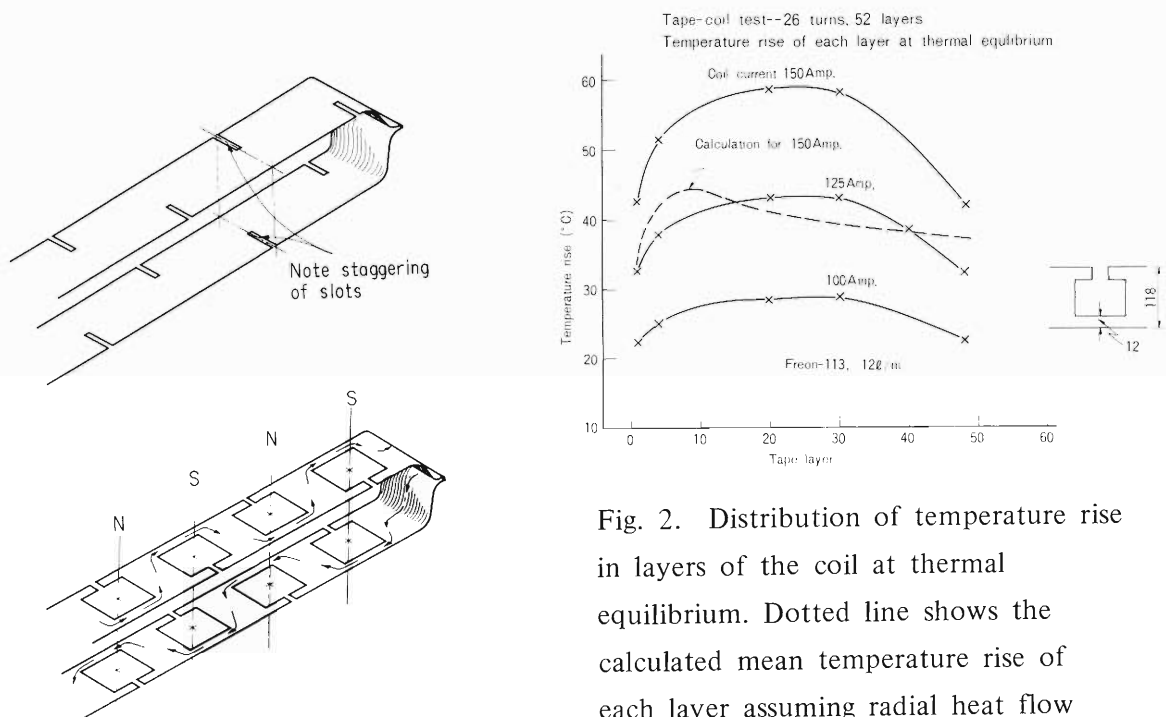

Fig. 1. Illustration of structure
and function of the tape-coil
taken from Ref. 1.

Fig. 2. Distribution of temperature rise
in layers of the coil at thermal
equilibrium. Dotted line shows the
calculated mean temperature rise of
each layer assuming radial heat flow
across insulator layers and uniform
temperature distribution on the surface
of the coil in contact with coolant.

temperature of the coil is not desirable to exceed this value. Therefore, cooling characteristics of the tape-coil were measured to confirm calculated results under the probable condition of use. Coolant enters through 12 mm diameter copper tubing into groove cut on the yoke surface. Then it enters through axial groove into narrow space between coil end and end plate of the drift tube, flows radially inward on the end surface of coil to the center, goes axially through the space between center tube and inner surface of the coil up to the other end, then radially outward on the end surface, and returns via axial and circumferential grooves into another copper tubing. (See Fig. 1 of 12-2 of this progress report for structure of the drift tube.) Temperature rise of each layer of coil was measured by soldering thin wires to the sides of copper sheets and observing variation of resistance of each layer. Figure 2 shows an example of distribution of temperature rise. Since current density in the copper sheets decreases roughly as inverse of radius, heat generated should change as inverse of square of radius. However, inner surface of the coil block is well cooled and heat generated in the inner several layers will be removed through radial inward conduction across thin insulator layers. Therefore, region of maximum temperature shifts outwards. This result of qualitative explanation was compared with that of numerical calculation. A qualitative agreement was obtained, but for better reproduction, the boundary condition of uniform temperature on the surface of coil block in contact with liquid needs to be modified. There seems to exist abrupt change of temperature in the surface film layer between liquid and coil. At some parts of the surface boundary, the film seems to consist of mixed vapor and liquid phase, since, as can be seen in Fig. 2, temperature of coil exceeds boiling temperature of liquid at some layers. Temperature drop across this region cannot be the same as at the region where coolant remains in liquid state. We found it possible to reduce temperature rise of coil by making liquid temperature as low as 3°C. Whether this fact supports or not the above statement of the existence of vapor phase in the surface film at higher liquid temperature is not clear. These cooling tests were performed in a transparent vessel simulating drift tube shell and generation of bubbles was expected to be clearly seen when it is present. However, no distinct change of surface appearance nor bubble formation by change of liquid temperature from 3°C to 20°C could be observed.

Reference

1) R. M. Main and R. Yourd: Proc. Fourth Intern. Conf. on Magnet Tech., p. 349 (1972).
   R. M. Main, J. M. Haughian, and R. B. Meuser: UCRL 17156 (1966).

12-5. Cooling Characteristics of the Quadrant-stacked Spiral Plate Coil

I. Takeshita and M. Odera

Though the tape coil has good cooling characteristics, its margin of safety is sometimes still not sufficient for use with some drift tubes. Main limitations come from the end region where the packing factor is half the expected conductor ratio of 90 %. Also temperature rise in the innermost region is proportional to square of the distance from the end surface of the coil and for a long coil the temperature limit of insulator may easily be exceeded. In the quadrant stacked coil, distance of heat conduction is very small and the packing factor of the conductor always coincides with the apparent value. Figure 1 is result of measurements of the coil in the same configuration and dimension as the tape coil. As expected, temperature rise is very small and roughly one third of that of the tape coil. Nowhere of the surface of the coil the temperature exceeds the boiling point of the coolant. Since the number of layers is the half of the tape coil, the number of insulator is also half and packing factor is better, hence power dissipation is smaller than the tape coil.
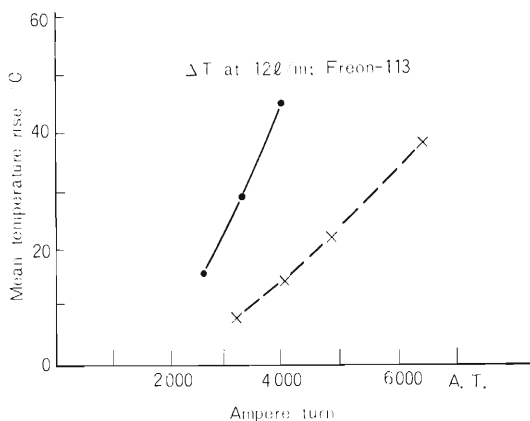
Fig. 1. Mean temperature rise of coils.
X ⋯⋯⋯ X Quadrant stacked coil
● ——— ● Tape coil

Thus, cooling characteristics of the quadrant stacked coil is definitely superior to the tape coil. However, fabrication requires more handwork unless hard soldering process in vacuum or hydrogen furnace is adopted. Therefore it was decided to use this type of coil only in the drift tubes where use of the tape coil is not supposed to be quite safe for continued operation.

12-6. Deviation of the Magnetic Axes of the Quadrupoles from the Geometrical Center of the Drift Tubes

I. Takeshita, I. Yokoyama, and M. Odera

As reported previously the magnetic axes of the quadrupoles to be contained in the drift tubes was found well coincident with the geometrical center of the magnet.[1] However, the magnet has to be sealed vacuum tight in a copper shell by electron beam welding to form a drift tube. Deformation of the tube shell may be expected by thermal stress induced by the welding process. In that case, the field center will not necessarily coincide with the geometrical center of the drift tube shell. Since alignment of the tubes in the manufacturer's factory is to be made by using optical targets set in the geometrical center of the tubes, extent of deviation of the field center from the geometrical one must be known. The device developed to determine center of the quadrupole field by a rotatable Hall probe[1] is also suitable to investigate this problem. (See the reference for its structure.) In its use, geometrical center was first fitted to the device center by use of a dial gauge attached to the rotatable holder of the Hall probe. Next, the dial gauge was replaced by the Hall plate and position of the field center was determined relative to the device center. Another apparatus was used which consists of a brass rod the diameter of which was carefully machined to fit snugly into the center bore of the drift tube and of a Hall prove imbedded in the rod. However, bore of some drift tubes was found not perfectly circular at its entrance and exit ends and did not accept the rod easily. This showed the existence of deformation by welding in spite of small heat generation involved in the electron beam processing. After the determination of the field center those bores were reshaped so as to permit insertion of the optical targets.

Figure 1 shows results of the measurement. Axial positions where tube cross sections are perfectly circular were chosen to avoid interference of welding deformation with determination of geometrical center. A and B correspond to the two end surfaces of a drift tube. As can be seen in the Figure, distinct deviation of the field center exists in some tubes. For the tubes for which deviation larger than 50 μm was observed, correction of the bore was applied with a jig borer machine. Thus, displacement of the field center from the geometrical center is believed to be reduced within 50 μm. The drift tubes were bolted on a long supporting base of the accelerator and aligned by a telescope. Precision of the alignment was checked by another method described in a separate report and the above expectation was confirmed.[2]

Fig. 1. Deviation of the center of the magnetic field. Tube number, for instance, I-5 means fifth drift tube of the first resonator. Coordinates are shown below each figure together with the axial depth of measurements from the entrance of bore. The coordinates are in μm and the depth in mm.

References

1) I. Takeshita and I. Yokoyama: Reports I.P.C.R., (in Japanese), 52, 166 (1976).

2) I. Takeshita, I. Yokoyama, T. Kambara, and M. Odera: IPCR Cyclotron Progr. Rep., 10, 140 (1976).

12-7. Field Harmonics of the Drift Tube Quadrupole Magnets

I. Yokoyama, I. Takeshita, and M. Odera

In order to achieve as small aberration as possible, the field configuration of the quadrupole magnets has to satisfy certain requirements for relative values of its Fourier components as described below. In a cylindrical coordinate system where center axis of the field is chosen as coordinate axis, the field can be derived from the following complex scalar potential developed

Table 1. Fourier expansion coefficients of azimuthal field distributions as functions of axial positions of measurement. L=0 corresponds to the center of the axial length. r_H is the distance from the axis the Hall probe was placed. Only values larger than 0.1% of n=2 component were given. Pole dimensions were those of (a) of the Figures 1 and 2. The quadrant stacked plate coil was used. The magnet was made by the machine shop of the institute.

Table 2. Fourier coefficients for the pole (b) of the Figures 1 and 2. The tape coil was used. The magnet was made by the machine shop of the institute.

$r_H = 12.6$ mm

%mm	L=0	L=20	L=35	L=40	L=45	L=50	L=55	L=60
E_1/E_2	.2	.2	.3	.3	.3	.4	.5	1.0
E_2/E_2	100.	100.	100.	100.	100.	100.	100.	100.
E_3/E_2	.1	.1	.1	.2	.2	.4	.3	.2
E_4/E_2	.1	.1	.1	.1	.2	.3	.2	.1
E_5/E_2	—	—	.1	.1	.1	.2	.1	.1
E_6/E_2	.9	.9	1.0	1.2	2.9	5.6	.6	.1
E_7/E_2	—	—	—	—	—	.3	.1	—
E_8/E_2	—	—	—	—	—	.2	—	—
E_9/E_2	—	—	—	—	—	.1	—	—
E_{10}/E_2	.7	.7	.7	.7	.7	.5	.4	.1

$r_H = 12.6$ mm

%mm	L=0	L=20	L=35	L=40	L=45	L=50	L=55
E_1/E_2	.7	.3	.3	.3	.5	.8	1.1
E_2/E_2	100.	100.	100.	100.	100.	100.	100.
E_3/E_2	.4	.5	.4	.4	.5	.6	.8
E_4/E_2	.3	.2	.2	.3	.5	.4	.5
E_5/E_2	.5	.1	.1	.1	.2	.1	.2
E_6/E_2	5.1	4.5	5.1	7.9	11.2	3.8	1.1
E_7/E_2	.4	.1	.1	—	.1	.1	.2
E_8/E_2	.4	—	—	—	.1	—	.1
E_9/E_2	.4	.1	.1	.1	.5	—	.1
E_{10}/E_2	1.4	1.0	1.1	.8	.1	-.1	.2

$r_H = 9.1$ mm

%mm	L=0	L=20	L=35	L=40	L=45	L=50	L=55	L=60
E_1/E_2	.3	.4	.4	.5	.5	.5	.7	1.2
E_2/E_2	100.	100.	100.	100.	100.	100.	100.	100.
E_3/E_2	.1	.1	.1	.1	.2	.2	.2	.2
E_4/E_2	—	—	—	—	—	.1	.1	—
E_5/E_2	—	—	—	—	—	—	—	—
E_6/E_2	.1	.1	.1	.2	.4	.5	.2	—
E_7/E_2	—	—	—	—	—	—	—	—
E_8/E_2	—	—	—	—	—	—	—	—
E_9/E_2	—	—	—	—	—	—	—	—
E_{10}/E_2	—	—	—	—	—	—	—	—

$r_H = 9.1$ mm

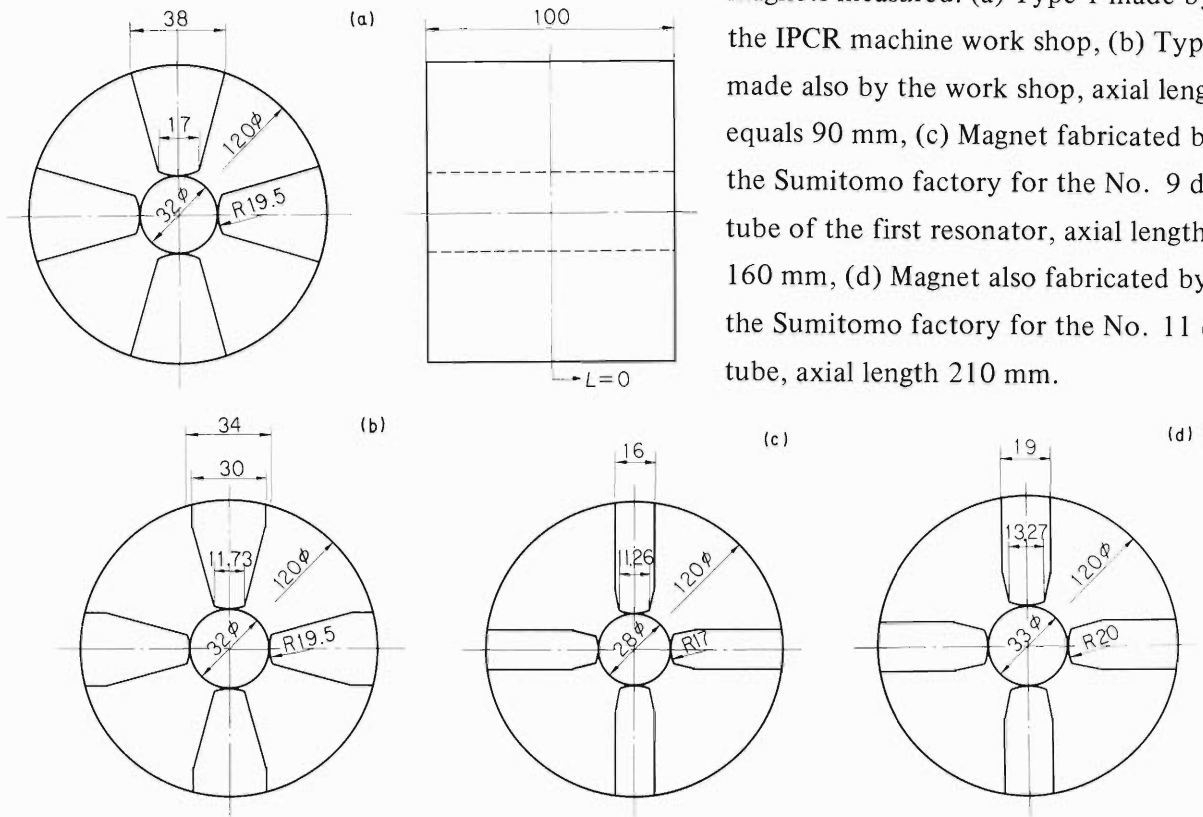| %mm	L=0	L=20	L=35	L=40	L=45	L=50	L=55
E_1/E_2	.4	.1	.4	.4	.6	.8	1.1
E_2/E_2	100.	100.	100.	100.	100.	100.	100.
E_3/E_2	.4	.5	.3	.3	.3	.4	.4
E_4/E_2	.1	.4	.1	.2	.3	.2	.2
E_5/E_2	—	.4	.1	.1	.1	.1	.2
E_6/E_2	1.4	1.5	1.7	2.7	3.3	1.6	.6
E_7/E_2	—	.3	—	—	.1	—	.1
E_8/E_2	—	.3	—	—	.1	—	.1
E_9/E_2	—	.3	—	—	.1	—	.1
E_{10}/E_2	.1	.3	.1	.1	.1	—	.1

Fig. 1. Dimensions of the quadrupole magnets measured. (a) Type 1 made by the IPCR machine work shop, (b) Type 2 made also by the work shop, axial length equals 90 mm, (c) Magnet fabricated by the Sumitomo factory for the No. 9 drift tube of the first resonator, axial length 160 mm, (d) Magnet also fabricated by the Sumitomo factory for the No. 11 drift tube, axial length 210 mm.

in a series

$$F(Z) = \sum_{n=0}^{\infty} c_n z^n , \quad z = re^{i\theta} ,$$

where r and θ are usual cylindrical coordinates; and n = 1 component is called dipole, n = 2 quadrupole, n = 3 sextupole and so on. Ideally, only n = 2 component ought to be present for no aberration. This fact means that the equipotential lines, specifically, pole profiles, are to be exactly hyperbolic. This condition can not be realized in practice, and terms other than n = 2 always exist in the real quadrupole magnets. There are two kinds of such terms in the series expansion shown above. First, the term caused by any kinds of asymmetry of constructing material or by manufacturing defects in some poles. Secondly, kinds of components remain even if symmetry of the field pattern around the coordinate center is secured. Terms specified by n = 2 (2 m + 1) belong to the latter kind. Here, m is positive integer beginning from 0. Therefore, the extent of symmetry achieved for a quadrupole magnet can be judged from the coefficients of terms of the former kind and the effect of non-hyperbolic pole profile can be known from the n = 2 (2 m + 1) terms.

Tables 1–2 show results of measurements on some quadrupoles. In Fig. 1 dimensions of the magnets measured are indicated, and Fig. 2 shows change of each term in the equation as a function of axial position of measurements. Generally, the coefficients are complex or when trigonometric expansion is used, relative phase of each term appears. However, only absolute values normalized by the n = 2 coefficient are given in the tables and the figures for simplicity of presentation. The results show sufficiently small values for the higher harmonics. Symmetry

achieved in fabrication seems satisfactory. The term n = 6 is relatively large, showing the effect of deviation from hyperbolic pole profile. But the value seems not too large to give harmful effect in the beam dynamics. Abrupt change of each term at the exit of magnet comes from break down of the two dimensional presentation of field and possibly from a slight misalignment of pole edge.
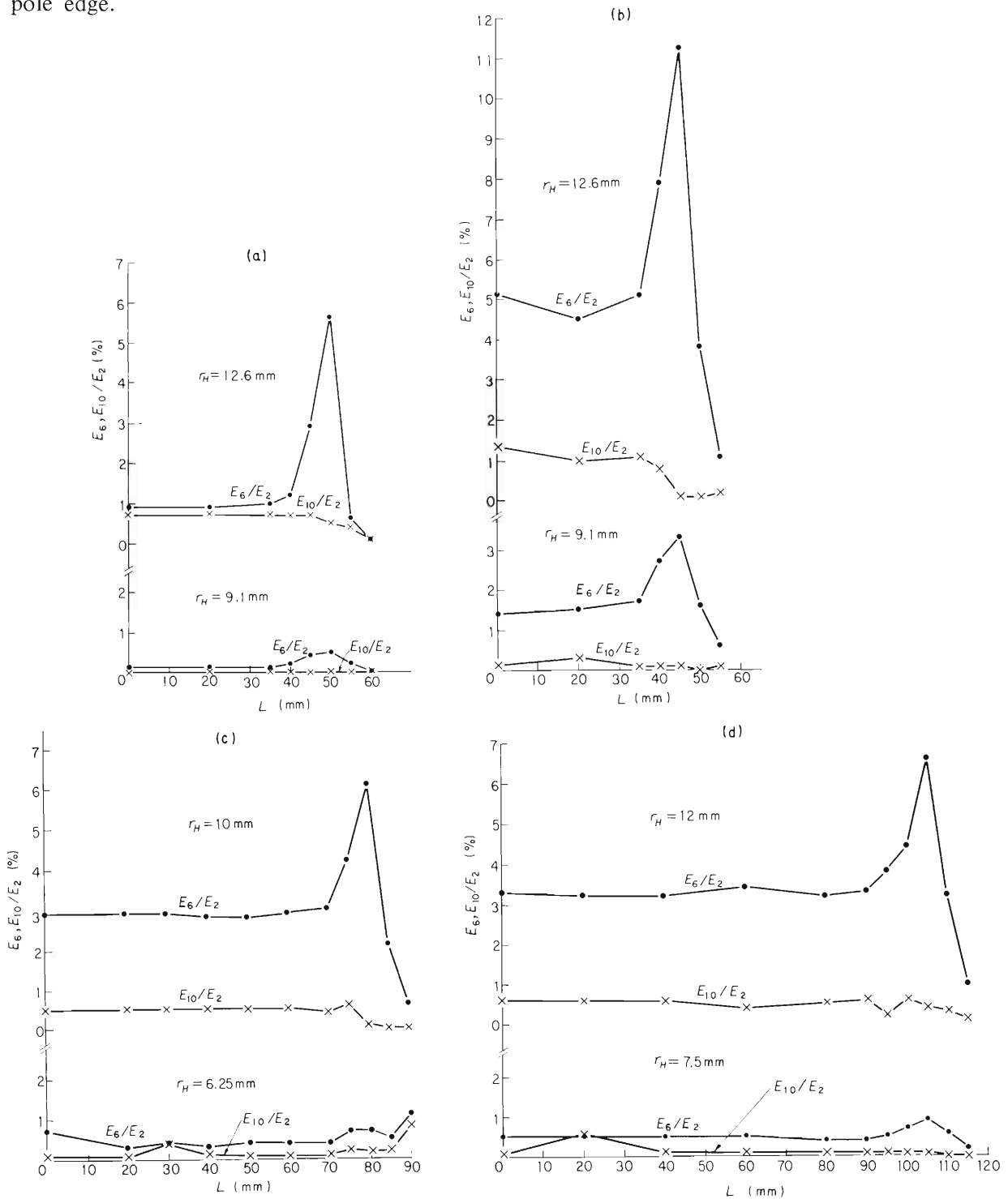
Fig. 2. Change of Fourier amplitudes with axial position. Numbers represent n of the series expansion. (a)-(d) correspond to those of Fig. 1.

12-8. A Digital Data Acquisition and Processing System for Study of Magnetic Field

I. Yokoyama

In the developmental work of a magnet, usually numerous data have to be recorded and analysed. Some methods of automatic recording and processing of the observed data are desirable to make study efficiently. A simple system was constructed and used in conjunction with the work to develope the drift tube magnets. It can be used for more general and complex
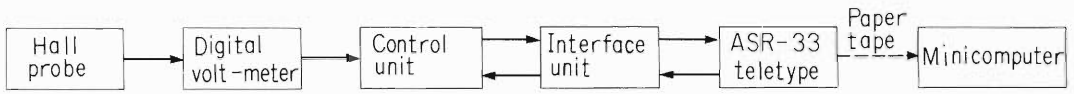
Fig. 1. Diagram of the system.
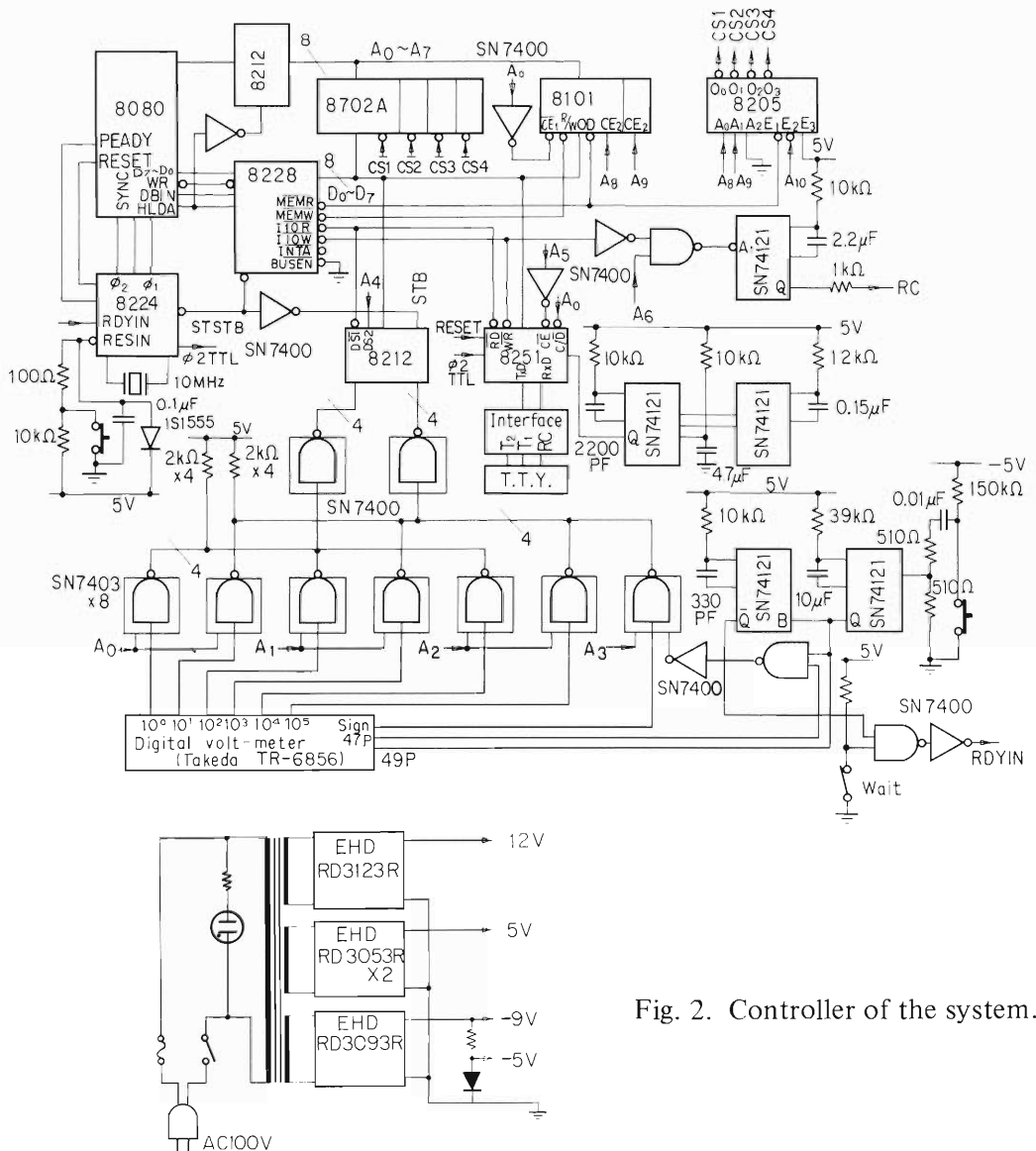
Fig. 2. Controller of the system.
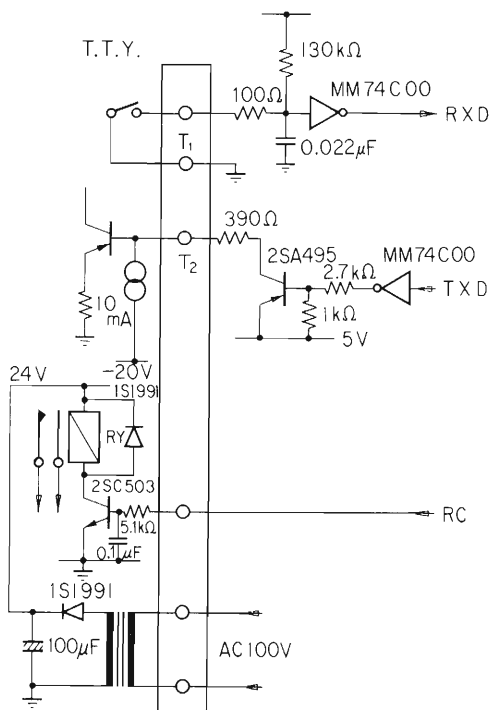
Fig. 3. Interface between teletype and the controller.

magnetic field study. In this system, the strength of the field was digitized by use of a five digit digital volt-meter and a Hall probe. Resolution of the volt-meter was 1 μV. Its BCD output was transferred to a teletype printer and punched out on a paper tape. The tape was processed off-line by a minicomputer Honeywell DDP-124. Figure 1 is a block diagram of the system. Figures 2 and 3 show the control and interface circuits constructed and used.

12-9.   Measurement of Alignment Error of the Drift Tube Array
by the Hot Wire Method

I. Takeshita, I. Yokoyama, T. Kambara, and M. Odera

To secure a good beam transmission in the linac, magnetic field center of each quadrupole magnet set in the drift tube is required to be aligned within 100 μm.[1] In order to examine this alignment, the position of the magnetic field centers were measured with a resolution of 10 μm using a hot wire method.[2]

Figure 1 is a schematic diagram of the hot wire measurement system employed. If z-axis is chosen coincident with the field center axis and x- and y- axes are chosen in the convergent and divergent direction of the field respectively, the force applied to the wire which is strung parallel to the z- axis and displaced by x and y from the field center is

$$F_x = -GILx - k(x - x_0), \qquad F_y = GILy - k(y - y_0),$$

where G is the magnitude of the magnetic flux density gradient, I is the current flowing in the wire, L is the longitudinal length of the magnet, k is the transverse elasticity constant of the wire, and (x_0, y_0) is the displacement of the wire without the field. When the tension of the wire is W, its length is 2ℓ, and the distance between the center of the Q-magnet and the center of the wire is d, k is equal to $2W\ell/(\ell^2 - d^2)$. If k is greater than $|GIL|$, an equilibrium point exists in both x- and y- directions, which is given by

$$x = kx_0/(k + GIL), \qquad y = ky_0/(k - GIL).$$
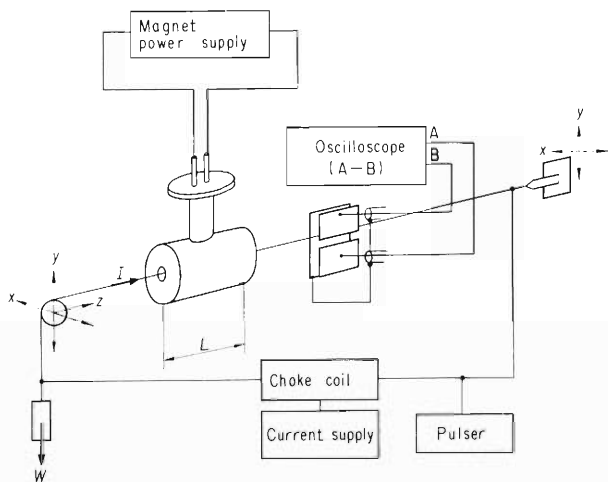
Fig. 1.   Schematic diagram of the measuring system.

In the measurement, a dc current is sent through the wire and one Q-magnet is excited at a time until G approaches to k/IL. The direction of movement of the wire is observed by a condenser sensor with split electrodes and by an oscilloscope, adding a pulse signal to the dc current. The movement along the x- and y- directions are observed independently by altering the direction of the current in the Q-magnet or through the wire, since a better resolution is obtainable in the divergent mode. Each wire holder at both ends has a pair of micrometers which define the x- and y-coordinate of the wire and the holders are moved in parallel until the

movement of the wire is not observed. At that point, the readings of the micrometers are recorded as the x-y coordinate of the magnetic center of the drift tube.

The measurement was done in September 1976 at the Niihama factory of the Sumitomo Heavy Industries Co., Ltd. A tungsten wire with diameter of 0.2 mm and length of 3970 mm was used as the hot wire. The tension applied to the wire was varied as 720, 1000, and 1230 grw. The effect of the vertical sag of the catenary curve was corrected using the parabola approximation. The maximum correction was about 0.6 mm. Figure 2 is a photograph of the drift tubes with sensors.
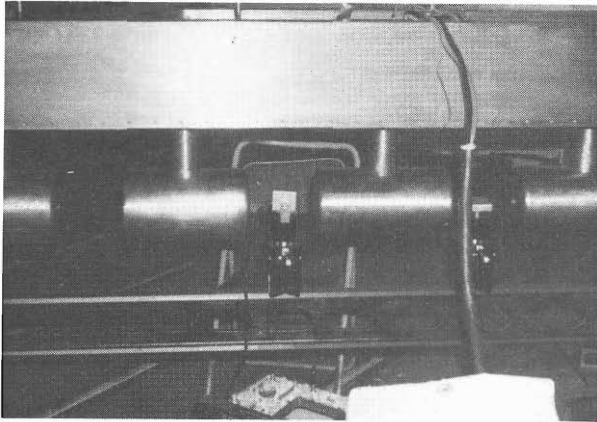
Fig. 2. The drift tubes and the sensors. The left sensor is for the measurement in the vertical direction and the right, for the horizontal direction.

The data obtained were fitted to a straight line with the chi-square minimization method, and the deviations from the line are plotted. The results are shown in Fig. 3 (solid lines), along with those of the geometrical centers measured by the Sumitomo factory inspector using a telescope (dashed lines). Both results have almost the same shape and the difference is less than 40 μm, so it is concluded that the geometrical center of the drift tube and the magnetic field center of the Q-magnet coincide well. In the horizontal direction, the alignment is fairly good and the deviation is less than 60 μm. In the vertical direction, two drift tubes No. 3 and
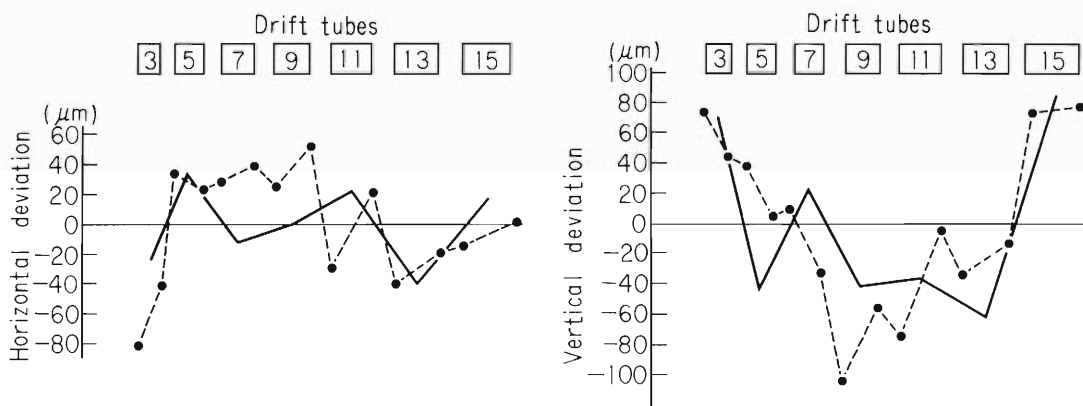
Fig. 3. Deviations of the positions of the drift tube centers from the best fit straight lines. The solid lines are the result of the hot wire method with W=1230grw, and the dashed lines, the geometrical measurement using a telescope. The deviations in the right and upper directions perpendicular to the beam direction are taken as positive in the graphs.

No. 15 give deviations of about 100 μm, values higher than the other tubes. According to another measurements by the factory staff of the flatness of the base of the drift tubes by a dial gauge, some deformation is found to be present in the base, of the same tendency as that observed in the positions of the drift tube centers. So the deviation seems to be mainly due to the unevenness of the base.

We concluded that no correction is needed for the installation of the drift tube, because observed deviation is within the planned value.

References

1) T. Tonuma, F. Yoshida, and M. Odera: Reports I.P.C.R., (in Japanese), 51, 53 (1975).
2) R. M. Main: Proc. Fourth Intern. Conf. on Magnet Tech., p. 735 (1972).

12-10.   Evacuation Test of the First Resonator

Y. Miyazawa and M. Hemmi

Evacuation test of the first tank was made at the Niihama factory of the Sumitomo Heavy Industries Co., Ltd. Molecular and cryogenic pumps were supplied by the laboratory to avoid use of an oil diffusion pump.   The vacuum leaks were located by a helium detector and a residual gas analyser.   The latter was found useful under the large outgassing condition of the newly built vessel of large volume and surface.   The volume of the vessel is $11000\ \ell$ and the surface area is about 9×10^5 cm^2.   After stopping a couple of leakages, a pressure of 10^{-6} Torr was obtained within a day.   This result is satisfactory considering the condition of the surface of the vessel which is not very clean and also the short period of time used for the test. The resonator was disassembled and cleaned before shipment to the laboratory.   It is expected that a pressure of 10^{-7} Torr will be obtained after a long term evacuation in the laboratory.

144

12-11.   Radiofrequency Characteristics of the First Resonator

Y. Chiba

The radiofrequency characteristics of the first resonator were measured at the Niihama factory of the Sumitomo Heavy Industries Co., Ltd.   Figure 1 shows the quality factor and position of shorting plane as functions of the resonant frequency.   Range of frequency expected in the design was obtained.   Quality factor was somewhat better than those measured on the models.   Figure 2 is the voltage distributions along the acceleration axis.   The distribution is more uniform than those measured on the models.
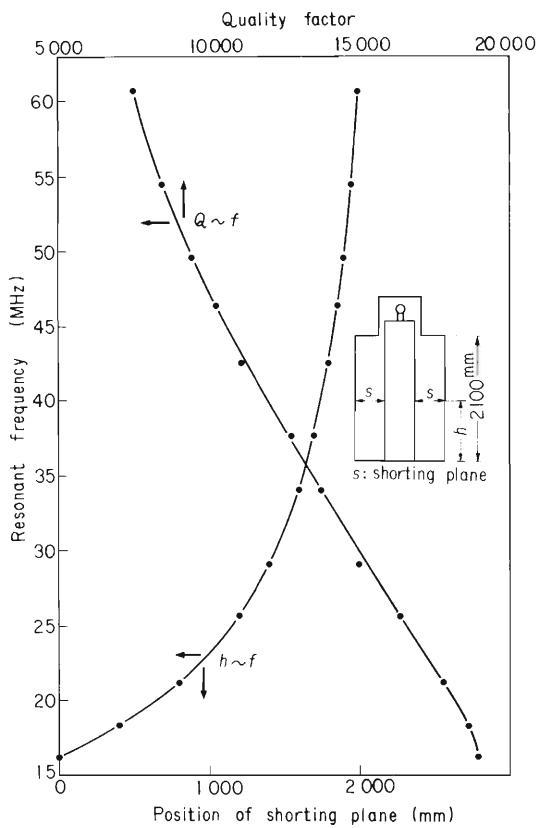
Fig. 1.   Quality factor and position of shorting plane.
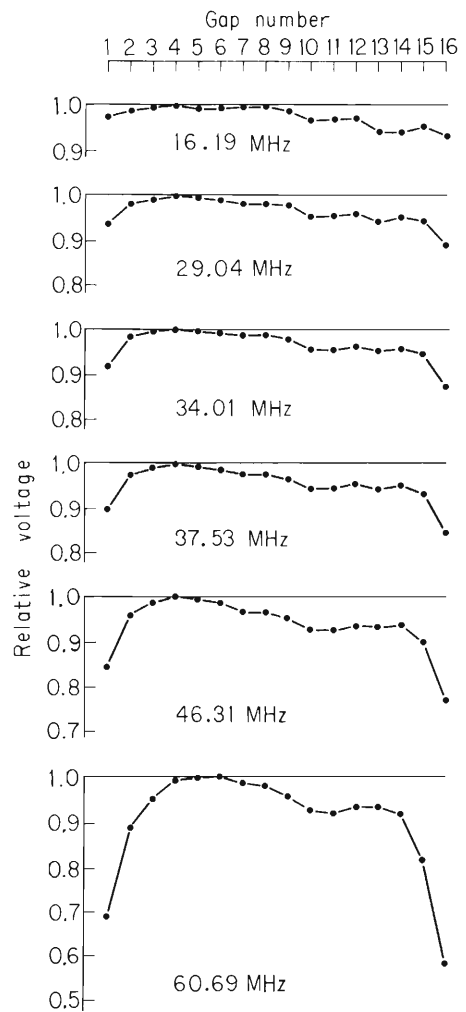
Fig. 2.   Distribution of voltage amplitudes at the accelerating gaps.

12-12. Trial Fabrication of Tape Coil for an Ordinary Quadrupole Magnet

M. Hemmi and F. Yoshida

In view of success in fabrication of tape-coils for the drift tube magnets we tried to use this type of coil also for an ordinary quadrupole magnet having a much larger aperture. Since the method of cooling by Freon-113 applied to the drift tubes, however, is neither convenient nor economical in a large and open air working magnet, other means had to be developed. Heat transfer through electrically insulating but thermally conducting material to a metal panel cooled by water was tried. Figure 1 is a disassembled view of the coil giving name and thickness of material used for thermal contact. The cooling panel is made of a thick aluminium plate with engraved water passage and another aluminium plate welded on it. Figure 2 shows measured mean temperature rise of the coil in comparison with calculation. Explanation of the measured temperature distribution requires radial heat flow across thin epoxy impregnated insulation paper between copper layers as was also the case in the drift tube magnets. Importance of the thickness of the thermal grease layer on the overall temperature rise of the coil should be noted. For efficient cooling, a good surface machining and chemical etching as light as possible to prevent short circuiting between layers are essential. Too much etching makes conductor layer recede deep between insulator valley. In the fabricated coil, degree of etching was as shown in Fig. 3. The cooling characteristics were satisfactory and extensive use of the compact quadrupole magnets with this type of coil seems promissing. Figure 4 is a photograph of the coil.
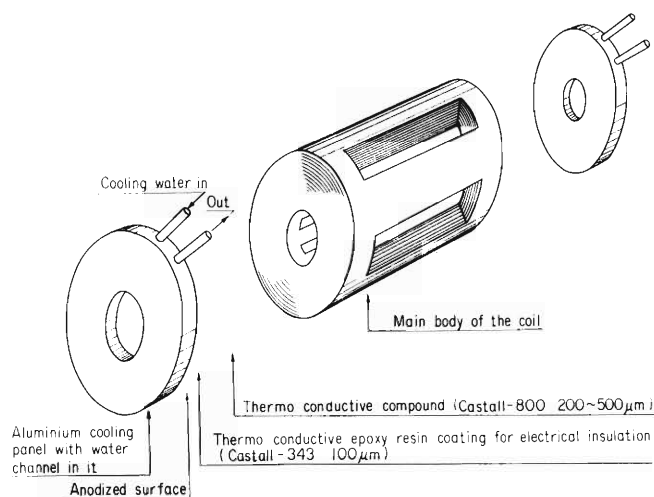
Fig. 1. Method of cooling the coil used for the open air quadrupole magnets.
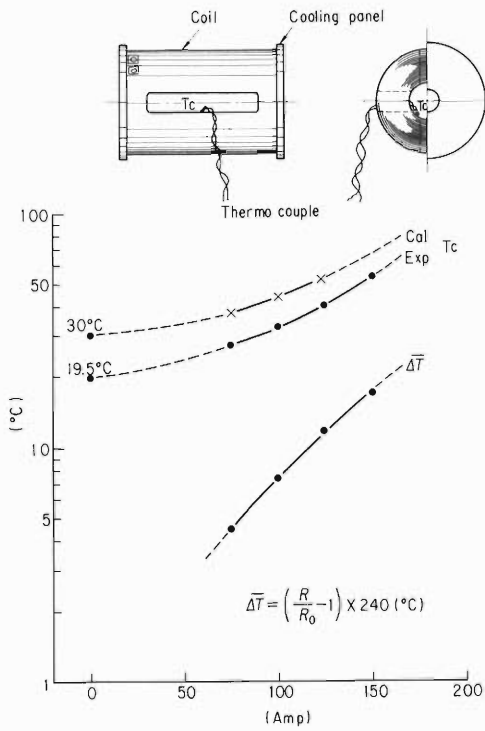
Fig. 2. Mean temperature rise of
the coil v.s. excitation current.

$$\overline{\Delta T} = \left(\frac{R}{R_0} - 1\right) \times 240 \; (°C)$$
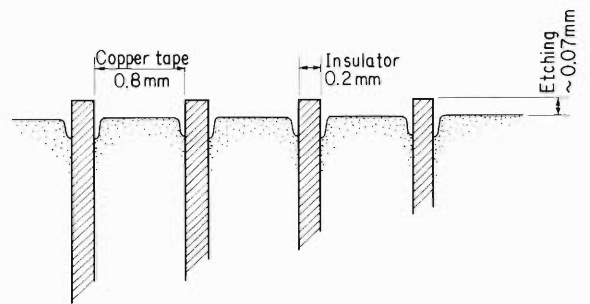
Fig. 3. Etched profile of the coil and
insulator cross section.
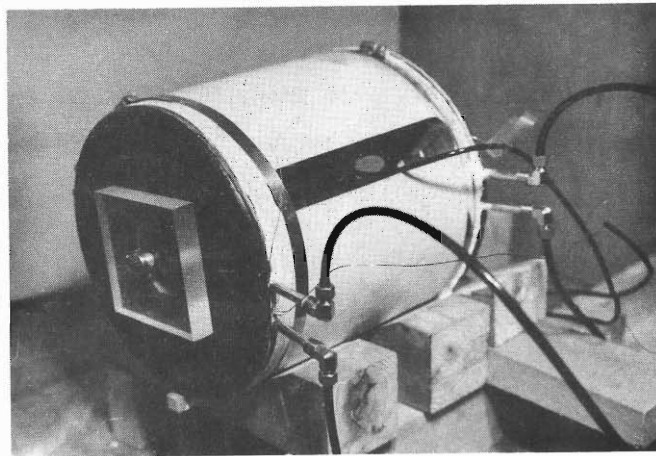
Fig. 4. Photograph of the coil.

12-13.   Design of the Ion Source for the Linac

Y. Ikegami and I. Takeshita

A heavy ion source for the new accelerator Linac was constructed in the Work Shop.   It was designed on the basis of the PIG type ion source used in the cyclotron.   The following improvements were made: (1) Cleaning and replacement of anode, cathodes and insulators are made easier.   (2) The cathode holders are made more sturdy.
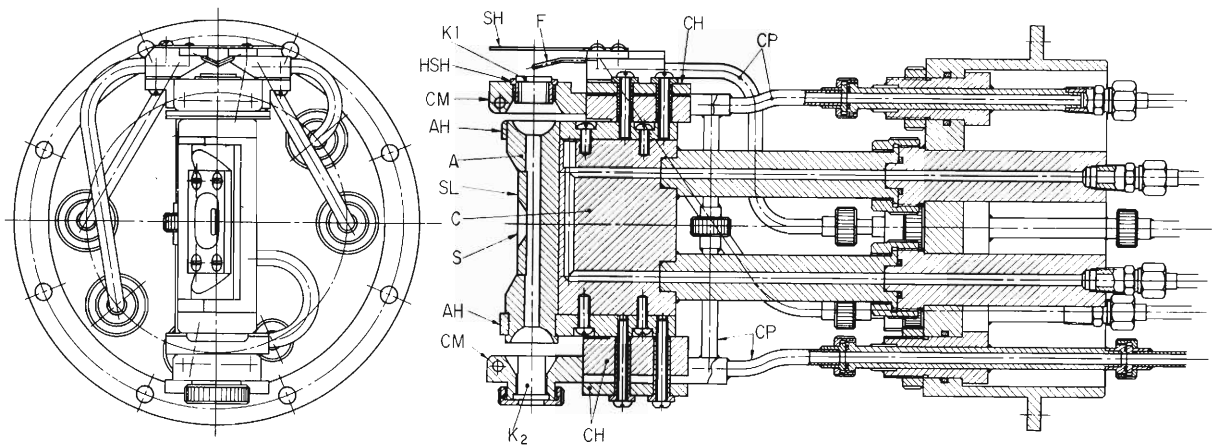
Fig. 1. A heavy ion source for the new accelerator of the linac.

SH: Electron shield (Molybdenum),   SL: Slit (Molybdenum),

F: Filament (Tungsten),   C: Anode block (Copper and water-

CH: Cathode holder (Ceramics),   cooled),

Kl: Hot cathode (Tungsten),   AH: Anode chimney holder (Stainless

HSH: Cathode heat shield (Molybdenum),   steel,

CM: Cathode mount (Copper and   K2:   Reflector cathode (Molybdenum),

         water-cooled),   CP: Cooling pipe (Copper),

A: Anode chimney (Stainless steel), S: Source aperture.

13. LIST OF PUBLICATIONS

1) T. Matsuura and H. Amakawa: "On the Spin-Orbit Terms of ^{3}He- and ^{3}H-Optical Potentials", Genshikaku Kenkyu, $\underline{21,}$ 886 (1976).

2) T. Motobayashi: "Anomalous Angular Distributions in Heavy Ion L=1 Transfer Reactions", Genshikaku Kenkyu, $\underline{21,}$ 687 (1976).

3) T. Fukuda, M. Ishihara, T. Inamura, T. Numao, T. Shimoda, K. Tanaka, and T. Nomura: "Complete Fusion Cross Section Measurement by Beam Attenuation Method", Genshikaku Kenkyu, (in press).

4) Y. Awaya, K. Izumo, T. Hamada, M. Okano, T. Takahashi, A. Hashizume, Y. Tendow, and T. Katou: "K and L X Rays Induced by 5-MeV/amu α-Particle and Nitrogen-ion Bombardment of Ten Target Elements Ranging from Cr to Bi", Phys. Rev., A, $\underline{13,}$ 992 (1976).

5) T. Mikumo, I. Kohno, K. Katori, T. Motobayashi, S. Nakajima, M. Yoshie, and H. Kamitsubo: "Systematics of Optimum Q Values in Multinucleon Transfer Reactions Induced by Heavy Ions", Phys. Rev., $\underline{C14,}$ 1458 (1976).

6) T. Ooi, T. Motobayashi, K. Katori, and I. Kohno: "Detection and Identification of ^{8}Be Nuclei with a Position Sensitive Detector and Counter Telescope", Reports I.P.C.R., (in Japanese), $\underline{52,}$ 145 (1976).

7) I. Takeshita and I. Yokoyama: "A New Method for Precise Determination of Quadrupole-magnetic field of the Drift Tubes of a Heavy Ion Linear Accelerator", Reports I.P.C.R., (in Japanese), $\underline{52,}$ 166 (1976).

8) T. Karasawa and Y. Toda: "An Ultracompact AVF Cyclotron (1), Electromagnet", Reports I.P.C.R., (in Japanese), $\underline{52,}$ 185 (1976).

9) B. Imanishi and K. I. Kubo: "Multi-Step Core-Exchange Analysis of ^{16}O + ^{18}O Scattering with the Full-Recoil Calculation", Phys. Rev. Lett., $\underline{36,}$ 132 (1976).

10) N. Bendjaballah, J. Delaunay, T. Nomura, and H. J. Kim: "Possible Shape Transition in the Yrast Band of ^{56}Fe", Phys. Rev. Lett., $\underline{36,}$ 1536 (1976).

11) H. Tawara, Y. Awaya, Y. Tendow, T. Katou, M. Akiba, and T. Tonuma: "Ar-K-Shell Ionization by High Energy Carbon Ion Impact", Phys. Lett., $\underline{59A,}$ 14 (1976).

12) F. Ambe and S. Ambe: "A ^{119}Sn Mössbauer Emission Study of Recoil ^{119}Sb Atoms after Proton Reactions in SnTe", Chem. Phys. Lett., $\underline{39,}$ 294 (1976).

13) T. Tonuma, F. Yoshida, and M. Odera: IEEE NS-23, No. 2, 1031 (1976).

14) Y. Awaya and K. Izumo: "X-rays Induced by Swift Heavy Ion Bombardment", Oyo Butsuri, $\underline{45,}$ 905 (1976) (in Japanese).

15) T. Inamura, F. Kearns, G. Varley, and J. C. Lisle: "Ground State Rotational Band in ^{181}Ta", Nucl. Phys., $\underline{A270,}$ 255 (1976).

16) N. Bendjaballah, B. Delaunay, J. Delaunay, and T. Nomura: "High Spin States in ^{57}Co",

Nucl. Phys. (in press).

17) N. Bendjaballah, J. Delaunay, A. Jaffrin, T. Nomura, and K. Ogawa: "The Level Structure of ^{56}Fe", Nucl. Phys. (in press).

18) T. Kammuri: "On the Importance of the Sequential Transfer Process in the Two-Nucleon Transfer between Heavy Ions", Nucl. Phys., A259, 343 (1976).

19) M. Uda: "Application of Ion Induced X-ray Spectroscopy to Solid State Chemistry and Its Possibility", Report on Application of Heavy Ions to Atoms and Molecules I.C.P.R., p.53 (1976).

20) F. Ambe and S. Ambe: "Defect ^{119}Sn Atoms after Nuclear Decays and Reaction in SnSb and SnTe", J. Physique (in press).

21) T. Nozaki, Y. Yatsurugi, and Y. Endo: "Charged Particle Activation Analysis — Studies on Carbon, Nitrogen and Oxygen Mainly in Semiconductor Silicon", J. Radioanal. Chem., 32, 43 (1976).

22) A. Koyama, E. Yagi, and H. Sakairi: "Secondary Electron Emission from Ni and Al by High-Energy Proton and α-Particle Bombardment", Japan. J. appl. Phys., 5, 1811 (1976).

23) A. Iwamoto, S. Yamaji, S. Suekane, and K. Harada: "Potential Energy Surfaces for the Fission of the Actinide Nuclei", Prog. Theor. Phys., 55, 115 (1976).

24) H. Shiraishi, H. Sakairi, E. Yagi, T. Karasawa, R. R. Hasiguti, and R. Watanabe: "Growth Process of Helium Bubbles in Aluminum", Trans. Japan Inst. Metals, 17, 749 (1976).

25) S. Yamaji, W. Scheid, H. J. Fink, and W. Greiner: "Dynamical Calculation of the Mass Fragmentation in the Collision ^{238}U - ^{238}U", Z. Physik, A278, 69 (1976).

26) E. Yagi, A. Koyama, H. Sakairi, and R. R. Hasiguti: "Defect Structures of Slightly Reduced Semiconductive Rutile as Observed by Channeling Method", Proc. Intern. Conf. Radiation Effects in Semiconductors, Dubrovnik, (1976), Inst. Phys., London (in press).

27) H. Sakairi, E. Yagi, A. Koyama, T. Karasawa, and R. R. Hasiguti: "Cyclotron Irradiation of Cu$_3$Au Alloys at Low Temperatures", Proc. Intern. Conf. Fundamental Aspects of Radiation Damage in Metals, Gatlinburg, 1975, USERDA, p. 643 (1976).

(Papers presented at meetings)

1) T. Motobayashi: "Experiment of α-Transfer Reactions", Symposium on Scattering of Complex Nuclei and Heavy Ion Reactions, Osaka, Jan. (1976).

2) T. Matsuura, A. Arima, T. Tomoda, and K. Yazaki: "DWBA Analysis of Four-Nucleon Transfer Reaction $^{208}Pb(^{16}O,^{12}C)^{212}Po$", Symposium on Scattering of Complex Nuclei and Heavy Ion Reactions, Osaka, Feb. (1976).

3) T. Suzuki, T. Matsuura, and K. I. Kubo: "Finite-Range Two-Step DWBA Code", Symposium on Scattering of Complex Nuclei and Heavy Ion Reactions, Osaka, Feb. (1976).

4) A. Arima, T. Matsuura, T. Tomoda, and K. Yazaki: "A Method of Generating α-Transfer Form Factors", Symposium on Scattering of Complex Nuclei and Heavy Ion Reactions, Osaka, Feb. (1976).

5) H. Sakairi: "Radiation Damage of Solids by Particle Beams", IPCR Symp. on Study of Atoms, Molecules and Solids with Heavy Ion Accelerator, Wako, Feb. (1976).

6) Y. Awaya: "Multiple Inner-shell Ionization Induced by Heavy Ion Impact", The IPCR Symp. on Ion-Atom Collision, Wako, Feb. (1976).

7) H. Sakairi: "Radiation Damage of Metals by Heavy Charged Particles", Ann. Meeting of Japan Soc. Appl. Phys., Tokyo, March (1976).

8) A. Koyama, E. Yagi, and H. Sakairi: "Secondary Electron Emission from Al by High Energy Proton Bombardment — Calculation", Ann. Meeting of Japan Soc. Appl. Phys., Tokyo, March (1976).

9) E. Yagi, A. Koyama, H. Sakairi, and R. R. Hasiguti: "Lattice Defects of TiO_{2-x}", Ann. Meeting of Phys. Soc. of Japan, Nagoya, Apr. (1976).

10) T. Fukuda, M. Ishihara, T. Inamura, and T. Numao: "Complete Fusion Cross Section Measurements by Beam Attenuation Method(1)", Ann. Meeting of Phys. Soc. of Japan, Nagoya, Apr. (1976).

11) A. Hashizume, Y. Tendow, T. Katou, and H. Kumagai: "In-Beam Spectroscopy on $^{92,94}Mo+C$ Reaction", Ann. Meeting of Phys. Soc. of Japan, Nagoya, Apr. (1976).

12) T. Ooi, T. Motobayashi, K. Katori, and I. Kohno: "Detection of ^8Be Nuclei with a Position Sensitive Detector", Ann. Meeting of Phys. Soc. of Japan, Nagoya, Apr. (1976).

13) H. Kumagai, Y. Awaya, Y. Tendow, M. Akiba, T. Katou, and T. Hamada: "An on-line Bragg Spectrometer", Ann. Meeting of Phys. Soc. of Japan, Nagoya, Apr. (1976).

14) Y. Awaya, M. Akiba, T. Hamada, M. Okano, A. Hashizume, T. Takahashi, Y. Tendow, T. Katou, H. Kumagai, and K. Izumo: "The $K\alpha$ and $K\beta$ Diagram and Satellite Lines and the $K\alpha$ Hypersatellite Lines of Al, Ti, Fe, and Ni Induced by 84-MeV N-ions", Ann. Meeting of Phys. Soc. Japan, Nagoya, Apr. (1976).

15) T. Inamura: "Angular Distributions of γ-rays from Coulomb Excitation of ^{181}Ta", Ann. Meeting of Phys. Soc. of Japan, Nagoya, Apr. (1976).

16) K. Hinode, S. Tanigawa, N. Shiotani, and M. Doyama, "Positron Lifetime Measurements for Aluminium Using An Internal Source" 78th Meeting of Japan Inst. of Metals (JIM), Tokyo, Apr. (1976).

17) T. Nozaki, T. Karasawa, and N. Nonaka: "Manualization of Oxygen Analysis by the $^{16}O(^3He,p)^{18}F$ Activation", 34th Japan Chem. Soc. Meeting, Hiratsuka, Apr. (1976).

18) H. Kamitsubo: "Systematics in the Reactions Induced by C and N Ions in the 100 MeV Region", Proc. of Symp. on Macroscopic Features of Heavy Ion Collisions, Argonne, Apr. (1976).

19) T. Ishihara, T. Numao, T. Fukuda, K. Tanaka, and T. Inamura: "Angular Momentum Transfer of the Quasi-elastic and Deeply Inelastic Processes in the $^{14}N+^{93}Nb$ Reaction at E=120 MeV", Proc. of Symp. on Macroscopic Features of Heavy Ion Collisions, Argonne, Apr. (1976).

20) T. Nomura, J. Delaunay, and N. Bendjaballah: "Unusually Large Difference between Side-Feedings into the 6^+ Doublet in ^{56}Fe", Intern. Conf. on Tandem Phys., Trieste, Apr. (1976).

21) N. Bendjaballah, J. Delaunay, T. Nomura, and H. J. Kim: "Shape Transition in the Yrast Band of ^{56}Fe", Intern. Conf. on Tandem Phys., Trieste, Apr. (1976).

22) M. Aratani and N. Saito: "Charge Spectra of the Si^{n+} Ions Sputtered from Mica under the Helium Bombardment", 13th Ann. Meeting on Radioisotopes in the Physical Sciences and Industry, Tokyo, June-July (1976).

23) M. Aratani and N. Saito: "Ionization of Aluminosilicate by the Presence of Alpha-Emitting Nuclides and Its Simplified Model", 24th Ann. Meeting of the Mass Spectroscopy Society of Japan, Tokyo, July (1976).

24) F. Ambe and S. Ambe: "Mössbauer Emission Studies of Recoil ^{119}Sn Atoms in Sb_2Te_3, SnSb, and SnTe", 16th Mössbauer Spectroscopy Discussion Group Meeting, the Chemical Society, Liverpool, July (1976).

25) Y. Awaya: "X-rays Induced by Heavy Ions", 2nd Hakone Symp. on the Electronic Structure and Collision Process of Heavy Ions, Hakone, July (1976).

26) H. Sekizawa, T. Okada, and N. Shiotani: "Angular Distributions in Cr and Mo", 4th Intern. Conf. on Positron Annihilation, Helsingor, Aug. (1976).

27) N. Shiotani, T. Okada, and H. Sekizawa: "Angular Distribution of Positron Annihilation Radiation in Aluminum", 4th Intern. Conf. on Positron Annihilation, Helsingor, Aug. (1976).

28) T. Mizoguchi, S. von Molnar, G.S.Cargill III, T. Kudo, N. Shiotani, and H. Sekizawa: "Structure and Physical Properties of An Amorphous $Cu_{57}Zr_{43}$ Alloy", 2nd Intern. Symp. on Amorphous Magnetism, Troy, Aug. (1976).

29) K. Fukushi, T. Irie, T. Uchikawa, Y. Kashida, and T. Nozaki: "Preparation of ^{18}F Amino Acids and Purine Bases and Their Distribution in Mice and Rats", 8th Intern. Symp. on Fluorine Chemistry, Kyoto, Aug. (1976).

152

30) T. Fukuda, M. Ishihara, T. Inamura, T. Numao, and T. Nomura: "A New Method of Complete Fusion Cross Section Measurement", European Conf. on Nucl. Phys. with Heavy Ions, Caen, Sept. (1976).

31) R. Ballini, N. Bendjaballah, S. Cavallaro, B. Delaunay, J. Delaunay, T. Nomura, and C. Tosello: "Study of High Spin States for ^{58}Fe and ^{58}Co", European Conf. on Nucl. Phys. with Heavy Ions, Caen, Sept. (1976).

32) T. Nomura, C. Tosello, J. Delaunay, and N. Bendjaballah: "The Distribution of Residual Nuclei from the ^{52}Cr + ^{12}C and ^{48}Ti + ^{16}O Compound Reactions under the Condition of the Same Excitation Energies and Grazing Angular Momenta", European Conf. on Nucl. Phys. with Heavy Ions, Caen, Sept. (1976).

33) T. Nomura: "A Systematics on the Kinetic Energy Dependence of Heavy-Ion Fusion Cross Sections", European Conf. on Nucl. Phys. with Heavy Ions, Caen, Sept. (1976).

34) M. Ishihara: "Coincidence Measurements for p and α with Various Light Products in the ^{14}N + ^{93}Nb Reaction", European Conf. on Nucl. Phys. with Heavy Ions, Caen, Sept. (1976).

35) T. Fukuda, M. Ishihara, T. Inamura, T. Numao, T. Shimoda, and T. Nomura: "Complete Fusion Cross Section Measurements by Beam Attenuation Method", Colloque Franco-Japonais de Spectroscopie Nucleaire et Reaction Nucleaire, Dogashima, Japan, Sept. (1976).

36) H. Kamitsubo: "Particle-Particle and Particle-Gamma Correlation in Heavy Ion Reaction", Colloque Franco-Japonais de Spectroscopie Nucleaire et Reaction Nucleaire, Dogashima, Japan, Sept. (1976).

37) T. Nozaki, K. Fukushi, and T. Irie: "On Some Radiohalogen Derivatives of Cholesterol", 1st Intern. Symp. on Radiopharmaceutical Chem., BNL, Upton, USA, Sept. (1976).

38) K. Ogawa, K. Taki, and T. Nozaki: "Synthesis and Application of ^{73}Se-Selenomethionine", 1st Intern. Symp. on Radiopharmaceutical Chem., BNL, Upton, USA, Sept. (1976).

39) A. Hashizume, T. Katou, and Y. Tendow: "The Excited States in ^{104}Cd following ^{104}Pd(^{3}He, ^{3}N) Reaction", INS Intern. Symp. on Collectivity of Medium and Heavy Nuclei and Colloque Franco-Japonais, Tokyo-Dogashima, Sept. (1976).

40) T. Inamura, K. Hiruta, M. Ishihara, T. Fukuda, and T. Shimoda: "Gamma Ray Spectroscopy with Direct (HI,α) Reactions", INS Intern. Symp. on Collectivity of Medium and Heavy Nuclei and Colloque Franco-Japonais, Tokyo-Dogashima, Sept. (1976).

41) T. Numao, M. Ishihara, T. Inamura, T. Fukuda, and K. Tanaka: "Measurement of Gamma Ray Multiplicities for Deeply Inelastic and Quasi-Elastic Processes", INS Intern. Symp. on Collectivity of Medium and Heavy Nuclei and Colloque Franco-Japonais, Tokyo-Dogashima, Sept. (1976).

42) F. Ambe and S. Ambe: "Defect ^{119}Sn Atoms after Nuclear Decays and Reaction in SnSb and SnTe", Intern. Conf. on the Appl. the Mössbauer Effect, Corfu (Greece), Sept. (1976).

43) E. Yagi, A. Koyama, H. Sakairi, and R. R. Hasiguti: "Defect Structures of Slightly Reduced

Semiconductive Rutile as Observed by Channeling Method", Intern. Conf. on Radiation Effects in Semiconductors, Dubrovnik, Sept. (1976).

44) M. Odera: "RILAC, A Variable Frequency Heavy Ion Linac", 1976 Proton Linear Accelerator Conf., Chalk Kiver Canada, Sept. (1976).

45) Kazuie Kimura, Hideaki Endo, and Masashi Imamura: "Color Center Formation in Alkali Halides by Heavy-Ion Irradiation. III", 19th Conf. Radiation Chem., Kyoto, Oct. (1976).

46) R. Nagai, S. Tanigawa, M. Doyama, and N. Shiotani, "The Influence of Precipitation on Positron Annihilation", The 79th Meeting of Japan Institute of Metals, Sendai, Oct. (1976).

47) H. Sekizawa, K. Asai, T. Okada, N. Shiotani, and S. Ambe: "Perturbed Angular Correlation of Gamma-Rays Emitted from ^{111}Cd in $NiFe_2O_4$", Divisional Meeting of Phys. Soc. of Japan, Yamagata, Oct. (1976).

48) Y. Yamawaki, K. Sakamoto, S. Okada, S. Suzuki, F. Yatagai, I. Kaneko, and A. Matsuyama: "The Effect of High LET Radiation on Cultured Mammalian Cells", 19th Ann. Meeting of Japan Rad. Research Soc., Hiroshima, Oct. (1976).

49) F. Yatagai, S. Kitayama, K. Yoshizaki, K. Kosaka, T. Takahashi, and A. Matsuyama: The Influence of Air Layer before Samples on the Inactivation of Phage $\times$174 by Cyclotron Beam", 19th Ann. Meeting of Japan Rad. Research Soc. Hiroshima, Oct. (1976).

50) T. Shimoda, H. Kamitsubo, M. Ishihara, T. Fukuda, T. Motobayashi, T. Ooi, and I. Kohno: "Measurement of Particle-Particle Correlation in Heavy Ion Reaction", Autumn Divisional Meeting of Phys. Soc. of Japan, Fukui, Oct. (1976).

51) T. Fukuda, M. Ishihara, T. Inamura, and T. Shimoda: "Complete Fusion Cross Section Measurements by Beam Attenuation Method(2)", Autumn Divisional Meeting of Phys. Soc. of Japan, Fukui, Oct. (1976).

52) A. Hashizume, Y. Tendow, T. Katou, and H. Kumagai: "Excited States in ^{104}Cd Revealed by γ-γ Coincidence Experiment Following ^{104}Pd + ^{3}He and ^{96}Mo + ^{12}C Reactions", Autumn Divisional Meeting of Phys. Soc. of Japan, Fukui, Oct. (1976).

53) T. Motobayashi, T. Ooi, S. Nakajima, and I. Kohno: "α-Transfer Reactions between Light Nuclei", Autumn Divisional Meeting of Phys. Soc. of Japan, Fukui, Oct. (1976).

54) S. Motonaga and T. Fujisawa: "Axial Injection into INS Cyclotron", Autumn Divisional Meeting of Phys. Soc. of Japan, Fukui, Oct. (1976).

55) K. Hiruta, T. Inamura, M. Ishihara, T. Fukuda, and T. Shimoda: "Gamma Ray Spectoscopy with Direct (HI, α) Reactions [1]", Autumn Divisional Meeting of Phys. Soc. of Japan, Fukui, Oct. (1976).

14. LIST OF PERSONNEL

Members of the Board

DOTE Toshihiko　土手敏彦 (Chairman)　　HAMADA Tatsuji　浜田達二
KAMITSUBO Hiromichi　上坪宏道　　NAKANE Ryohei　中根良平
NOZAKI Tadashi　野崎正　　ODERA Masatoshi　小寺正俊
KOHNO Isao　河野功

Users Committee

HAMADA Tatsuji　浜田達二 (Chairman)　　IMAMURA Masashi　今村昌
KAMITSUBO Hiromichi　上坪宏道　　KOHNO Isao　河野功
MATSUYAMA Akira　松山晃　　NOZAKI Tadashi　野崎正
ODERA Masatoshi　小寺正俊　　SAKAIRI Hideo　坂入英雄
SEKIZAWA Hisashi　関沢尚

Operation and Machine Maintenance Group

FUJITA Shin　藤田新　　IKEGAMI Kumio　池上九三男
KAGEYAMA Tadashi　影山正　　KOHARA Shigeo　小原重夫
KOHNO Isao　河野功　　NAKAJIMA Hisao　中嶋尚雄
OGIWARA Kiyoshi　荻原清　　TAKEBE Hideki　武部英樹
TAKESHITA Isao　竹下勇夫　　YOKOYAMA Ichiro　横山一郎

Scientific and Engineering Personnel
Cyclotron Laboratory

FUJISAWA Takashi　藤沢高志　　FUJITA Jiro　藤田二郎
INAMURA Takashi　稲村卓　　ISHIHARA Masayasu　石原正泰
KAMITSUBO Hiromichi　上坪宏道　　KARASAWA Takashi　唐沢孝
KOHNO Isao　河野功　　MATSUURA Toshihiko　松浦俊彦
MOTONAGA Shoshichi　元永昭七　　NAKAJIMA Shunji　中島諄二
NAKANISHI Noriyoshi　中西紀喜　　NOMURA Toru　野村亨*
SUZUKI Toshio　鈴木敏男　　WADA Takeshi　和田雄
YAMAJI Shuhei　山路修平

(Visitors)

HIRUTA Kotaro　蛭田幸太郎　(Tokyo Gakugei Univ.)
ICHIMURA Munetake　市村宗武　(Univ. of Tokyo)
IMANISHI Bunryu　今西文竜　(Univ. of Tokyo)
KAMMURI Tetsuo　冠哲夫　(Osaka Univ.)
KATORI Kenji　鹿取謙二　(Tsukuba Univ.)
KAWAI Mitsuji　河合光路　(Kyushu Univ.)
KOIKE Masahiro　小池正宏　(Univ. of Tokyo)
MIKUMO Takashi　三雲昻　(Tsukuba Univ.)
NOJIRI Yoichi　野尻洋一　(Osaka Univ.)
OHNUMA Hajime　大沼甫　(Univ. of Tokyo)
SHIMOKOSHI Fumio　霜越文夫　(Univ. of Tokyo)

* On leave of absence to : DPHNBE, CEN Saclay, B.P. 2, 91190 Gif/Yvette, France.

SHINNO Hitoshi　　新野　仁　　(Nat'l Res. Inst. for Metals)
SHIRAISHI Haruki　　白石春樹　　(Nat'l Res. Inst. for Metals)
TAKAHASHI Noriaki　高橋憲明　　(Osaka Univ.)
TAKEMASA Tadashi　武政尹士　　(Saga Univ.)
YOSHIDA Hiroshi　　吉田　弘　　(Tokyo Inst. Tech.)

(Students)

FUKUDA Tomokazu　福田共和　　(Univ. of Tokyo)
MOTOBAYASHI Tohru 本林　透　　(Univ. of Tokyo)
OOI Takao　　大井孝雄　　(Tsukuba Univ.)
SHIMODA Tadashi　　下田　正　　(Kyoto Univ.)
TANAKA Koichiro　　田中耕一郎　　(Univ. of Tokyo)
TOBA Yoshiyuki　　外羽吉幸　　(Kyoto Univ.)

Linac Laboratory

CHIBA Yoshiaki　　千葉好明　　　HEMMI Masatake　　逸見政武
INOUE Toshihiko　　井上敏彦　　　KAMBARA Tadashi　　神原　正
MIYAZAWA Yoshitoshi　宮沢佳敏　　ODERA Masatoshi　　小寺正俊
SHIMAMURA Akira　島村　旻　　　TONUMA Tadao　　戸沼正雄
YOSHIDA Fusako　　吉田房子

Radiation Laboratory

AWAYA Yohko　　粟谷容子　　　HAMADA Tatsuji　　浜田達二
HASHIZUME Akira　　橋爪　朗　　　IZUMO Koichi　　出雲光一
KATOU Takeo　　加藤武雄　　　KONNO Satoshi　　金野　智
KUMAGAI Hidekazu　熊谷秀和　　OKANO Masaharu　　岡野真治
TAKAHASHI Tan　　高橋　旦　　　TENDOW Yoshihiko　天道芳彦

(Visitors)

AKIBA Mitsunori　　秋葉光徳　　(Tokyo Inst. Tech.)
DOKE Tadayoshi　　道家忠義　　(Waseda Univ.)
FUJIOKA Manabu　　藤岡　学　　(Tohoku Univ.)
HAYASHIBE Shogo　林部昭吾　　(Tohoku Univ.)
IIO Masahiro　飯尾正宏　　(Tokyo Metropol. Jeriatric Hosp.)
NAGAHARA Teruaki　永原照明　　(Rikkyo Univ.)
SUZUKI Kazuaki　　鈴木一明　　(Japan Anal. Chem. Res. Inst.)
TAWARA Hiroyuki　　俵　博之　　(Kyushu Univ.)

Nuclear Analytical Chemistry Laboratory

AMBE Fumitoshi　　安部文敏　　　AMBE Shizuko　　安部静子
ARATANI Michi　　荒谷美智　　　ITO Yoshiko　　伊東芳子
IWAMOTO Masako　　岩本正子　　　NOZAKI Tadashi　　野崎　正
SAITO Nobufusa　　斎藤信房

(Visitors)

FUKUSHI Kiyoshi　　福土　清　(Nat. Inst. of Radiological Sciences)
HARA Toshihiko　　原　敏彦　　(Nat. Nakano Chest Hosp.)
IRIE Toshiaki　　入江俊章　　(Nat. Inst. of Radiological Sciences)

KASIDA Yoshihiko　樫田義彦　(Nat. Inst. of Radiological Sciences)
TAKI Ko　　　滝　幸　　(Kitazato Univ.)

Radiobiology Laboratory

KANEKO Ichiro　金子一郎　　　　　KITAYAMA Shigeru　北山　滋
MATSUYAMA Akira　松山　晃　　　　YATAGAI Fumio　谷田貝文夫

(Visitors)

OKADA Shigefumi　岡田重文　(Univ. of Tokyo)
SAKAMOTO Kiyohiko　坂本澄彦　(Univ. of Tokyo)

Radiation Chemistry Laboratory

IMAMURA Masashi　今村　昌　　　　　KIMURA Kazuie　木村一宇
KIRA Akira　吉良　爽　　　　　　　MATSUI Masao　松井正夫

(Student)

HARATA Yasuo　原田康雄

Metal Physics Laboratory

KOYAMA Akio　小山昭雄　　　　　　SAKAIRI Hideo　坂入英雄
SHIOTANI Nobuhiro　塩谷亘弘　　　　YAGI Eiichi　八木栄一

(Visitor)

TANIGAWA Shoichiro 谷川庄一郎　(Univ. of Tokyo)

Magnetic Materials Laboratory

ASAI Kichizo　浅井吉蔵　　　　　　OKADA Takuya　岡田卓也
SEKIZAWA Hisashi　関沢　尚

(Visitor)

MIZOGUCHI Tadashi　溝口　正　(Gakushuin Univ.)

15. LIST OF OUTSIDE USERS AND THEIR THEMES

(Jan. — Dec. 1976)

1) H. Nakahara and M. Yanokura,   Faculty of Science, Tokyo Metropolitan Univ.
"Isomeric Cross Section for the ^{121}Sb$(\alpha,\alpha n)$
^{120m}Sb and ^{121}Sb$(^3$He,^{3}He n$)^{120m}$Sb
Reactions"

2) Y. Murakami, Y. Honma, E. Shirai, and   Faculty of Science, Tokyo Metropolitan Univ.
M. Unno
"Production of ^{61}Cu and ^{68}Ge"

3) T. Furuta, T. Katou, and S. Kawasaki,   Japan Atomic Energy Research Inst.
"Study of Effect of Helium Bubbles on the
Mechanical Behavior of Stainless Steel"

4) M. Nakamura,   Faculty of Medicine, Kyushu Univ.
"Production of ^{43}Kr"

5) K. Shiraishi and A. Hishinuma,   Japan Atomic Energy Research Inst.
"Radiation Damage of Stainless Steel by
Alpha Irradiation"

6) A. Iida,   Faculty of Engineering, Tokyo Univ.
"X-ray Diffraction Study of the Effect of
Alpha-Bombardment of Si-Crystal"

7) A. Furusawa and S. Tamaki,   Faculty of Science, Niigata Univ.
"Production of ^{124}Sb for Perturbed
Angular Correlation Measurement"

8) Y. Murakami and M. Yanokura,   Faculty of Science, Tokyo Metropolitan Univ.
"Production of ^{57}Co, ^{62,63}Zn, ^{68}Ga,
^{67}Ge, and ^{123}I"

9) A. Hishinuma, K. Fukai, T. Aruga,   Japan Atomic Energy Research Inst.
T. Katou, T. Furuta, and T. Otomo,
"Simulation Test on Neutron Irradiation
Damage of Stainless Steel for Fast Breeder
Reactors by Alpha-Bombardment"

10) M. Shimada, K. Une, and M. Terasawa,   Toshiba R. & D. Center
"Cyclotron Irradiation for Study of
FBR Material Embrittlment"

11) A. Furusawa and K. Mori,   Faculty of Science, Niigata Univ.
"Production of ^{152,154}Eu for Perturbed
Angular Correlation Measurement"

158

12) A. Hishinuma, K. Shirai, and K. Fukai,   Japan Atomic Energy Research Inst.
    "Helium Effect on the Formation of Void
    in SUS316 by Electron Bombardment"

13) Y. Murakami and H. Nakahara,   Faculty of Science, Tokyo Metropolitan Univ.
    "Study of Nuclear Reaction Products for
    the Purpose of Medical Use"

AUTHOR INDEX

理化学研究所

埼玉県　和光市　広沢

理化学研究所

埼玉県　和光市　広沢